UNIVERSITÀ
DEGLI STUDI
FIRENZE

PhD SCHOOL
INGEGNERIA INDUSTRIALE

CURRICULUM:
Energetica e Tecnologie Industriali ed Ambientali Innovative

XXIX PhD SCHOOL CYCLE

PhD SCHOOL COORDINATOR: Prof. De Lucia Maurizio

EXPERIMENTAL INVESTIGATION ON THE FLUID-DYNAMIC LOSSES IN POWER GEARBOXES FOR AEROENGINE APPLICATIONS

Scientific Area: ING-IND/09

PhD Candidate
Dott. Massini Daniele

Academic Supervisor
Prof. Facchini Bruno

PhD School Coordinator
Prof. De Lucia Maurizio

2014/2016

George Gray

I HAVE studied many times
The marble which was chiseled for me
A boat with a furled sail at rest in a harbor.
In truth it pictures not my destination
But my life.
For love was offered me and I shrank from its disillusionment;
Sorrow knocked at my door, but I was afraid;
Ambition called to me, but I dreaded the chances.
Yet all the while I hungered for meaning in my life.
And now I know that we must lift the sail
And catch the winds of destiny
Wherever they drive the boat.
To put meaning in one's life may end in madness,
But life without meaning is the torture
Of restlessness and vague desire
It is a boat longing for the sea and yet afraid.

Edgar Lee Masters (1868–1950), Spoon River Anthology

Acknowledgements

Alla fine di questo percorso desidero fare un sincero ringraziamento a tutti i miei compagni di viaggio.
Un primo ringraziamento spetta ovviamente al prof. Facchini il quale mi ha dato fiducia nel farmi intraprendere questa strada che si è rivelata piena di occasioni di crescita professionale e non.
Il lavoro che ho portato avanti non sarebbe stato possibile senza l'interesse di GE Avio s.r.l. in particolare nella figura dell'ingegnere Federico Leonardi al quale vanno i miei ringraziamenti.
Ho ricevuto un grande sostegno durante il dottorato anche dai ragazzi di Ergon Research, soprattutto da parte di Lorenzo che mi ha accompagnato in quasi ogni attività sperimentale svolta in questi anni, ma non posso non ricordare con piacere la mia primissima attività di ricerca con Mirko, la mia prima conferenza con Cosimo in prima fila a vedermi balbettare in inglese e qualche serata a Seoul con Riccardo.
Un grazie anche alle figure più autorevoli del gruppo, l'ing. Antonio Andreini e il prof. Carlo Carcasci, con i quali le occasioni di confronto non sono state continue ma sempre proficue.
Ma veniamo a noi, sono entrato in questo gruppo di ricerca da perfetto sconosciuto, iniziare un'attività di laboratorio senza neanche conoscere dove fosse un cacciavite significa dover chiedere aiuto per qualsiasi inezia. Desidero quindi ringraziare il Maio, il Picchi e Marchino, che sono stati i primi abitanti del Lab Colonne che ho incontrato e che mi hanno aiutato a muovere i primi passi.
Con il passare degli anni il gruppo si è ampliato e ho avuto modo di

lavorare con tanti altri Lab Guys divisi fra il Colonne e il THT e con i quali ho condiviso gioie e dolori: Giulio, Riccardo, Tommaso B., Lorenzo C. e Valter.
Anche se è difficile ammetterlo, nel gruppo dei numerici ho trovato dei compagni di strada fondamentali Lorenzo W., Lorenzo M., Davide B., Stefano P., Daniele P, Dominique, in particolare Tommaso F. (che ho quasi convertito agli esperimenti, salvo accorgersi che si sta meglio alla scrivania) e Leopoldo (a Kyoto ancora raccontano di un gigante che si aggirava per strada all'alba la scorsa estate).
Questo gruppo è stato anche occasione di divertimento, non sono mancate aperitivi, cene e dopocene che non avrebbero avuto lo stesso sapore senza animatori del calibro di Luca (ormai ex da qualche anno ma sempre presente), dell'Inno e della Sabri e per non parlare del mio storico compagno di merende Ema (futuro premier). Sono riuscito ad arrivare in fondo nonostante (o forse anche grazie a) tutto ciò che sta fuori da questo mondo e che ogni tanto mi riporta alla vita sociale, il mio gruppo scout e i miei amici storici che con questi argomenti proprio non legano.
Un supporto fondamentale è stato invece la mia famiglia che nei momenti un po' più difficili e tempestosi è sempre un porto in cui tornare.

Abstract

Enhancing the efficiency of gearing systems is an important topic for the development of future aero-engines with low specific fuel consumption. The transmission system has indeed a direct impact on the engine overall efficiency by means of its weight contribution, internal power losses and lubrication requirements. Thus, an evaluation of its structure and performance is mandatory in order to optimize the design as well as maximize its efficiency. Gears are among the most efficient power transmission systems, whose efficiencies can exceed 99 %, nevertheless in high speed applications power losses are anything but negligible. All power dissipated through losses is converted into heat that must be dissipated by the lubrication system. More heat leads a larger cooling capacity, which results in more oil, larger heat exchangers which finally means more weight.
Mechanical power losses are usually distinguished in two main categories: load-dependent and load-independent losses. The former are all those associated with the transmission of torque, while the latter are tied to the fluid-dynamics of the environment which surrounds the gears, namely windage, fluid trapping and squeezing between meshing gear teeth and inertial losses resulting by the impinging oil jets, usually adopted in high speed transmission for cooling and lubrication purposes. The relative magnitude of these phenomena is strongly dependent on the operative conditions of the transmission. While load-dependent losses are predominant at slow speeds and high torque conditions, load-independent mechanisms become prevailing in high speed applications, like in turbomachinery. Among fluid-dynamic losses, windage is extremely important and can

dominate the other mechanisms. In this context, a new test rig was designed for investigating windage power losses resulting by a single spur gear rotating in a free oil environment. The test rig allows the gear to rotate at high speed within a box where pressure and temperature conditions can be set and monitored. An electric spindle, which drives the system, is connected to the gear through a high accuracy torque meter, equipped with a speedometer providing the rotating velocity. The test box is fitted with optical accesses in order to perform particle image velocimetry measurements for investigating the flow-field surrounding the rotating gear. The experiment has been computationally replicated, performing RANS simulations in the context of conventional eddy viscosity models. The numerical results were compared with experimental data in terms of resistant torque as well as PIV measurements, achieving a good agreement for all of the speed of rotations.

Time resolved PIV revealed strong instabilities in the flow field generated by the gear, highlighting the importance of performing unsteady simulations for a better modelling of this component. Results have been post-processed in terms of Fast Furier Transform (FFT) and Proper Orthogonal Decomposition (POD) in order to provide a reliable data base for future unsteady simulations.

In design phase it is important to predict the losses increase due to the lubricating oil jet impact on the spur gear varying the different geometrical and working parameters such as the jet inclination, distance and the oil mass flow rate and temperature.

For this reason the test rig was equipped with an oil control unit able to provide a controlled oil mass flow rate to a spray-bar placed within the test chamber. The oil jet can be regulated in terms of pressure and temperature, in such a way the mass flow rate can be imposed and measured by means of flow-meters. The spray-bar is equipped with a circular hole, its position can be varied as well as the inclination angle.

High speed visualizations were performed for every tested condition in order to deepen the physical understanding of the phenomena and to obtain more information on the lubrication and cooling capability. The

high speed camera was placed in front of the gear exploiting an optical access while a halogen lamp was used to provide the proper lightening necessary due to the very low exposure time of the acquisitions.
In every test the power losses were also measured using the torque-meter, results were post-processed in order to insulate the torque increase due only to jet injection. The collected data were used for the validation of a simple 0D model able to well predict power losses due to jet injection under certain conditions.

Contents

Abstract **v**

Contents **xi**

List of Figures **xvii**

List of Tables **xix**

Nomenclature **xxi**

1 Introduction **1**

Introduction **1**

1.1 Aim of the work 9

2 Technical background **11**

Technical background **11**

2.1 Windage power losses 13

2.1.1 Experimental investigations 14

2.1.2 Numerical investigations 18

2.2 Oil jet injection losses 21

2.3 Gear meshing losses 27

3 Experimental Setup **29**

Experimental Setup **29**
3.1 Test Rig 31
3.2 Lubricating Oil Control Unit 34
3.3 Oil Jet Control Unit 35
3.4 Measurement Techniques 36
3.4.1 Power Losses Measurement 37
3.4.1.1 Torque 37
3.4.1.2 Temperature and Pressure Sensors 38
3.4.1.3 Drive Train Friction Losses Characterization 40
3.4.2 PIV Measurement and Oil-Jet Visualization 42
3.4.2.1 Fundamentals of PIV 43
3.4.2.2 PIV Setup 44
3.4.2.3 Oil Jet Visualization Setup 47
3.4.3 Uncertainty analysis 48

4 Windage losses **51**

Windage losses **51**
4.1 CFD Analysis 51
4.1.1 Computational Domain and Boundary Conditions 51
4.1.2 Numerical Setup and Grids 52
4.2 Air Windage Power Losses 53
4.2.1 Windage Correlation 58
4.3 PIV Measurements 62
4.3.1 XY Plane 62
4.3.2 YZ Plane 67
4.3.3 Unsteady Phenomena 77
4.3.3.1 Time-variant flow fields 77
4.3.3.2 Spectral analysis 79
4.3.3.3 Proper Orthogonal Decomposition (POD) analysis 84

5 Oil jet **93**

Oil jet **93**
5.1 Theoretical 0D model 94
5.2 Oil jet break-up regimes 96
5.3 High speed visualizations 100
5.3.1 Laminar jet 101
5.3.2 Turbulent jet 103
5.4 Power losses 109

6 Conclusions and future work **117**

Conclusions and future work **117**

Bibliography **127**

List of Figures

1.1 Basic structure of a turbofan engine [1] 3
1.2 Conventional and geared turbofan engine with BPR = 10 [2] 4
1.3 Pratt & Whitney PW1000G engine cross section [3] . . . 5
1.4 Rolls-Royce UltraFan high-bypass geared turbofan engine cross section [4] 7
1.5 Rolls-Royce UltraFan high-bypass geared turbofan, view of the gearbox [4] 8
1.6 A scheme of the oil jet cooling mechanism 8

2.1 Relative contributions of losses for different operating conditions [5] 12
2.2 A scheme of all fluid-dynamic losses source 13
2.3 Sketch of the flow pattern observed by Dawson [6] 16
2.4 Test rig used by Diab et al. [7] 17
2.5 Comparison of experimental results of Diab et al. [7] (black dots) with Anderson and Loewenthal [5] (left) and Dawson [6] (right) 17
2.6 Flow-field inside a tooth cavity, velocity vectors relative to rotating reference frame [8] 19
2.7 Computational domain and casing geometrical parameters for CFD investigation performed by Fondelli [9] 21
2.8 Oil jet penetrating tooth space and impinging tooth; speed, 4920 rpm; oil pressure, $10.5 \cdot 10^4 Pa$ [10] 24

2.9 Oil jet impingement and subsequent penetration into the tooth space; (a) 4920 rpm and oil pressure of $14 \cdot 10^4 Pa$; (b) 2560 rpm and oil pressure of $13 \cdot 10^4 Pa$ [10] 25
2.10 Centrifugal and Coriolis accelerations above and below impingement on gear tooth [11] 26

3.1 View of the laboratory 30
3.2 View of the test cabin 30
3.3 View of the test rig 32
3.4 Back plate for single gear (left) and meshing gears (right) configurations 32
3.5 Sketch of gear and spraybar 34
3.6 Oil control unit scheme for bearings cooling and lubrication 35
3.7 Oil control unit scheme for oil jet generation 36
3.8 T11 Bearingless Rotary Torque Transducer 38
3.9 The T11 Transducer installed on the drive train 38
3.10 Devices power supply and acquisition units 39
3.11 Friction losses of the drive train due to lubricant oil temperature, evolution with gear pitch line velocity V_p 40
3.12 Friction losses of the drive train due to lubricant test chamber pressure, evolution with gear pitch line velocity V_p . . 41
3.13 Comparison between experimental and calculated friction losses 42
3.14 Basic principles of PIV 44
3.15 PIV measurement equipment and setup 45
3.16 Example of camera and optic configuration 46
3.17 PIV investigated planes 47
3.18 High speed visualization setup 48
3.19 Uncertainty evolution with torque 49

4.1 Computational domain 52
4.2 Computational grid 53
4.3 Test rig in free gear configuration 55

4.4 Power losses comparison between Diab's correlation and free and enclosed gear configurations 55
4.5 Power losses comparison between Diab's correlation and free and enclosed gear configurations imposing $h_1 = 0$ . . 56
4.6 Power losses for different working pressures 57
4.7 Power losses vs air density 57
4.8 Power losses vs pitch velocity: comparison between CFD and experiments 58
4.9 Results expressed in dimensionless terms 59
4.10 Diab's definition of air passage area [7] 60
4.11 Comparison between CFD and experiments and Owen correlation 4.5 61
4.12 C_m correlation's error 62
4.13 V/V_p and streamlines in XY plane 63
4.14 Scheme of the angular interval for the tangential velocity extrapolation 64
4.15 Tangential velocities for test at 25 m/s 64
4.16 Swirl comparison at angle zero 65
4.17 Comparison between PIV and CFD in XY plane 66
4.18 PIV velocity and vector maps in plane YZ 68
4.19 Seven traverse position for PIV velocity profiles extraction 69
4.20 PIV radial velocity profiles at T1, T4, T7: comparison between all tests 70
4.21 PIV axial velocity profiles at T1, T4, T7: comparison between all tests 71
4.22 PIV radial velocity profiles scaled on pitch velocity at T1, T4, T7: comparison between all tests 73
4.23 PIV axial velocity profiles scaled on pitch velocity at T1, T4, T7: comparison between all tests 74
4.24 CFD results for YZ plane 75
4.25 PIV velocity and vector maps in plane YZ 76
4.26 PIV velocity and vector maps in plane YZ 78
4.27 PIV velocity and vector maps in plane YZ 78

4.28 Lines on which velocity time evolution was extracted . . . 79
4.29 PIV velocity spectra in test at $V_p = 25m/s$ 80
4.30 Velocity oscillating mode at 52 Hz for $V_p = 52Hz$ 81
4.31 Flow field comparison after a period of time $T = 1/f$ . . . 82
4.32 Velocity oscillating mode at 12 Hz for $V_p = 12Hz$ 83
4.33 Energy fraction and cumulative curve for the first 25 modes for $V_p = 100m/s$ 85
4.34 POD modes 1 to 3 for test at $V_p = 25m/s$ 87
4.35 POD modes 4 to 7 for test at $V_p = 25m/s$ 88
4.36 POD modes 8 to 10 for test at $V_p = 25m/s$ 89
4.37 Energy fraction and cumulative for the first 25 modes for $V_p = 100m/s$ 90
4.38 POD modes 1 to 3 for test at $V_p = 100m/s$ 91

5.1 Oil jet angular direction definition 93
5.2 The four break-up zones 97
5.3 Typical image of the four primary breakup regimes [12] . 98
5.4 The regimes of liquid breakup as a function of Reynolds number and ambient gas density [13] 99
5.5 The regimes of liquid breakup at different We_{cf} for a laminar jet 100
5.6 Discharge coefficient vs Reynolds number for the tested spray-bar 101
5.7 Effect of We_{cf} defined using gear pitch pitch velocity on a laminar oil jet 102
5.8 Oil jet break-up: effect of Re_j at ambient conditions . . . 103
5.9 High speed visualizations in Take-off condition and $\alpha = 0$ 105
5.10 High speed visualizations in Cruise condition and $\alpha = 0$. 106
5.11 High speed visualizations in Take-off condition and $\alpha = 40$ 107
5.12 High speed visualizations in Cruise condition and $\alpha = 40$. 108
5.13 Power losses due to oil injection at ambient pressure: effect of pitch velocity 109
5.14 Power losses for oil jet injection at $\frac{L_j}{D_p} = 0.013$ 110

5.15 C_m vs $\frac{\rho_j V_j}{\rho_{air} V_p}$ for oil jet injection at $\frac{L_j}{D_p} = 0.013$ 111
5.16 Effect of pressure on oil injection power losses 113
5.17 C_m vs $\frac{\rho_j V_j}{\rho_{air} V_p}$ for oil jet injection at $\frac{L_j}{D_p} = 0.013$ 114
5.18 Power losses due to oil injection delivered from $\frac{L_j}{D_p} = 0.5$ at $V_p = 100m/s$ and $\alpha = 60^\circ$ effect of ambient pressure . . 115

List of Tables

3.1 Gear characteristics 33

4.1 Results of mesh sensitivity. 53
4.2 Coefficients of the Diab's correlation 54

5.1 Oil injection test matrix 94

Nomenclature

NOMENCLATURE

α	Oil-jet injection angle	$[^{\circ}]$
C_m	Moment coefficient	$[-]$
C_d	Discharge coefficient	$[-]$
D	Diameter	$[m]$
F	Forces	$[N]$
L_f	Gear face lenght	$[m]$
L_j	Jet to Gear distance	$[m]$
$\dot{m}$	Mass flow rate	$[kg/s]$
ρ	Density	$[kg/m^3]$
ω	Rotational speed	$[rad/s]$
P	Power	$[W]$
r	Radial coordinate	$[m]$
R	Radius	$[m]$
Re	Reynolds number	$[-]$
Re_ϕ	Rotational Reynolds number	$[-]$
τ	Torque	$[Nm]$
T	Temperature	$[K]$
V	Velocity	$[m/s]$
Z	Number of teeth	$[-]$

Acronyms

BPR	Bypass Ratio
CFD	Computational Fluid Dynamics
GTF	Geared Turbofan
PCA	Principal Components Analysis
PIV	Particle Image Velocimetry
POD	Proper Orthogonal Decomposition
RANS	Reynolds Averaged Navier Stokes
SFC	Specific Fuel Consumption
THT	Technology for High Temperature
VOF	Volume Of Fluid
WPL	Windage Power Losses

Supscripts

corr	Correlation
exp	Experimental
j	Jet
is	Isentropic
oil	Referred to oil
p	Pitch
real	Real
t	Tangential

Chapter 1

Introduction

In the last years huge efforts have been made by the scientific community with the goal of finding innovative ways for reducing environmental and climate impact from energy production and transports.
Considering the ever growing demand for air transportation, aircraft engines play an important role in this scenario, for this reason researchers are looking towards alternative engine solutions aimed at a significant reduction in emissions, noise and fuel consumption [14].
The efficiency increase of aero-engines can be described by the Specific Fuel Consumption (SFC) parameter, defined as the ratio between the fuel mass flow rate and the relative thrust produced:

$$SFC = \frac{\dot{m}_{fuel}}{F} \left[\frac{\frac{g}{s}}{kN} \right] \tag{1.1}$$

As far as this parameter is reduced the efficiency rises. Increasing the thermodynamic and propulsion efficiencies may be a way for reducing the SFC [15]. The efficiency of conventional gas turbine cycles can be improved by augmenting the overall pressure ratio and the turbine entry temperature. In this field there is not so much room for improvement considering that temperatures of 1900 - 2000 K have been already reached at the turbine entry and further increase will be bound to future ad-

vancements in material and cooling technology [2], on the other hand the increase of pressure ratio above 40 does not bring significant benefits on the fuel consumption[16]. Nevertheless an alternative way may be found for improving the fuel efficiency of aircraft engines as the increase of the propulsive efficiency.

The most applied technology in modern aircraft is the turbofan engine, showed schematically in Figure 1.1, in which the propulsion is assured by a large fan moved by a gas turbine and positioned in front of it.

In addition to the fan, the main components of this kind of engine are the low and high pressure compressor, the combustion chamber, the high and low pressure turbine and finally the exhaust nozzle. Air is firstly compressed increasing its pressure, it is then sent to the combustion chamber, where it reacts with fuel, and then to the turbine where the energy is extracted from the hot gas.

Low pressure and high pressure components are usually connected with two different concentric spools rotating at different velocities, lower for the low pressure shafts, which supports also the fan.

As sketched in Figure 1.1, the overall amount of air frontally ingested passes through the fan and is split in two parts, one flows within the engine and is called core flow, the other, named by-pass flow, passes between the engine and the nacelle and is the main contributor to the aircraft propulsion. The ratio between the two mass flow rates is the so called by-pass ratio BPR, typical vales of BPR for current conventional turbofan are in the 6-8 range [15]. The thrust, defined as the product of the air mass flow rate and the change in velocity given to that air, is the parameter used to measure the amount of propulsion granted by an engine. The propulsion efficiency can be improved by processing a larger amount of air flows with a reduced pressure ratio, rather than vice versa. This means that a higher BPR and lower Fan Pressure Ratios are beneficial for reducing the SFC. This goal can be achieved in conventional turbofan engines by increasing the fan diameter and consequently reducing the low pressure spool speed. Another beneficial effect of adopting a higher BPR is in terms of noise and emissions reduction.

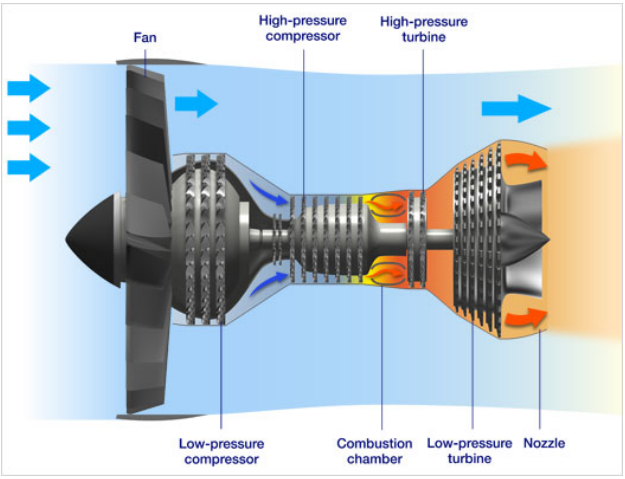

Figure 1.1: Basic structure of a turbofan engine [1]

As a consequence of velocity reduction, the number of stages for the low spool compressor and turbine must to increase in order to retain satisfactory efficiencies and pressure ratios for these components. Moreover higher torques would be applied to the shaft making necessary to adopt wider spool diameters, and hence wider core dimensions. Also the low pressure turbine diameter and its number of stages need to increase, in order to run a bigger diameter fan.

Given all these constrains, the maximum gain in propulsive efficiency is limited for conventional turbofan engines and for BPR higher than 10 engine would need an excessive number of stages.

Summarizing the considerations made, modern two-spool aero-engine configurations having fan and LP compressor and turbine connected on the same shaft and hence rotating at same velocity, encounter many limitations. The speed is too high for the fan, resulting in noise emissions and low efficiency, and too low for compressor and turbine, requiring more stages.

This limit can be overcome by adopting an innovative layout concept

introduced by Pratt & Whitney in '90s: the so called Geared TurboFan (GTF) Engine. In this new technology a power epicyclical gearbox is interposed between the fan and the low pressure spool, allowing both of them spinning at their optimum speed. Such configuration allows to

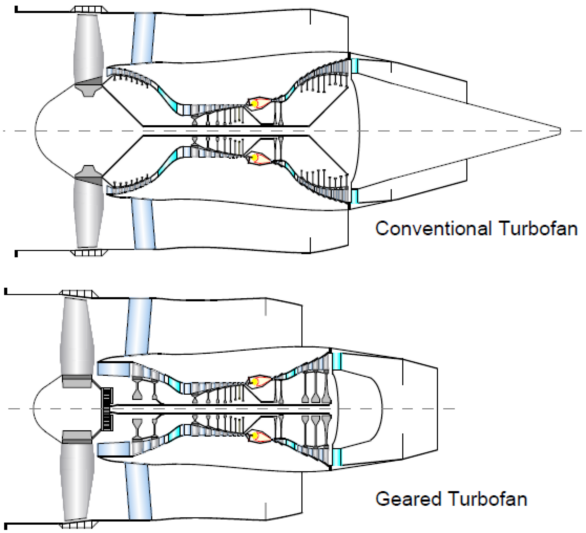

Figure 1.2: Conventional and geared turbofan engine with BPR = 10 [2]

select the proper fan speed in order to increase efficiency and reduce noise and, at the same time, to maintain a high LP shaft velocity reducing the number of stages of LP compressor and turbine [17].
In 2009 Kurzke [2] compared the conventional and geared turbofan configurations, for equal blowing ratio (BPR=10), thrust and SFC. He proposed the two layouts exposed in Figure 1.2, from which it is easy to note the lower number of components present in the geared configuration. Nevertheless the weight between the two configurations may be similar due to presence of the gearbox system and the relative oil lubricating and cooling system.

However the real innovation of the geared turbofan technology is the possibility of reaching higher BPR values absolutely prohibitive with the conventional technology.
Recently a new GTF engine called Pure Power PW1000G has been developed by Pratt & Whitney, it develops thrust in the range of 10000-40000 lbf (44.5 -177.9 kN) [3].
In September 2011 this engine (model PW1524G) for the Bombardier CSeries aircraft completed its first flight test program: 25 flights for an overall amount of 115 hours. It has a BPR=12 and nominal thrust of 24000 lbf (107 kN) and a claimed significative improvement in fuel burn with respect to current best engines, as well as a reduction in noise emissions below today's most stringent standards, Figure 1.3 shows a cross section of the engine.

The gearbox is a planetary gear system composed of a sun gear, con-

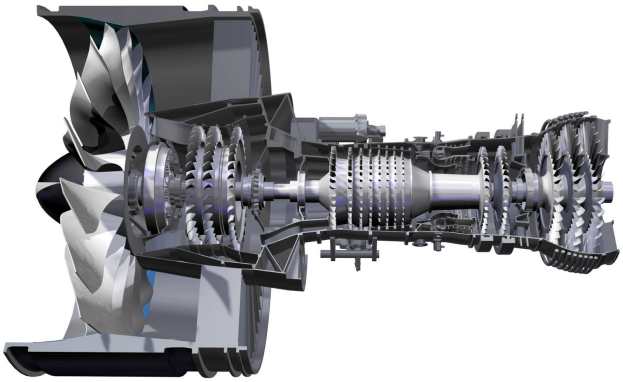

Figure 1.3: Pratt & Whitney PW1000G engine cross section [3]

nected with the driving shaft, and five planetary gears, enmeshing with sun and a static annular gear. A carrier holds the planetary gears and transmits the torque to the fan.
The efficiency of a GTF engine is directly affected by the gearbox given its weight contribution, internal power losses and lubrication system. For

these reasons the evaluation of its structure and performance is necessary to improve design optimization and efficiency increase.
Among the power transmission methods, gears are the most competitive, they can reach values of efficiency up to 99% [8].
Power losses occurring in a gear system can be divided in two main groups: load-dependent and load-independent (or spin power) losses [18].
The first category is related to the torque transmission and include meshing (sliding and rolling) and bearing losses. The load-independent on the other hand, are associated with fluid-dynamic phenomena of the environment surrounding the gears, i.e. windage and lubrication effects.
The fluid-dynamic losses can be caused by many sources, among them the primary ones are the windage, due to oil/air drag on the periphery and faces of the gears, lubrication losses, pocketing/squeezing of lubricant from the cavities of the gear mesh, and viscous dissipation of bearings.
The two categories can have different weight on the overall power losses, depending on the operative conditions on the transmission: load-dependent losses are predominant in low speed applications mostly because of the little importance of fluid-dynamic effects, which on the contrary, become important in high speed applications, such as in turbomachinery.
In the most stressed applications, gears can transmit power up to 100 MW, in these conditions even very low losses, in the order of 1%, mean a significant amount of power [19].
All the power dissipated through losses is converted in heat that needs to be removed by the lubricating system, in order to avoid any gear malfunction. The higher is the heat to be removed the more oil is necessary as well as heat exchangers dimensions and, at the end, the larger is the weight.
For this reason, geared turbofan engine technology has been used so far for limited power applications, for example the Pratt & Whitney PW1000G engine is able to develop a maximum thrust of about 178 kN. This engine is indeed developed for low and mid-thrust market, Rolls-Royce is recently developing the so-called UltraFan high-bypass geared turbofan, one of the first attempts to look forward the mid and high thrust applications, up

to the 100000 lbf (445 kN) power range.

Figure 1.4 shows the cross section of the engine, the engine is expected

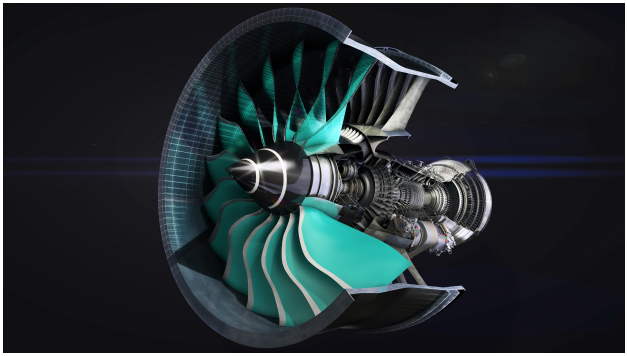

Figure 1.4: Rolls-Royce UltraFan high-bypass geared turbofan engine cross section [4]

to be ready for service in 2025 offering the 25 % improvement in fuel burn and emissions with respect to the same baseline.

Thanks to an innovative gearbox architecture, an indicative image is reported in Figure 1.5, the engine will have a very high by-pass ratio of 15:1.

Concerning the gears cooling and lubrication, several methods can be adopted depending on the pitch line velocity. For the aeronautical applications, considering the very high velocities and powers involved, a series of oil jets can be injected by nozzles in the meshing zone (see Figure 1.6). The oil impacting on the teeth surface generates an impingement point removing heat from it, subsequently it creates a film layer that helps reducing the frictional losses. This layer needs to be continuously fed because the centrifugal forces fling the oil off the gear shortly after its application [20].

The system sees the contemporary presence of oil droplets, generated by spray system and fling off mechanisms, continuous oil jet, and air all interacting within the gearbox and eventually affecting cooling and

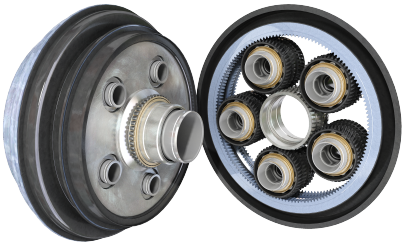

Figure 1.5: Rolls-Royce UltraFan high-bypass geared turbofan, view of the gearbox [4]

lubrication capabilities.
Given the multiphase characteristic of the problem, it is necessary to approach the study of the epicyclic gear train step by step, starting from simpler geometries and decoupling the physical phenomena involved.

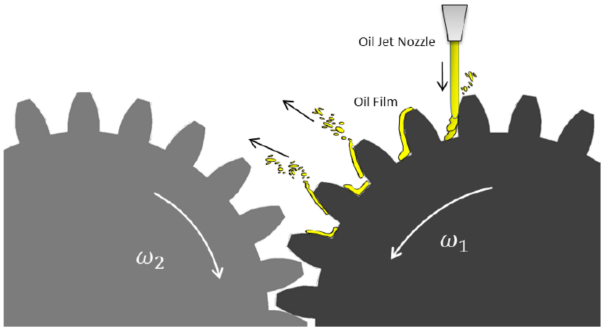

Figure 1.6: A scheme of the oil jet cooling mechanism

1.1 Aim of the work

In the past years many efforts have been made to develop correlative methods able to evaluate and predict load-dependent losses, much work is still necessary in characterizing fluid-dynamic losses.
For this reason nowadays, also considering the growing request of gears in high speed applications, it is important to deepen the knowledge of the fluid-dynamic phenomena governing the load-independent power losses and to provide correlative approaches with reduced uncertainty [20].
Considering the complexity of the gearbox, the rotating parts generate a complex flow field around them, in addition the oil injected can interact both with solid elements and air causing break-up and particle generation.
In summary, a high number of physical phenomena take place in this component and have a mutual interaction, moreover the phenomenon has multiphase characteristics. For this reason it does not make any sense to study a complete epicyclic gearbox without a deep knowledge of every loss contribution.
In this contest the Department of Industrial Engineering of the University of Florence (DIEF), started a research project aimed at studying fluid dynamic losses described above, both experimentally and numerically. Such research was developed in cooperation with GE Avio S.R.L., global leader in designing and manufacturing of power gearboxes for aero-engine applications.
In particular, the work reported in this thesis deals with the results obtained from a new High Speed Test Rig able to reproduce the fluid dynamic losses affecting a spur gear having typical dimensions and working conditions of the ones adopted in gearboxes for high speed and power applications.
The test rig setup can be changed in order to mount a gears pair reproducing also meshing losses, results from this configuration are not reported here because they are ongoing.
In this first experimental campaign the fluid dynamic losses due to air windage at different gear rotating velocities were reported, the effect of

air pressure reduction was also taken into account considering the aeronautical purpose of the research. Effect of lubricant oil injection was also reproduced and observed both in terms of power losses and high speed visualizations in order to gain knowledge on the break-up phenomena generated within the gearbox.
During the project numerical simulations were carried out with the two objectives of finding a good predictive model for this kind of components and deepen the analysis of experimental evidence, however the results from CFD will not find a central role in this work.

Chapter 2

Technical background

The research presented in this work deals with experimental investigation on fluid dynamic losses in gearbox systems used for aero-engine applications. The importance and the originality of this work may be appreciated after an accurate review of the state of the art: experimental and numerical studies found in open literature will be presented in the following section with the double objective of contextualize the problem and to show where are the missing pieces that we are going to fill.
As already mentioned the power losses in a gearing system can be distinguished in load-dependent and load-independent. The first group deals with mechanical losses, due to friction between meshing gears or rolling elements and races of the bearings, it is for this reason related to load transmission. The second category on the contrary, is not affected by the load transmitted by the system but is a consequence of the environment surrounding the gears. The source of losses can be in turn caused by the atmospheric condition or the lubrication method. We talk of Windage when referring to the first case, in particular to the power spent to drag the gear in its environment. The lubrication effects are multiple and can be divided in three main categories: churning, oil-jet impingement, oil pumping. Churning is the power dissipated by a gear rotating in an oil bath, this kind of system however is rarely used in high speed applications.

Oil-jet impingement affects power loss both through its jet momentum and by modifying the air-oil ratio close to the tip radius. Oil-air mixture pumping is a phenomenon that occurs due to the pocketing and squeezing of oil from the meshing cavities. All the reported sources of losses are schematically reported in Figure 2.2. The contribution of every source of

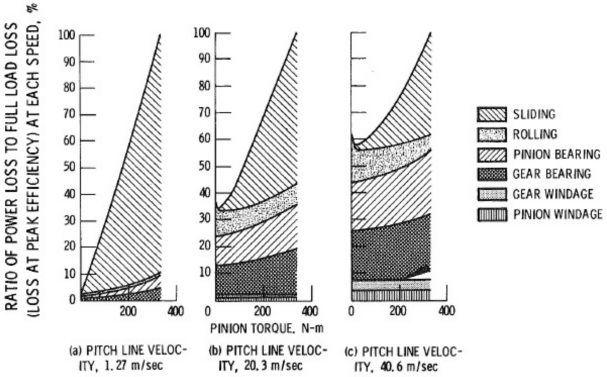

Figure 2.1: Relative contributions of losses for different operating conditions [5]

losses on the overall budget is not constant for every application but, as showed in Figure 2.1, in low velocities and high load conditions, friction-induced losses are predominant, while bearing and windage losses increase significantly in percentage at higher speeds. It can also be possible for windage losses to equal or overcame the meshing ones [5, 21, 22], Figure 2.2. Given their high level in every conditions, meshing and bearings losses have been deeply investigated while windage have been somewhat neglected so far.

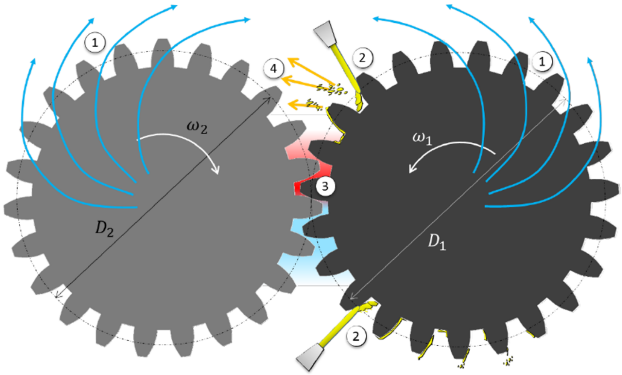

Figure 2.2: A scheme of all fluid-dynamic losses source

2.1 Windage power losses

During the past years attention has been paid to windage of rotating disks, mostly for gas turbine applications such as rotor-stator cavities. Many researchers focused their work on this matter providing analytical or empirical correlations, two pioneers have been Von Karman [23] and Goldstein [24] at beginning of the past century and many others in following years until nowadays.
It is increasingly accepted that torque, related to both sides of a disk, depends linearly by the fluid density, in a quadratic way by the angular velocity and by a fifth power of the disk radius. Two dimensionless parameters have been adopted for describing the torque losses relative to a rotating disk:

- Rotational Reynolds number:

$$Re_\phi = \frac{\rho \Omega R^2}{\mu} \tag{2.1}$$

- Moment coefficient:

$$C_m = \frac{\tau}{0.5 \rho \Omega^2 R^5} \tag{2.2}$$

These parameters can still be useful for the description of a spur gear, as well as the many correlations developed can still be applied to gear's lateral surfaces. Unfortunately the presence of gear's teeth is not negligible and new studies have been necessary for their description.

2.1.1 Experimental investigations

One of the first works dealing with windage for a spur gear was made by Anderson and Loewenthal [25] which provided an algebraic expression taking into account gear geometrical parameters. They proposed also a correction parameter in order to account for air density variation around the gear, due to possible mixture with oil particles.
The formula obtained is reported below in equation 2.3:

$$WPL = C_4\left(1 + 2.3\frac{b}{R}\right)\rho^{0.8}N^{2.8}R^{4.6}\mu^{0.2} \tag{2.3}$$

Where $C_4 = 2.04 \cdot 10^{-8}$ (SI units). In the equation, b is the face width, R the pitch radius, ρ the air density, N the rotational speed and μ the air viscosity. The next year, the same authors compared the proposed model with available experimental data finding good agreement, moreover they experienced the effect of various parameters such as speed, size, pitch, lubricant viscosity and face width, finding that the most influential are pitch radius and rotational speed [5].
Few years later Dawson [6] presented a paper in which reported a systematic research on windage power losses due to gears rotating in free air. This work was carried out on a self-made test rig composed of a steel shaft driven by an electric motor through a V-belt which could be unhooked to decouple shaft and motor. This mechanism allowed Dawson to speed up the gear to a certain velocity and then disconnect the shaft in such a way he could graphically calculate the derivative of speed and the moment of inertia of the apparatus, hence obtaining the resistant torque of the decelerating gear at given instants. Spur gears were machined of hardboard, he tested many geometries at a maximum velocity of 1500 RPM.

The results of this research were in agreement with the previous one: similar power proportionality of speed and diameter with the WPL were indeed obtained.
Dawson tested cylinders of the same diameters of gears and noticed that the WPL increased up to 5 times when teeth were present, this fact revealed that the teeth, and particularly their shape, are responsible for higher power losses.
He tried to deepen the fluid dynamic knowledge of the phenomenon by using smoke to observe the air flow path around the gear and discovered that air is ingested axially in the spacing between the teeth and is then expelled radially from the gear centerline. A sketch of this phenomenon is showed in Figure 2.3 where also the differences between spur and helical gears are reported. He so observed that imposing a blockage to air ingress the WPL strongly decreased.
The final consideration made by Dawson concerned effect of shrouding the gear, again he found beneficial effects as good as the clearance was reduced.
All these results were used to develop an empirical formula, reported in equation 2.4:

$$WPL = N^{2.9}\left(0.16D^{0.39} + D^{2.9}b^{0.75}m^{1.15}\right) \cdot 10^{-20}\psi\lambda \qquad (2.4)$$

Where N is the rotational speed (RPM), D the root diameter (mm), b the face width (mm), m the module (mm), ψ is a function of the environment density, λ represents the effect of the gear case.
More recently, in 2003, Diab et al. [7] performed an experimental investigation testing four gear's geometries as well as a flat disk. They used a test rig and measurement technique similar to the ones developed by Dawson even if he could reach higher velocities, given the more advanced technology at his disposal, a sketch of the test rig is reported in Figure 2.4.

They compared the obtained results with the values calculated from the correlations by Anderson and Loewenthal (eq. 2.3) and Dawson (eq. 2.4) observing a fairly good agreement, even if the former underestimates

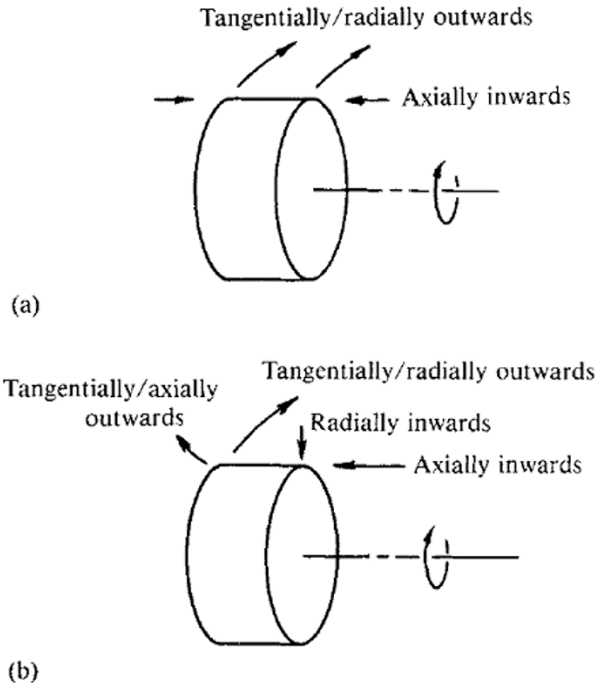

Figure 2.3: Sketch of the flow pattern observed by Dawson [6]

losses for small- and medium-sized gears, while the latter overestimates windage for every gear as reported in Figure 2.5. The new experimental database was used to develop two different predictive approaches: the first was a dimensional analysis performed with dimensionless groups of variables which are relevant for describing the phenomenon like gear geometry, speed and fluid properties. The second method was inspired to the discoveries of Dawson and was based on a fluid dynamic model of the phenomenon: lateral surfaces and teeth were treated separately.
The dimensional correlation was chosen to compare the experimental results obtained in the present activity, while the fluid dynamic analysis

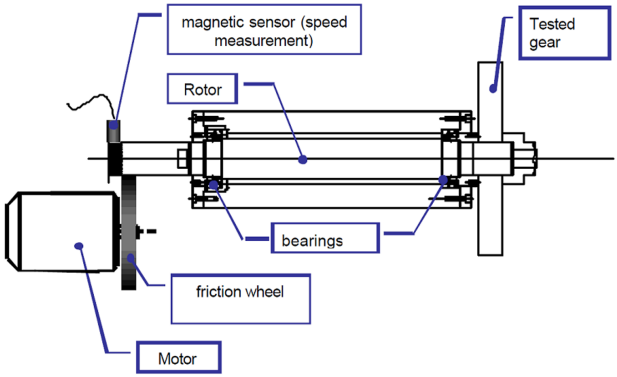

Figure 2.4: Test rig used by Diab et al. [7]

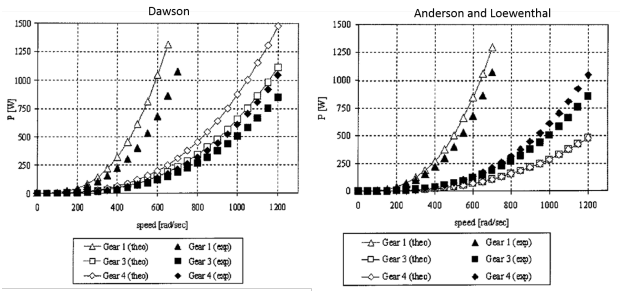

Figure 2.5: Comparison of experimental results of Diab et al. [7] (black dots) with Anderson and Loewenthal [5] (left) and Dawson [6] (right)

helped to explain the results, for this reason both the method will be better explained in chapter 3. What is worth to notice is that, even if all the presented work tried to find a correction to the effect of air density, mostly for the need of considering the possible presence of air-oil mixture, none of them tested the effect of a reduced pressure, that is peculiar in flight applications.

Another aspect fundamental for windage modelling is the air flow field

around the gear, these pioneer works revealed the main flow structures by qualitatively observing a smoke fog, but a more accurate and quantitative measurement of the flow field is more and more necessary, mostly within the teeth spacing, the place where the loss mechanism is generated.

2.1.2 Numerical investigations

In the last years, the ever growing development of computational resources and numerical tools, the windage problem was approached also by means of numerical simulations. Using CFD in such kind of problems brings many advantages: first of all it is possible to decouple every source of losses analysing separately for example viscous or pressure effect thank to the Navier-Stokes equations. Moreover many gear geometries and working conditions difficult to realize in laboratory can be studied, being the only limit the computational resources. These characteristics make CFD analysis appealing for industrial applications.
The reliability of such tool has been improved in the last years, in 2008 Eastwick and Johnson [26] provided a review on the experimental and numerical results for gear windage power losses, they highlighted the limits of the CFD models applied so far.
One of the first works dealing with numerical simulation on a spur gear was performed by Al-Shibl et al. [8] which performed a CFD 2D simulation, comparing their results with available experimental data. They found out that, even if the trend with rotating speed was similar, the CFD model underestimated the power losses in every condition. The conclusion draw by this experience was that a 2D simulation is not able to reproduce the phenomenon because it is strongly three-dimensional, the power losses contributions of the teeth are not equally distributed along the face width but are concentrated on the lateral zones, where the air ingresses the spacing.
Nevertheless thanks to the work of Al-Shibl, secondary flows were identified within the teeth spacing by calculating the flow field in the gear rotating reference frame, see Figure 2.6. They are composed of two counter-rotating vortical structures generated by a pressure gradient present between the

two surfaces. Where the flow impinges on the leading edge of each tooth indeed, there is a stagnation point from which the pressure gradient arises. This mechanism was attributed to be the responsible for power losses

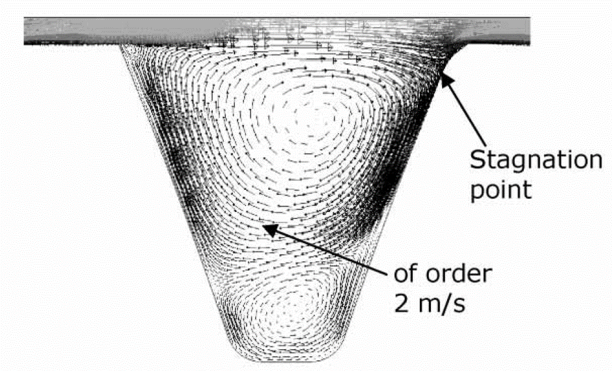

Figure 2.6: Flow-field inside a tooth cavity, velocity vectors relative to rotating reference frame [8]

much greater than that due to viscous effects, hence much more influential on windage.

A step forward was done by Marchesse et al. [27] in 2011, they performed both 2D and 3D simulations. The former gave the same vortical structures, obtained by Al-Shibl, within the teeth spacing, the latter showed that the flow field changes along the tooth face width due to air suction from the lateral openings and its ejection from the centerline. They also showed that the predictability of the power losses is largely increased adopting 3D simulations.

A 3D unstructured moving mesh method was implemented by Hill et al. [20, 28], they validated their predictions against data from Diab et al. [7] and then used it to investigate the aerodynamics of single gear in various shrouding configurations. They compared the results with experiments on a dedicated test rig finding good agreement. They observed for all the configurations that the pressure field on the tooth surface is the

dominant physical mechanism responsible for power losses, shrouding the gear provides a mitigation on its magnitude but not in its dominance in the loss budget.
Further studies on the shrouding effects were performed at the Department for Industrial Engineering of the University of Florence (DIEF) by Fondelli and reported in his PhD thesis [9]. He reproduced one of the gears tested by Diab et al. rotating in free air conditions and validated a 3D model imposing several symmetry conditions in order to reduce computational costs. The model was then exploited imposing shroud geometries in which the effect of axial (δ_{axial}) and radial (δ_{radial}) distances were investigated, see Figure 2.7. He found out that the main parameter affecting the windage power losses is the ratio between the air volume contained in the shroud and the gear one. The data were collected to create a coefficient, function of the volume ratio and the rotational Reynolds number, able to correct the correlations obtained in free air conditions taking into account the shroud.

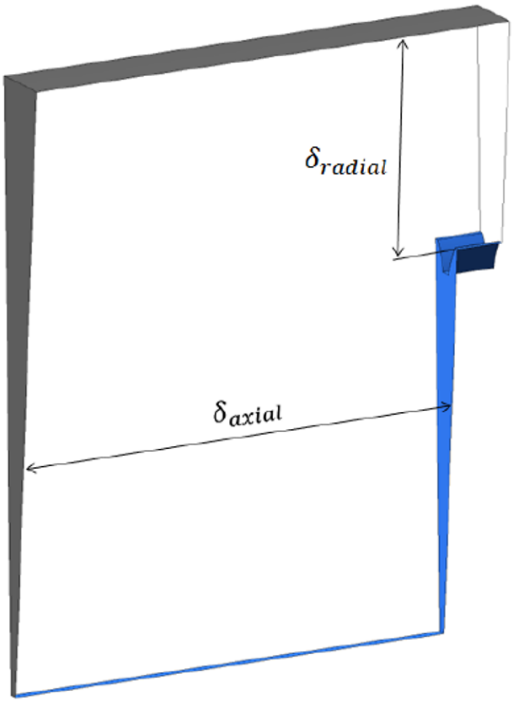

Figure 2.7: Computational domain and casing geometrical parameters for CFD investigation performed by Fondelli [9]

2.2 Oil jet injection losses

Failure phenomena occurring in gearing transmissions, such as scoring and scuffing, can be reduced if a proper temperature is maintained on the gear tooth surfaces, that is a crucial parameter mostly in high speed and heavy load gears [29].
Therefore the teeth need to be sufficiently lubricated, to reduce the friction during the meshing, and cooled to reduce the risk of gearbox failure.
Several methods have been adopted to reach this goal, mostly depending

on the pitch line velocity and load: when both of them are low indeed, the lubrication method is not critical, given the low heat generated [30]. In such conditions the splash method is usually employed, in which the gear is partly submerged in oil, therefore higher velocities mean very strong power losses increase [31].
In aeroengine applications gears work at high speed and high load conditions, hence the lubricant is injected by a system of nozzles in the for form of jets. They are directed towards the gear tooth surface and is so supplied to each one once per revolution. This method provides an adequate lubrication and high cooling performances given the heat transfer rates of impinging jets [32].
The power losses related to this method are due to momentum increase of the oil injected during its interaction with teeth. Hence it is important to know which is the interaction between oil and gear, in order to reduce the oil mass flow necessary or its effect in terms of power losses.
It can be useful to define two parameters such as the oil jet impingement depth and the penetration depth of lubricant penetration: the first is the point where the oil jet collides with the tooth surface, the other is the depth of lubricant penetration, this one is usually the higher [10].
Akin et al. [10] experimentally investigated a spur gear oil jet lubrication system, varying both gear and oil-jet velocity. The gear had a 88.9 mm pitch diameter, a tooth height of 7.62 mm and a pressure angle of 20 degree, while the speeds were 2560 and 4290 rpm, which correspond to gear pitch line velocities of 12 and 23 m/s. A nozzle with 80° spray angle and an orifice of 1.1 mm diameter was adopted to provide the oil jet. The injection pressure was varied for every rotating speed tested in order to separately analyse the effect of jet velocity and obtaining different impingement and penetration depths.
In all the tested conditions the oil were injected both as a continuous stream or large droplets, showing that droplets are too much subjected to windage effect for higher velocities.
The oil jet penetration was observed by means of a high speed camera, the lubricant, illuminated with a xenon lamp, was seeded with lithopone

pigments to increase its light reflection.
It was one, if not the sole, of the first works reporting oil visualizations, Figure 2.8 shows the two moments of the beginning of oil jet penetration and the impingement instant of a test performed at 4920 RPM and an oil pressure of $10.5 \cdot 10^4 Pa$. The effect of windage is visible in the jet bending towards the direction of rotation as well as its break up after the impact. The effect of gear rotation with similar oil jet injection velocities are reported in Figure 2.9, where the total penetration of the oil particles is visible for the two tests. Comparing the two pictures it is possible to observe the higher windage effect when higher rotating velocity is present, consequently the oil jet is heavily bended. Also a different break-up happens, a higher percentage of smaller particles are carried out of the teeth spacing having a detrimental effect on lubrication and, mostly, on cooling.
Akin et al. [10], in the same work, provided an analytical model able to predict the impingement and penetration depths depending on oil pressure and taking into account also the effect of windage. They compared the predictions with the experimental results finding good agreement.
Further work was done, on the cooling efficiency of oil jets, by Dewinter and Blok [33]. They indicated that the oil that reaches the tooth surface is split in two parts, one stream moves radially outward the other inward eventually reaching the tooth root or even the other tooth surface.
Later El-Bayoumy et al. [11] provided a balance of all the forces acting on the oil after the impingement taking into account also the Coriolis effects, a sketch is reported in Figure 2.10. Their work was focused on the heat transfer and they provided a steady state temperature prediction all over the tooth. However none of the cited works dealt with power losses due to oil injection.
In 2008 Johnson et al. [34] performed an experimental investigation on a spiral bevel high-speed gear in shrouded configuration, aimed at evaluating the torque losses due to lubricant oil injection. They found a strong torque increase with oil mass flow rate and proposed a very simple predictive model.
The test rig allowed visualizations through a transparent shroud, so they

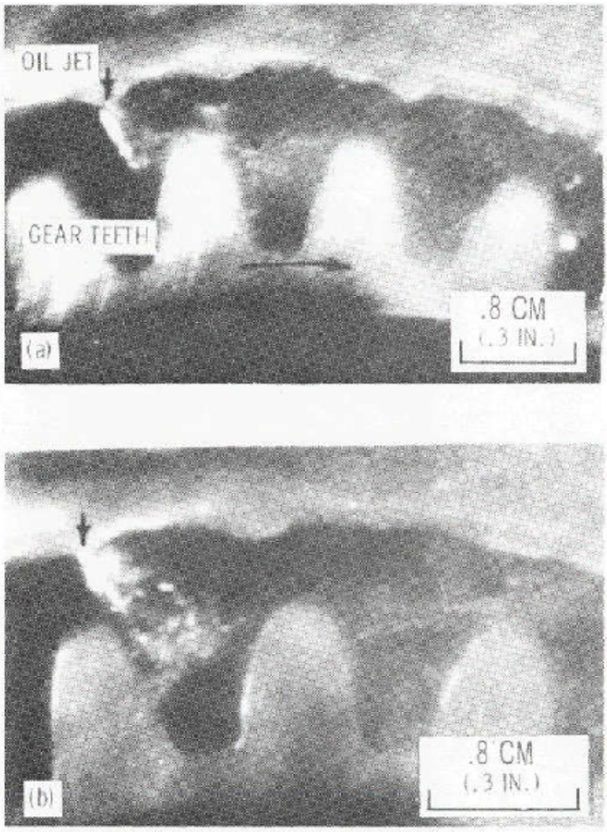

Figure 2.8: Oil jet penetrating tooth space and impinging tooth; speed, 4920 rpm; oil pressure, $10.5 \cdot 10^4 Pa$ *[10]*

could observe that the air and oil phases remain separate, indicating that it is not physical to use an average fluid density to model the phenomenon. This study identified three main loss terms that in sum represents the resistant torque in shrouded gears: single air windage, oil acceleration and oil recirculation.

Considering the multiphase condition of the phenomenon, CFD simula-

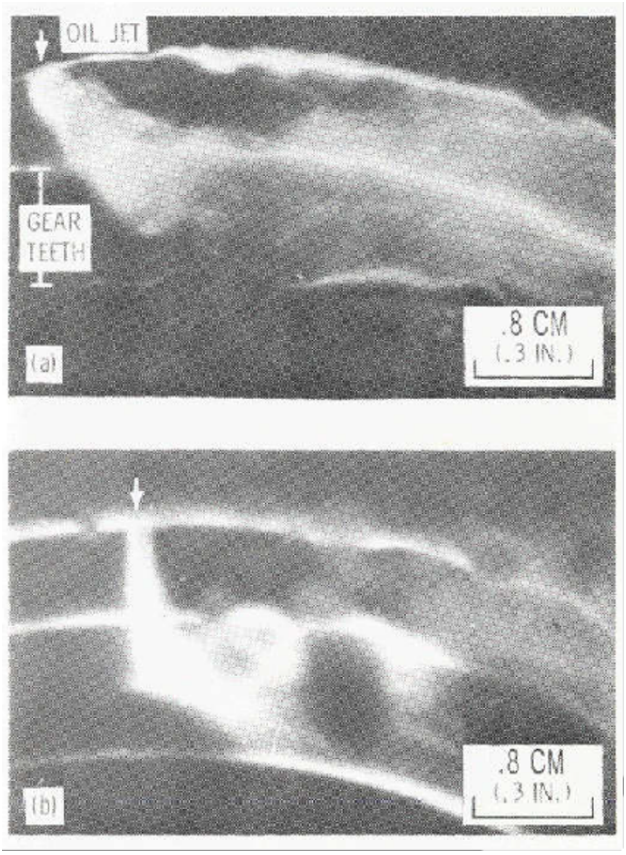

Figure 2.9: Oil jet impingement and subsequent penetration into the tooth space; (a) 4920 rpm and oil pressure of $14 \cdot 10^4 Pa$*; (b) 2560 rpm and oil pressure of* $13 \cdot 10^4 Pa$ *[10]*

tions could help to deepen the knowledge on the interaction between oil jet and gears. However the need for transient and multiphase models contemporary involved in the simulation of such a system, make them very challenging to be performed. For this reason only recently, contributions on this branch have been provided by Li et al. [35], they studied a gear

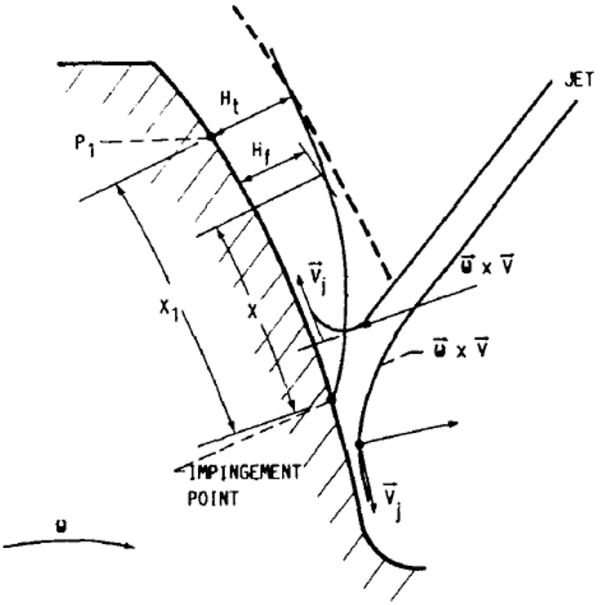

Figure 2.10: Centrifugal and Coriolis accelerations above and below impingement on gear tooth [11]

pair subjected to splash lubrication, and Arisawa et al. [36] which investigated both experimentally and numerically the windage and oil churning losses within a prototype bevel gearbox. Both the applied Volume Of Fluid (VOF) method to model the two-phase flow.

A pioneer work on the jet lubrication method was performed at the Department of Industrial Engineering at the University of Florence by Fondelli et al. [37, 38] where the VOF technique was used to model a lubricant oil jet impacting on a shrouded spur gear. The effects of subatmospheric ambient pressure was investigated as well as different injection angles.

Besides the impingement and penetrations depths they observed the jet lateral spreading on the tooth surface. The resistant torque was also calculated and the model proposed by Johnson et al. [34] verified and

updated with the effect of jet inclination.

2.3 Gear meshing losses

During meshing phase the teeth of the two gears enclose small volumes of air which is compressed and then expanded. This work is extracted from the gears and results in an increase of power losses.
Few studies can be found in literature concerning this phenomenon. The first study is from Rosen [39] which, in 1961, determined the air velocity in spur gears using an incompressible flow theory, this work proved that sonic conditions can be reached. Wittbrodt and Pechersky [40] studied the fluid pumping resulting from meshing conducting two different analysis considering the fluid incompressible, such as when oil is present, or compressible, for example when there is low lubricant and a portion of fluid is air. They found that for both the cases very high flow velocities are reached considering the short time in which the volumes change. When the flow is compressible a sonic wave can form, which may be responsible for noise generation.
An important result concerns the high pressure and temperature reached in the meshing area, all this energy generated is yielded for a certain part in the air-oil mixture, the rest to the gear teeth causing temperature increase.
Houjoh et al. investigated velocity and pressure fields within a tooth space for meshing spur [41] and helical gears [42], by acquiring transient pressure signal using a pressure transducer placed at the bottom of the tooth cavity.
Diab et al. in 2005 [43] used these results to developed a hydrodynamic model able to predict the compression-expansion process by the meshing teeth.
The gear meshing losses has been studied also from a numerical point of view, Gorla et al. [44] provided a numerical and experimental investigation on the effect of rotational speed on fluid dynamic losses of a completely

oil filled gearbox.
These experimental results have been exploited by Burberi et al. [45] for validating a transient RANS simulation model performed at the Department of Industrial Engineering of the University of Florence (DIEF), they provided useful information on the power losses mechanism as well as on the flow and pressure fields generated by the gear's pair.
On this kind of losses there is still room for research, for example dealing with the effect of pressure on meshing losses. For this reason the test rig exploited for the present work can be operated also in gear's pair configuration allowing, in the next future, torque measurements in different rotating speed and pressure conditions.

Chapter 3

Experimental Setup

A novel rotating test rig was exploited to collect data on the fluid-dynamic losses within a high speed power gearbox for aircraft applications. The experimental survey was performed at the Technology for High Temperature (THT) Laboratory of the Department of Industrial Engineering of the University of Florence.
As showed in Figure 3.1, the test rig is enclosed in a soundproof cabin equipped with a ventilation system for air recirculation. For safety reasons, all the electrical panels and control pulpits are placed outside together with computers allowing the operators to set working conditions and to perform data acquisition and processing in a remote way.
Looking within the test room, see Figure 3.2, three main components are present:

- Test rig
- Bearings lubricating oil control unit
- Oil jet control unit

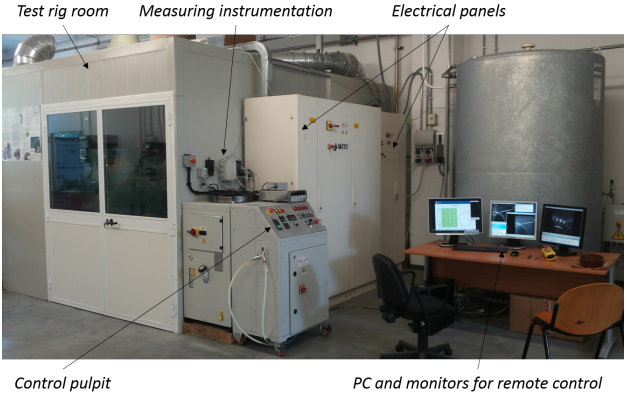

Figure 3.1: View of the laboratory

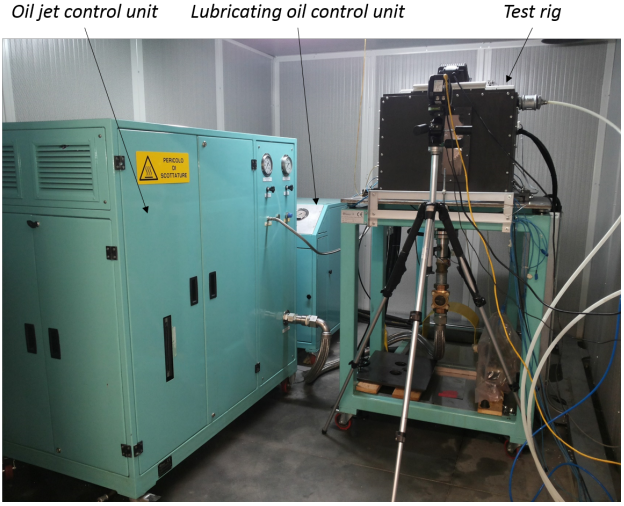

Figure 3.2: View of the test cabin

3.1 Test Rig

The test rig is able to reproduce actual working conditions of a power gearbox in terms of rotating velocity, ambient pressure and oil jet lubrication velocity.
Referring to Figure 3.3, the rig is composed by a rotating shaft supported by two ball-bearings mounted in "O" configuration. The bearings are housed in a sealed casing with inlets and outlets for lubricant and measuring sensor connections. A test chamber encloses the spur gear, it is composed by removable plates in order to allow the gear assembly on the shaft. Even if the enclosure volume is big enough to minimize the effects of the walls, the gear can also be tested in a real open environment by disassembling the chamber's plates in order to verify the effect of the enclosure on the windage losses.
The test chamber is sealed in order to provide a pressure controlled environment: a vacuum pump is indeed connected through a system of tubes and gate valves which allows a fine pressure regulation, till a minimum pressure of 10 kPa, reproducing flight conditions. Two PolyTetraFluoroEthylene (PTFE) seals prevent the lubricating oil from leaking outside the bearing housing or into the test chamber. Three glass windows allow optical accesses for PIV measurements or high speed visualizations.
The elements composing the rotating frame such as bearings' chamber, shaft and spur gear, are machined in 40NiCrMo. A proper fixing system allows the gear to be mounted or unmounted from the shaft.
The test rig is designed to characterize fluid-dynamic losses that are load-independent and very low to be measured, for this reason the gear is unloaded.
A bearing-less torque-meter allows the connection of the shaft with an electric spindle which can reach a maximum velocity of 15000 RPM and a maximum torque of 30Nm.

The whole rotating frame is placed over a plate which is decoupled by the base by means of elastic joints. The assembling of electric spindle, torque-meter and the shaft over the plate is allowed with a tolerance of

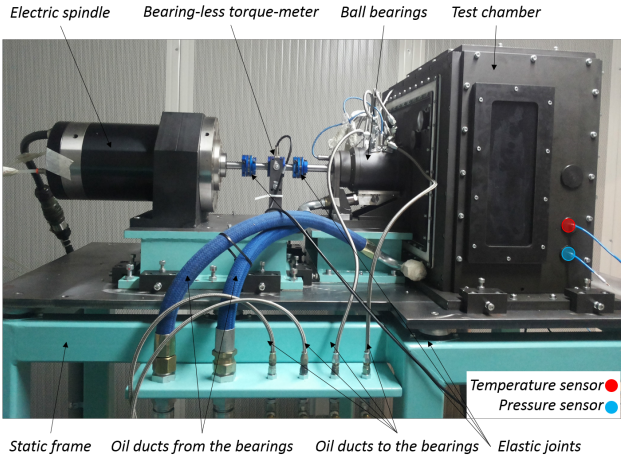

Figure 3.3: View of the test rig

$\pm 0.05mm$, every other small misalignment is compensated by the rotating elastic joints of the torque-meter.

In order to reproduce the effect of oil jet lubrication a spray-bar can be

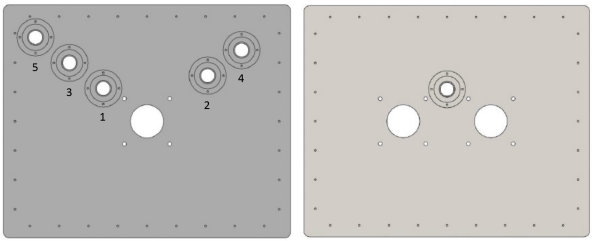

Figure 3.4: Back plate for single gear (left) and meshing gears (right) configurations

inserted within the test chamber by the back plate that can be changed for the single gear or meshing gears configurations. As showed in Figure

3.4 the configuration presenting a single gear allows to vary five spray-bar positions in order to change the jet to gear distance. Considering the rounded shape of the spray-bar it is possible to rotate it obtaining different relative angles.
In order to perform tests using two meshing gears the test rig configuration can be changed adding another rotating axis presenting the driven shaft, the bearings and the gear. Both shafts can be mounted alternatively on the driving line and connected with the torque-meter in order to characterize their friction losses. In this configuration the driven shaft is free to rotate, no load is applied on it.
In the meshing gears configuration there is only a spray-bar position designed to lubricate the meshing zone.
The losses mechanisms present in meshing gears are caused, excluding the windage, by air and oil trapping between the teeth, for this reason tests need to be performed both with and without lubrication. For the first condition a second gear machined in 40NiCrMo can be used, nevertheless in absence of oil lubrication the original gear pair cannot be used, for this reason two other gears were machined in rexilon, a self lubricant material. The gear and spray-bar are sketched in Figure 3.5, their characteristics are given in Table 3.1 together with the jet to gear distances tested for the lubricating conditions and the jet diameter. Dimensions are scaled with respect to the pitch diameter D_p.

L_f/D_p	Z	L_j/D_p	D_j/D_p
0.36	38	0.013,0.5	0.0065

Table 3.1: Gear characteristics

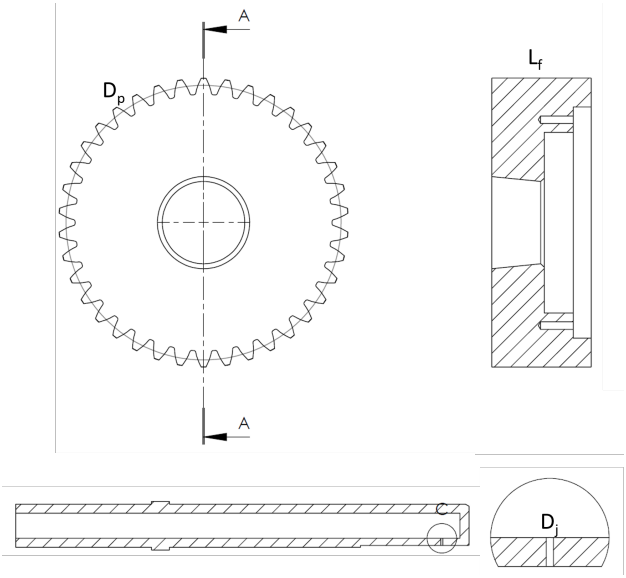

Figure 3.5: Sketch of gear and spraybar

3.2 Lubricating Oil Control Unit

In order to provide the proper cooling and lubrication to each bearing chamber a dedicated oil control unit was employed, a scheme of which is presented in Figure 3.6. Lubricant oil ISO 46 was used.

An electric heater is installed in the oil tank, it allows to heat up the oil, while an air cooler is used to dissipate any overheating that may occur from the bearings working at high speed conditions. The oil mass flow rate, measured by a flow-meter, is fed by a pump and recollected to the tank by gravity, the working pressure was set at 3 bar and controlled by a pressure transducer.

Two K-type thermocouples are placed in the bearing casing in order to trigger warnings if any temperature exceeds safety limitations.

All these instruments are used to set the proper conditions in order to

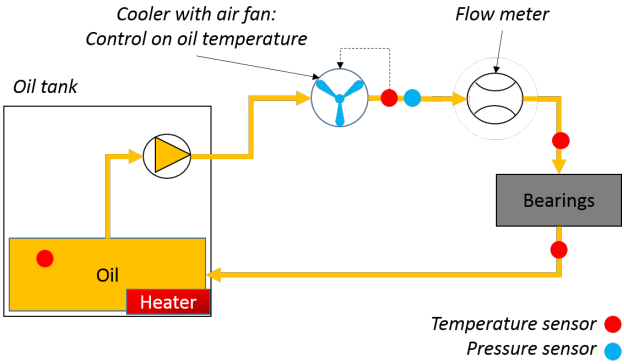

Figure 3.6: Oil control unit scheme for bearings cooling and lubrication

assure the rig to work properly, for this reason they are not acquired during the tests. Nevertheless in order to make predictions on the resistant torque due to the drive train, T-type thermocouples were used to monitor the oil temperature before and after crossing the bearings chamber as it will be better explained in section 3.4.

3.3 Oil Jet Control Unit

A different oil control unit, working with MIL-L-23699 oil, was used in order to provide the oil jet within the test chamber.
Figure 3.7 shows the working scheme of the control unit: a volumetric pump feeds the circuit that is equipped with an overpressure valve, which opens a by-pass to the oil tank if a maximum pressure of 30 bar is reached. The mass flow rate is split in two or more parts in correspondence of a distributor used to set constant upstream conditions for one or more pipes. A part of the oil recirculates continuously, another part can be injected in the test chamber and is recollected and sent to the oil tank by means of a scavenge pump. A glass specola is placed under the test chamber and allows to check if the oil is flowing. Automated valves allow

to perform a fine mass flow regulation. Two electric heaters are placed

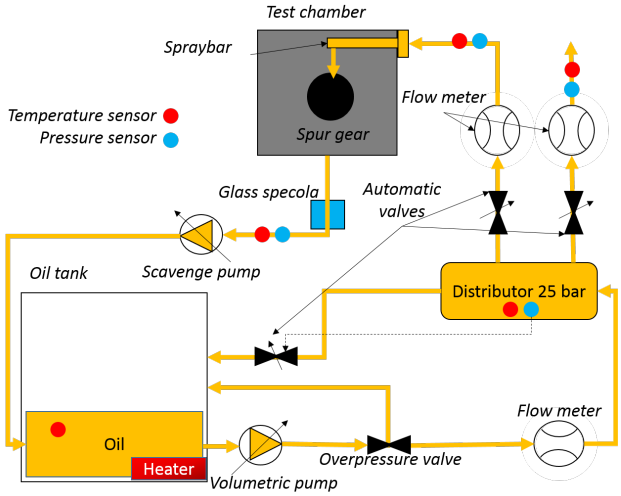

Figure 3.7: Oil control unit scheme for oil jet generation

within the oil tank in order to heat up the oil, a maximum temperature of 180°C can be reached in the test rig.
In order to control and register the working conditions, every branch of the circuit is equipped with pressure and temperature transducers as well as flow-meters. The control unit is operated using a in house LabVIEW®routine installed in a PC that is able to communicate with all the on-board instruments by means of a NI-cDAQ-9188 chassis.

3.4 Measurement Techniques

The tests performed during this experimental investigation can be divided in three main parts according to the investigated physical phenomenon:

- Power losses due to windage and oil jet impact

- Air flow field measurements
- Oil jet visualizations

Sensors and measuring devices used for data acquisition and processing will be presented divided according to their use in the above list.

3.4.1 Power Losses Measurement

Torque losses are affected by several parameters, such as rotating speed, air temperature and pressure and rotating frame friction losses, which in turn depends also on bearings lubricating oil temperature. Therefore every parameter was measured by a dedicated sensor, this task was fulfilled by an acquisition program encoded in LabVIEW®environment.
In the following section the characteristics of every instrument exploited will be shown, together with the post-processing technique aimed at obtaining the windage power losses.

3.4.1.1 Torque

In order to measure power losses due to air windage and oil jet injection a T11 Bearing-less Rotary Torque Transducer was used, see Figure 3.8.
This instrument can reach a maximum rotating velocity of 30000 RPM with a maximum sample rate of 10 kHz, the accuracy is stated by the producer as 0.1 % of the full-scale that is 10 Nm. The device is also equipped with a speedometer: a standard encoder with 6 sensors equally spaced circumferentially.
A careful assembling with shafts and a dedicated support placed on the base of the rig was performed, two dedicated couplings, able to compensate small axial, radial and angular misalignments, were used for the connections with the shafts avoiding any contact between the rotor and stator of the torque-meter. Figure 3.9 shows the transducer in position. Data from the torque-meter and speedometer were acquired using a NI-9184-cDAQ chassis. The device is fed by a dedicated 24 VDC power supply, see Figure 3.10.

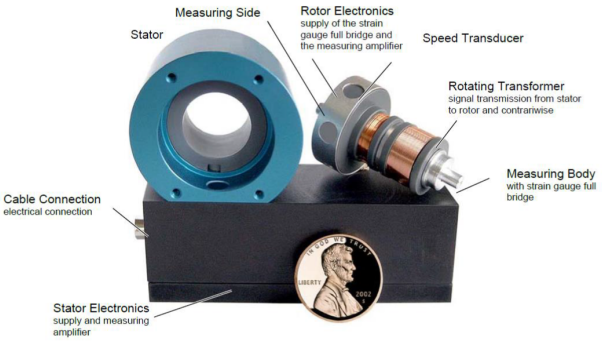

Figure 3.8: T11 Bearingless Rotary Torque Transducer

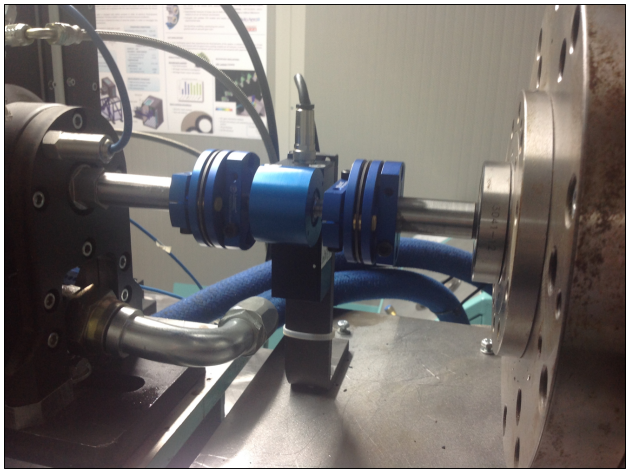

Figure 3.9: The T11 Transducer installed on the drive train

3.4.1.2 Temperature and Pressure Sensors

T-type thermocouples are placed in different points of the rig such as at the inlet and outlet of the bearing chamber lubrication system, inside the test box and in the outer environment. The accuracy of these sensors

is of ± 0.5 ℃.
A pressure tap is located within the test chamber and is connected to a Honeywell Sensotec absolute pressure transducer with an accuracy of the 0.1% of the full scale, that is 15 psi.

Both temperature and pressure sensors are connected to an Agilent

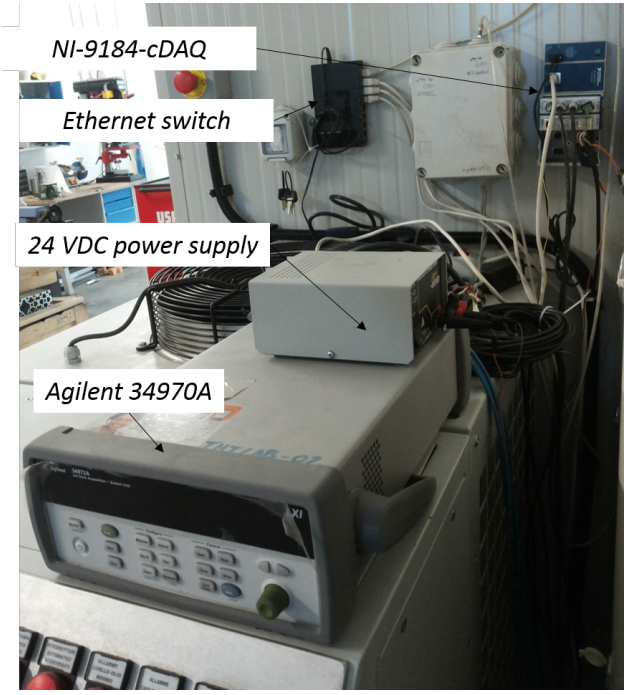

Figure 3.10: Devices power supply and acquisition units

34970A data acquisition/switch unit. Figure 3.10 shows all the instruments power supplies and acquisition units together with an ethernet switch that allows the data flow to the PC.

3.4.1.3 Drive Train Friction Losses Characterization

The torque-meter is sensible to every torsional force acting on the driven shaft, as Figure 3.3 shows, the bearing chamber must have an effect on the readings of the device. The torque measured results by the sum of the frictional forces acting on the bearings and the windage losses due to the gear rotation, only this last contribution is the real goal of the measurement.
Given this premise, a series of preliminary tests were performed in order to evaluate which parameter affect the frictional losses of the driven shaft: the gear was unmounted and the rig operated varying the lubricant oil temperature, the shaft velocity (expressed in terms of gear pitch line velocity V_p), the test chamber pressure. Everyone of the aforesaid parameters was found to have an impact as shown in Figures 3.11 and 3.12.
The highest effect on friction losses is due, as expected, by the rotating velocity which is the main responsible for the torque increase. The

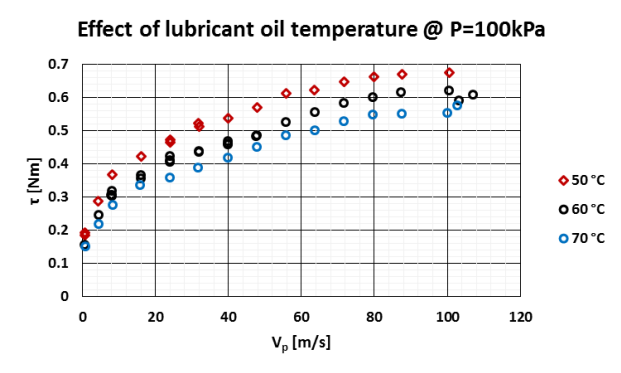

Figure 3.11: Friction losses of the drive train due to lubricant oil temperature, evolution with gear pitch line velocity V_p

augmentation of the oil temperature is beneficial because it brings to a significant torque reduction. On the other hand, considering the heat

exchanged within the bearings chamber, there is the risk of an elevated oil overheating. For this reason a temperature of $60°C$ was preferred as the best compromise.

Pressure within the box has smaller effect: the torque decreases at lower

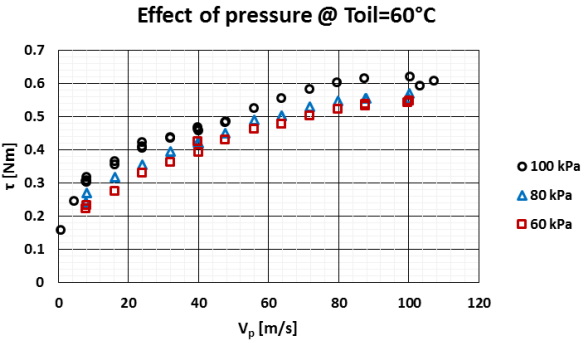

Figure 3.12: Friction losses of the drive train due to lubricant test chamber pressure, evolution with gear pitch line velocity V_p

pressures given the reduced windage losses of the portion of the shaft cantilevered within the test chamber.

From the collected database a multiple variable fitting was performed and an empirical formulation for friction torque was calculated obtaining the following formulation:

$$\tau_{corr} = a \cdot V_p^b \cdot T^c \cdot \rho^d \tag{3.1}$$

Where τ_{corr} is the torque calculated following the correlative method (eq. 3.1), V_p is the rotating speed expressed as the gear pitch velocity, T is the oil inlet temperature, ρ is the air density within the box. a,b,c and d are coefficients obtained by performing the multivariate fitting of the experimental data. They are not given because every time the shaft is unmounted and/or changed they need to be recalculated. However an example of the reliability of the friction torque prediction is given by the

graph in Figure 3.13 where the predicted values are plotted against the experimental ones resulting very close to a straight line with slope one. This value was then used to purge the shaft friction torque value (τ_{corr}),

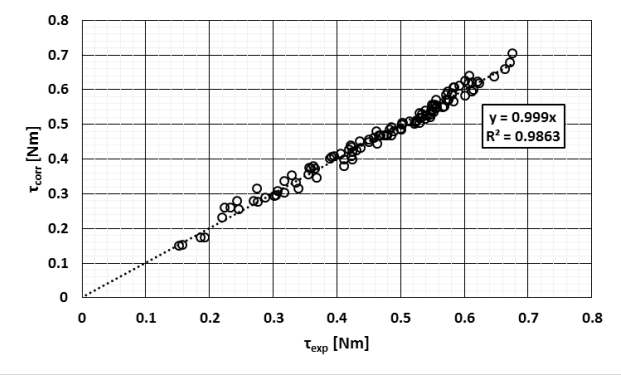

Figure 3.13: Comparison between experimental and calculated friction losses

calculated, from the overall one ($\tau_{overall}$) , measured by the torque-meter, in order to insulate the windage effect ($\tau_{windage}$):

$$\tau_{windage} = \tau_{overall} - \tau_{corr} \tag{3.2}$$

3.4.2 PIV Measurement and Oil-Jet Visualization

As mentioned in the section 3.1, the test chamber is equipped with three optical accesses in order to characterize the flow field around the gear by means of the Particle Image Velocimetry (PIV) technique and to provide information on the oil jet lubrication system in terms of break-up, interaction with the air flow and capacity of penetration within the teeth spacing.

3.4.2.1 Fundamentals of PIV

The main features of PIV will be here briefly described referring the reader to the work of Raffel et at. [46] for a more detailed description of the technique.
The PIV allows to measure the instantaneous whole field velocities by using the simple speed definition as: $speed = \frac{distance}{time}$. Particles, named seeding, are added to the flow and their positions recorded in two different instants, in such a way their displacement is actually measured during a known period of time. Of course this means the seeding velocities are associated with flow ones, for this reason proper particles dimensions must be set in order to minimize the discrepancies between the measured and actual velocities.
Figure 3.14 shows how practically this technique works: the examined area is illuminated by a pulsating light sheet generated by a laser and a system of optical components. The time between the two lasers pulses is the denominator of the equation above.
A CCD-Camera (CCD = Coupled Charge Device) is positioned orthogonally with respect to the investigated area and acquires the light scattered by the seeding, the particles result in light spots on a dark background. The camera acquisition is synchronized with the laser pulses, so every couple of images obtained contains the information on the particles' positions at two different times. The images from camera are then divided in rectangular regions called interrogation areas or interrogation regions and used to produce most probable particle displacement vector by performing a cross-correlation between the areas from the first and the second frame. Repeating this operation for all the interrogation areas and dividing the displacements for the time between the two acquisitions, produces a vector map of raw velocity vectors. In order to perform the above mentioned operation it is necessary to know which is the real distance in mm reported in pixels; this can be done by performing an image calibration using for example graph paper.
Considering that the PIV is an instantaneous measurement technique, the presence of no meaningful input in some regions can take place. For

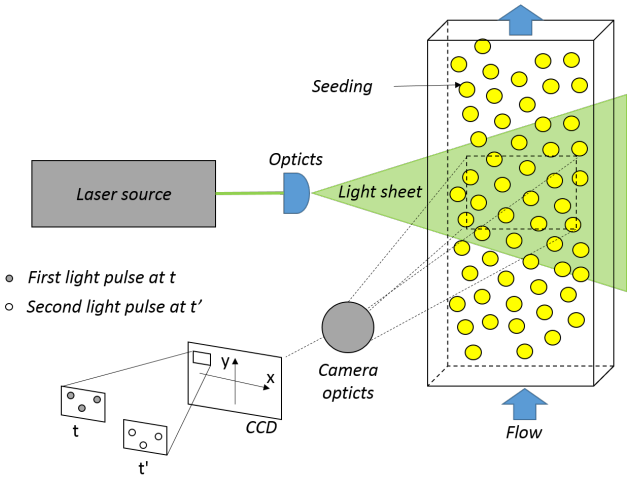

Figure 3.14: Basic principles of PIV

this reason dedicated algorithms are used to subsequently validate the obtained vector maps detecting and removing erroneous vectors called outliers.
In case of gearbox testing, the PIV technique results to be useful to understand the windage losses mechanism by studying the gear interaction with the surrounding air, being a non-intrusive technique it allows to measure air velocity flow field without employing probes as pressure tubes or hot wire that could not be applied given the presence of rotating elements. Moreover measuring the instantaneous velocity in large areas allows to detect spatial structures even in unsteady flow fields.

3.4.2.2 PIV Setup

As mentioned in the previous section the basic components necessary for PIV measurements are a laser source, a CCD-camera and a system providing the proper seeding. The devices used during the experimental

investigation are reported in Figure 3.15.

A diode-pumped, dual-cavity, Nd:YLF Litron LDY300 laser was used as

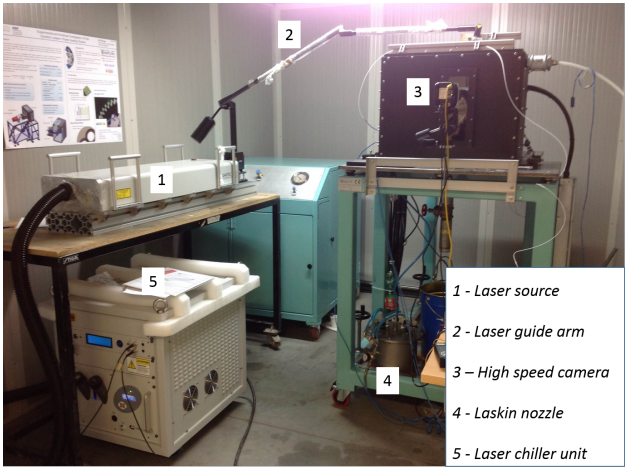

Figure 3.15: PIV measurement equipment and setup

laser source: two independent resonance chambers with two separate Q-switches allow to fire at time intervals as low as 4 μs. A chiller unit allows to maintain a constant temperature within the cavities. Laser power can be regulated but it presents a strong reduction for high frequencies. For this reason measurements were carried out at the maximum power in order to obtain the highest light intensity. A maximum frequency of 20 kHz can be reached.

Considering the high dimensions of the laser source and its distance from the optical accesses, an orientable guide arm ending with lens capable of converting the beam into a 1-mm-thin laser sheet was employed. A support holding the optic was bolted on the test chamber. The correct alignment between the laser source and the optics was guaranteed by a rigid connection on an aluminium section.

The seeding used to track air within the test chamber was injected by a hole in the back plate, Laskin nozzle was used to generate a mist of olive

oil particles with a mean diameter of $1\mu m$.

A Phantom Miro M340 high-speed camera was used for acquiring images

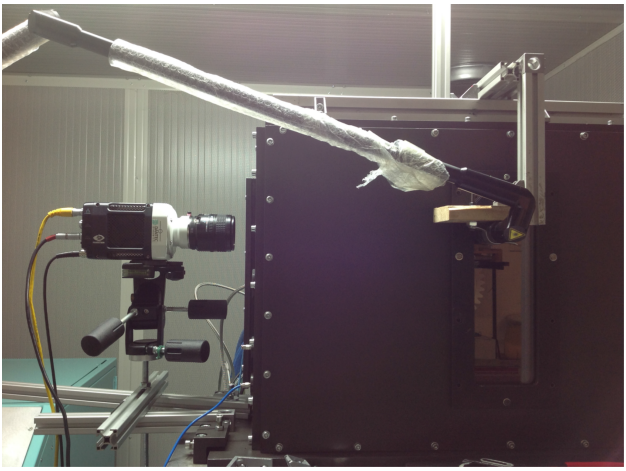

Figure 3.16: Example of camera and optic configuration

of the flow field. The camera acquisition rate depends on the sensor resolution: with the maximum of 2560x1600 pixels, it can acquire not more than 800 fps (frames per second). The acquisition rate can rise up to 66600 fps for a 128x128 pixels sensor area. An example of the camera and optic placement in one of the configurations studied is given in Figure 3.16.

Data acquisition and post-processing were carried out with the Dantec ®DynamicStudio software, which was also responsible for laser and camera synchronization. Each set of image pairs were post processed using a standard average cross correlation approach with a moving average and peak validation approach. The resulting velocity vectors for each camera framing were composed in a single vector map using MatLab.

The optical accesses allow to change the position of camera and optics in order to perform PIV measurements in different planes, see Figure 3.17.

Tests were performed at ambient conditions in order to allow the seeding

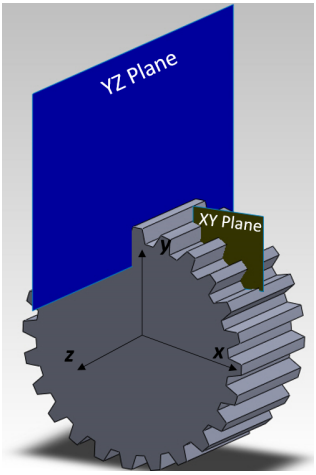

Figure 3.17: PIV investigated planes

injection within the test chamber and at four pitch velocities: 25, 50, 75, 100 m/s.

3.4.2.3 Oil Jet Visualization Setup

In order to perform oil jet visualizations, the same camera used in PIV measurement was employed, the illumination was provided in a diffusive way using an halogen lamp. A 2D sheet is not sufficient to provide the right amount of information on the oil jet impingement on the teeth or its spreading after the impact. Moreover the camera was not positioned orthogonally with respect to the jet plane because the visualization was focused on looking within the teeth spacing. Therefore the laser was not exploited.
An example of the instrumentation setup for high speed visualizations is showed in Figure 3.18. Depending on the rotating velocity imposed during the visualization, the acquisition frequency was chosen in order to obtain at least three images during a tooth passage. Further information on the chosen frame rates will be given in the dedicated chapter.

Figure 3.18: High speed visualization setup

The objective of these acquisitions was the understanding of jet interaction with the air flow and with the tooth, during the impact.

3.4.3 Uncertainty analysis

For every measuring device used and described in the preceding sections the accuracy was provided, nevertheless a deep uncertainty analysis was performed on those parameters obtained using measurement techniques for which a complex post-processing was necessary.
The objective of the work is to measure the windage torque calculated from equation 3.2, for this reason the uncertainty analysis needs to be performed taking into account the accuracy of the parameters used to calculate τ_{corr}. In order to do this, uncertainty analysis was performed following the standard ANSI/ASME PTC 19.1 [47] based on the Kline

and McClintock method [48].
The quantities considered for the analysis were basically the uncertainty on the correlation, due to errors on density, rotating velocity and oil temperature, summed to the original torque-meter accuracy.
The torque error was calculated to be almost constant, for this reason the per cent uncertainty is a function of the net torque. As Figure 3.19 shows, there is a decreasing trend both with pitch velocity and density, the two main parameters responsible for windage losses.
Tests at $\rho > 0.7 \frac{kg}{m^3}$ show to have an uncertainty lower than 10 % for

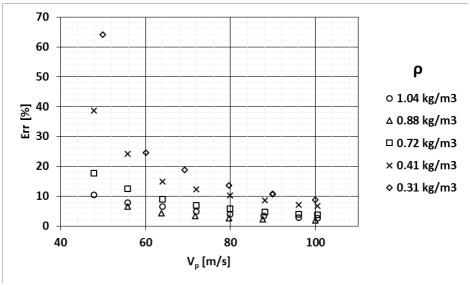

Figure 3.19: Uncertainty evolution with torque

almost the totality of test points.
For lower densities the losses are very low and the per cent error drop under 10 % only for the highest pitch velocities, greater than 80 m/s.
The other measurement technique used in this experimental investigation is the Particle Image Velocimetry (PIV) for which, as suggested by Gancedo et al. in [49], it is still easy to use the Kline and Mc Klintock [48] method, after simplifying the formula for velocity evaluation as:

$$V = M \cdot \frac{\Delta D_p}{\Delta t} \tag{3.3}$$

Where M is the magnitude factor expressed in m/pixels, ΔD_p is the particle displacement in pixel and the Δt is the time between the two acquired frames. According to the study of Westerweel [50] the uncertainty

on the particle displacement is expected to be in the range of 0.1 pixels. The uncertainty of the planar velocity can be so expressed as:

$$\frac{\delta(V)}{V} = \pm\sqrt{\left(\frac{\delta(M)}{M}\right)^2 + \left(\frac{\delta(\Delta D_p)}{\Delta D_p}\right)^2 + \left(\frac{\delta(\Delta t)}{\Delta t}\right)^2} \tag{3.4}$$

After a proper image calibration the M value is fixed for a certain setup and so the ratio $\left(\frac{\delta(M)}{M}\right)^2$ can be neglected. The time uncertainty of laser pulse is very low, in the order of 1 ns.
The equation 3.4 can so be simplified in:

$$\delta(V) \approx V \cdot \frac{\delta(\Delta D_p)}{\Delta D_p} = \frac{M\Delta D_p}{\Delta t} \cdot \frac{\delta(\Delta D_p)}{\Delta D_p} = M \cdot \frac{\delta(\Delta D_p)}{\Delta t} \tag{3.5}$$

Following this method a maximum uncertainty of 0.6 m/s was found for tests in plane XY and 0.4 m/s for tests in plane YZ.

Chapter 4

Windage losses

In this chapter a deep analysis of windage losses due to a single spur gear rotating in air at variable pressure conditions will be provided. In order to have a better understanding of every physical phenomenon occurring in this tests, a numerical investigation was also carried out in parallel with experiments.
Experimental and numerical results obtained will be presented divided in two main parts considering the two main measurement techniques adopted: firstly the power losses will be observed and compared with results already available in literature, then a deep analysis of the flow field will follow.

4.1 CFD Analysis

4.1.1 Computational Domain and Boundary Conditions

The test chamber has been accurately reproduced by the computational domain, a sketch of which is showed in Figure 4.1. It is divided into two main parts: a rotating domain, comprising the gear and a portion of fluid surrounding it, and a stationary one useful to model the flow far from the gear. The flow field close to the gear, within the rotating domain, has been indeed solved using the rotating reference frame equations, on the

contrary stationary frame equations have been used outside the rotating zone.
The rotor-stator interface has been treated using the frozen rotor model, no-slip condition has been applied to all the walls in turn divided between stationary, such as the box wall and rotating, for gear and shaft surfaces.

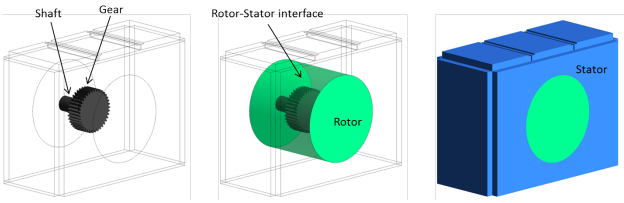

Figure 4.1: Computational domain

4.1.2 Numerical Setup and Grids

ANSYS Fluent v.16 has been used for solving 3D RANS equations [51]. Due to low Mach conditions and little variations in term of temperature, the fluid has been treated as incompressible and with constant properties. A segregated solver with SIMPLEC scheme was selected as velocity-pressure coupling algorithm. Pressure field was discretized using a second order scheme, while a second order upwind scheme was used for the discretization of the velocity field, as well as for turbulent quantities. Turbulence was modelled adopting standard $k-\epsilon$ in conjunction with scalable wall functions as regards to the near wall treatment. The simulations were stopped when the resistant torque had achieved a steady condition, and the scaled residuals had reached a minimum of $1.0 \cdot 10^{-5}$ for every equation.

ANSYS ICEM-CFD has been adopted to generate three hexahedral meshes, having an increasing number of elements; each grid was converted in a polyhedral mesh by using a conversion tool available on Fluent solver. A mesh sensitivity study was performed, comparing the torque coefficient at a pitch line speed of 100 m/s; the grid dimensions and the results

Mesh ID	Nodes number [−]	Torque coefficient [−]
1	2.6 M	0.332
2	17.6 M	0.346
3	47.6 M	0.345

Table 4.1: Results of mesh sensitivity.

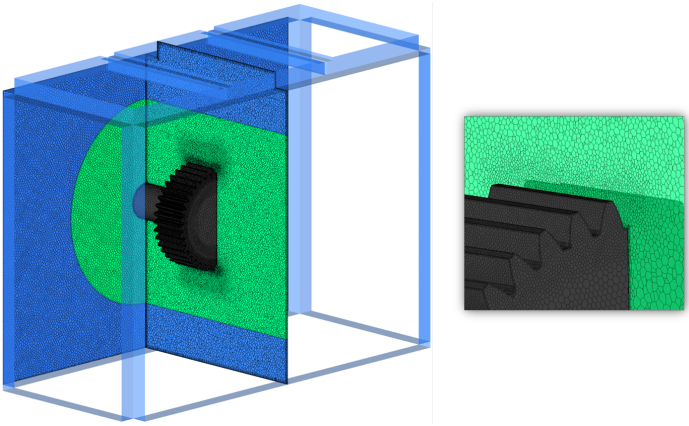

Figure 4.2: Computational grid

are summarized in Table 4.1. By switching from the coarser grid to the medium size grid, C_m increases of 4.1 %, while a further increase of nodes number (Mesh 3) do not lead to noticeable change in moment coefficient. On the basis of the mesh sensitivity analysis, the medium size grid has been selected for the present work. A picture of the mesh is shown in Figure 4.2.

4.2 Air Windage Power Losses

As already mentioned the air windage losses were characterized by measuring the overall torque and then subtracting the drive train friction

losses calculated using the correlation exposed in chapter 3.
The measurement technique was validated by performing a first series of tests at ambient pressure in order to make a comparison with the well known correlation proposed by Diab et al. [7] and here reported in equation 4.1

$$C_m = \alpha Re^{\beta}\left(\frac{b}{R}\right)^{\gamma} Z^{\delta}\left\{\left(\frac{h_1}{R_p}\right)^{\psi} + \left(\frac{h_2}{R_p}\right)^{\psi}\right\} \tag{4.1}$$

α	β	γ	δ	ψ
60	-0.25	0.8	-0.4	0.56

Table 4.2: Coefficients of the Diab's correlation

The correlation results from a database collected by Diab et al. testing a series of four spur gears with different geometrical characteristics, such as the pitch radius R_p, the gear width b and number of teeth Z, the tests were carried out varying the rotating speed at ambient pressure. Equation 4.1 calculates the moment coefficient C_m that is defined as:

$$C_m = \frac{\tau}{0.5\rho\Omega^2 R_p^5} \tag{4.2}$$

The coefficients $\alpha, \beta, \gamma, \delta, \psi$ are constant and their values are summarized in table 4.2. The values in the brace accounts for the presence of a flange or deflector, it has a unit value in free gear case, the definition of h is given as: $h_{1,2} = 0.5R_p^{\frac{1}{\psi}}$ without any obstacle, $h_{1,2} = H_e\sqrt{j_{1,2}^2 + (R_a - R_{d1,2})^2}$ in presence of flange or deflector, where H_e is a step function of unit value equal to $(R_a - R_{d1,2}) > 0$, 0 otherwise. The subscripts 1 and 2 refer to the two sides of the gear.
The effect of the enclosure volume was firstly tested by disassembling the test chamber plates, as Figure 4.3 shows. The two tests showed a very good agreement, as visible in Figure 4.4, where the two power curves plotted together with the values calculated using the Diab's correlation 4.1 in their evolution with the pitch velocity. The graph shows that,

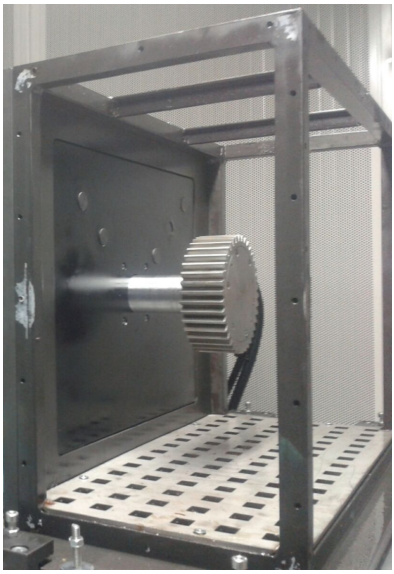

Figure 4.3: Test rig in free gear configuration

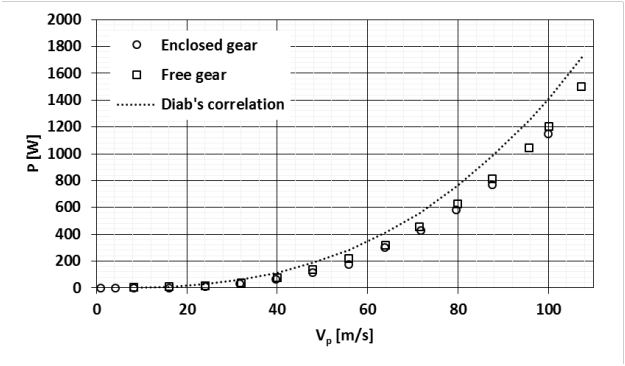

Figure 4.4: Power losses comparison between Diab's correlation and free and enclosed gear configurations

changing the rig configuration, no significant effect on windage power losses is present, nevertheless some differences occur with respect to the Diab's correlation that overestimates the power measured in the experiments. This was explained with the presence of the backplate that is not removable and can affect the flow field around the gear both in open and enclosed configurations giving the same results. Such a component is modelled in the correlation by setting the h parameter: for one side of the gear, equal to 0. This however results in a too strong correction of the original values as showed in Figure 4.5. One reason can be found in the fact that the back plate is quite distant from the gear, not enough to be completely without effects though: we are in a midway between a shrouded and a free gear condition. The relative position between the back plate and the gear is not modifiable for constructive reasons. Further explanation of the back plate effects on the flow field will be given in the next section. The experiments are meant to describe the windage

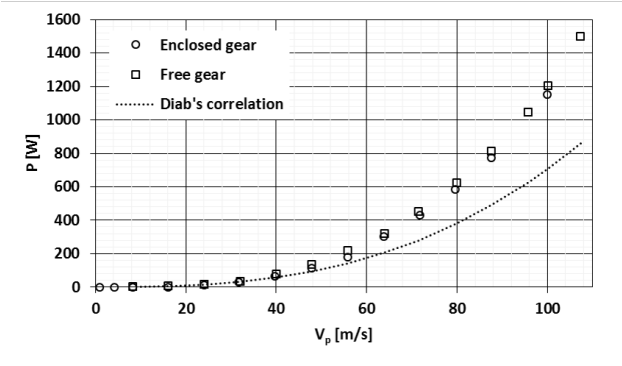

Figure 4.5: Power losses comparison between Diab's correlation and free and enclosed gear configurations imposing $h_1 = 0$

behaviour also in conditions of very low pressure or, better, of very low density. For this reason many tests were performed at different working pressures, results are collected in Figure 4.6 together with the 3^{rd} degree polynomial fitting. As could be expectable, the power losses have a strong

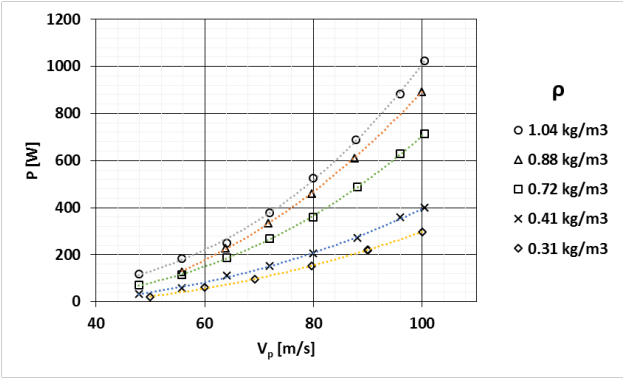

Figure 4.6: Power losses for different working pressures

reduction with air density, this is due to the fact that a minor amount of air is elaborated by the gear. The relation between the windage losses and the air density is linear fixing the rotating velocity, as the Figure 4.7 clearly shows. In this case results are indeed plotted together with their linear fitting. The effects of gear speed and air density on the torque losses

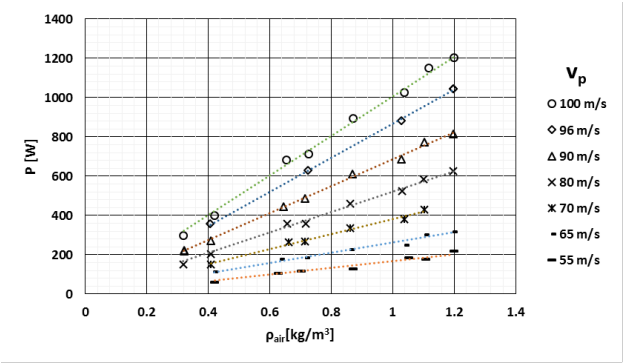

Figure 4.7: Power losses vs air density

were investigated also by performing numerical simulations: the velocity

was varied at ambient conditions while the density was changed for the maximum speed ($V_p = 100m/s$). The graph in Figure 4.8 compare the numerical and experimental results. Differences between the two results are always lower than $\pm 5\%$.

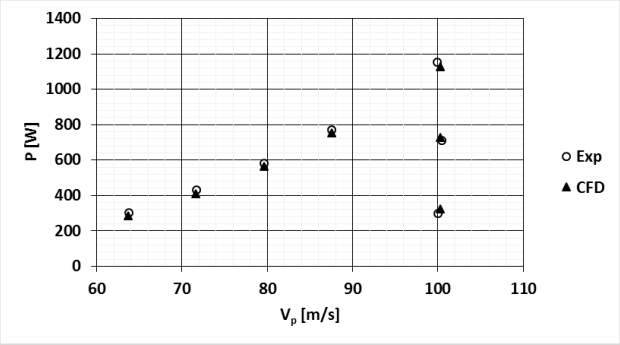

Figure 4.8: Power losses vs pitch velocity: comparison between CFD and experiments

4.2.1 Windage Correlation

One of the main goal of this work was to find a correlation able to well predict power losses for the spur gear, in order to have a safe tool to decouple the windage effects and the oil get torque increase in the second part of the experimental campaign.
All the results can be expressed in terms of dimensionless parameters in order to reduce their dispersion and to find a univocal relationship between power losses, velocity and air density. These parameters are the following:

- Rotational Reynolds number:

$$Re_\phi = \frac{\rho \Omega R_p^2}{\mu} \tag{4.3}$$

- Moment coefficient:

$$C_m = \frac{\tau}{0.5\rho\Omega^2 R_p^5} \tag{4.4}$$

Using these parameters both the effects of rotating velocity and density are considered, the result is showed in Figure 4.9, where all the results already presented in Figure 4.6 are reported. All the test points collapse on a single curve which seems to be a constant for every Re_ϕ. Few words

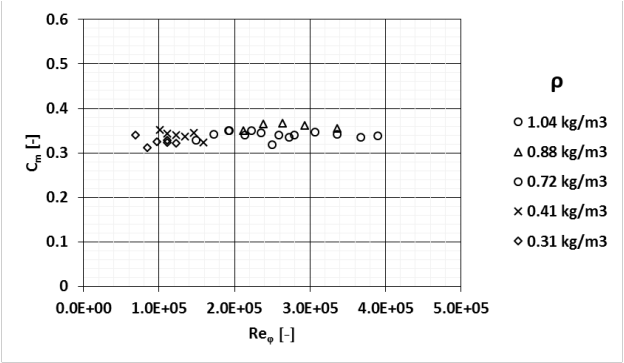

Figure 4.9: Results expressed in dimensionless terms

need to be spent to explain this trend or better its absence: as proposed by Diab et al. [7], the power losses mechanisms can be divided in two main parts, one is due to the viscous effects of air on the gear lateral surfaces, the other can be attributed to the air acceleration given by the teeth spacing to a certain amount of air.
The first contribution is comparable to the windage due to a rotating disk and has been studied by many researchers in the past years. One of the pioneer work on this matter was done by Owen in 1989 [52] which proposed a correlation with the form of a power law with negative exponent:

$$C_m = 0.07288 Re_{\dot{\phi}}^{-\frac{1}{5}} \tag{4.5}$$

For the other contribution Diab proposed a simple fluid-dynamic model based on the momentum increase of a certain air mass due to its acceleration from a null velocity to the teeth peripheral one. He proposed a relation of proportionality:

$$\tau \propto Z\rho x L_f \Omega^2 \left(R_p - \frac{x}{2}\right)^3 \tag{4.6}$$

Where x is a portion of tooth used to calculate the cross section of the mass flow and defined by geometrical parameters as showed in Figure 4.10.

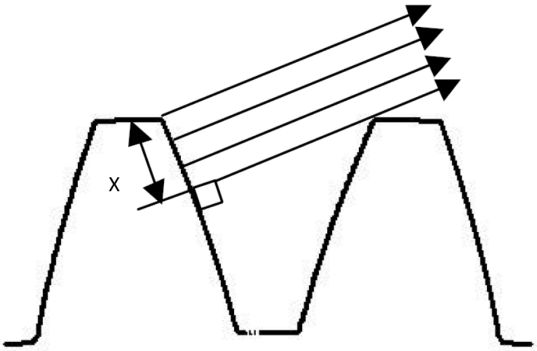

Figure 4.10: Diab's definition of air passage area [7]

Following this relation the rotating velocity affects the torque with a quadratic low while the effect of density is linear. This is in agreement with the results shown in Figures 4.6 and 4.7. Moreover if we apply the definition of moment coefficient to the relation 4.6 we obtain:

$$C_m = \frac{\tau}{0.5\rho\Omega^2 R_p^5} = \frac{Z\rho x L_f \Omega^2 \left(R_p - \frac{x}{2}\right)^3}{0.5\rho\Omega^2 R_p^5} \tag{4.7}$$

Which results in:

$$C_m = \frac{Z L_f \left(R_p - \frac{x}{2}\right)^3}{R_p^5} \tag{4.8}$$

That is constant for a fixed gear geometry. Given all these considerations the constant value resulting from experiments and CFD can be attributed to the fact that the windage due to lateral surfaces is practically negligible with respect to the effect of the teeth on air momentum increase. This is also confirmed by the application of the correlation proposed by Owen for the free disk to the later surfaces of the studied gear: the obtained C_m values are two order of magnitude lower than the measured ones. This comparison is presented in Figure 4.11.

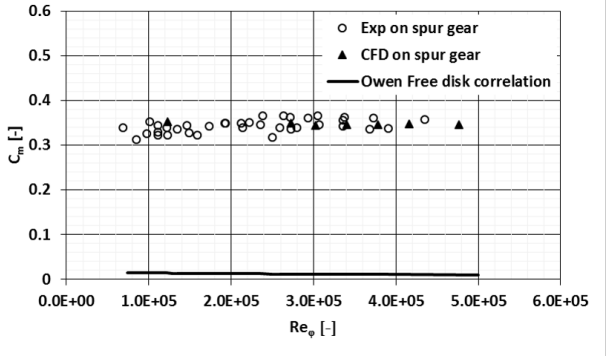

Figure 4.11: Comparison between CFD and experiments and Owen correlation 4.5

Averaging all the results, constant value of $C_m = 0.34$ was then obtained to characterize the windage power losses of the tested gear, with absolute errors contained within the 10 % for all the data (see Figure 4.12).

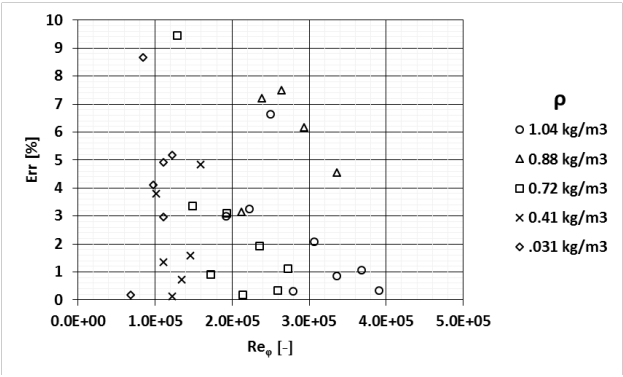

Figure 4.12: C_m correlation's error

4.3 PIV Measurements

Refferring to Figure 3.17 two orthogonal investigation planes were chosen in order to observe the main air flow structures generated by teeth in their movement.

4.3.1 XY Plane

The XY plane is parallel to the faces of the gear and is placed halfway in the face width. Measurements were performed at ambient conditions, two rotating velocities were investigated $V_p = 50$ and $25m/s$. The acquisition was synchronized with the teeth's passage frequency, in order to get 1000 pairs of images that reconstruct "frozen" flow fields within the teeth spacing. The flow fields have been then averaged obtaining a 2D map for every velocity of rotation.
The velocity colormaps, together with the relative streamlines for the two tested conditions and scaled on the respective rotating velocity, are showed in Figure 4.13. From these images it is possible to observe the rotating core generated around the gear which moves at significantly lower velocity. The pumping mechanisms occurring between the teeth can cause an air

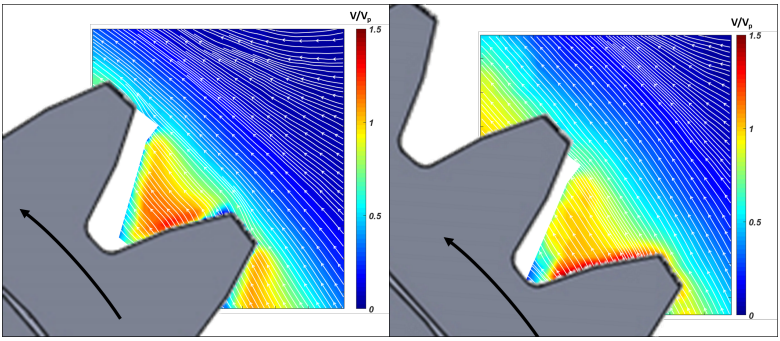

(a) V/V_p and streamlines for $V_p = 25m/s$

(b) Absolute velocity and streamlines for $V_p = 50m/s$

Figure 4.13: V/V_p and streamlines in XY plane

motion from the "pressure" to the "suction" side of the cavity as proposed by Al-Shibl [8], for this reason velocities higher than the entrainment one were registered for both the tests. In order to make more quantitative comparisons between tests, the tangential velocity distributions along the radial direction were calculated at different angular positions following the scheme in Figure 4.14: an angular interval equal to the pitch of the gear, namely 9.4 deg, was investigated, the zero was chosen in the middle of the teeth spacing, positive angles are defined towards the tooth "suction side". Figure 4.15 shows the tangential velocities for test at $V_p = 25m/s$ taken in seven angular positions, on the abscissa the radius is expressed in terms of its ratio with the pitch radius. The first observation is that all the angular positions have a similar trend, particularly at $r/R_p > 1$. At lower radii there are few discrepancies, in this zone the flow field is more complex and changes from a tooth side to the other, because of the air motion. The most interesting thing is that there is a central zone of the tooth (for $r/R_p < 1$) in which the air is flowing from one tooth to the preceding one. The same trend was found for the test at $V_p = 50m/s$ for which the tangential velocity in the mid line is showed in Figure 4.16a together with the one at $V_p = 25m/s$, of course the velocity level is higher.

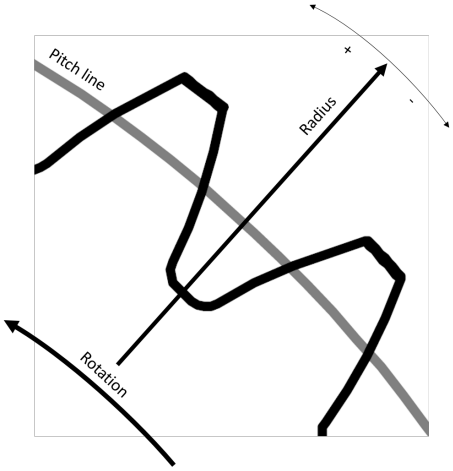

Figure 4.14: Scheme of the angular interval for the tangential velocity extrapolation

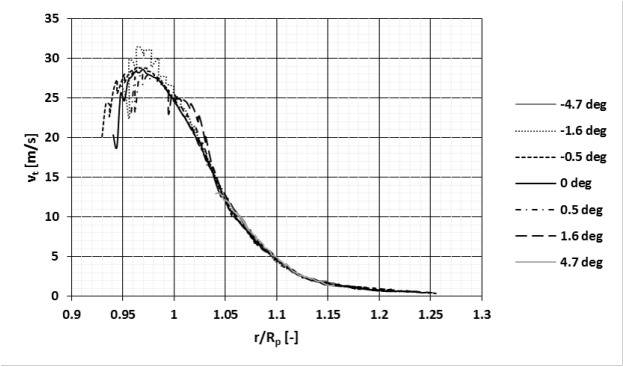

Figure 4.15: Tangential velocities for test at 25 m/s

The two tests can be better compared in terms of Swirl number defined as:

$$Swirl = \frac{v_t}{\omega r} \tag{4.9}$$

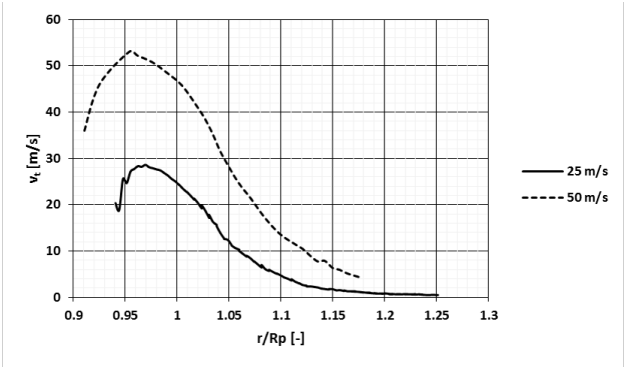

(a) Tangential velocity comparison for $V_p = 25m/s$ at angle zero

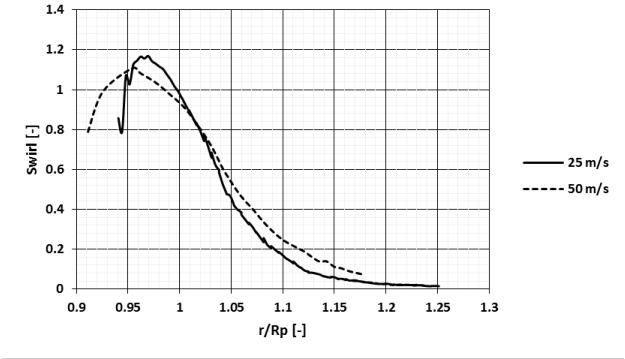

(b) Tangential velocity comparison for $V_p = 50m/s$

Figure 4.16: Swirl comparison at angle zero

In this way the two tests show great similarities, see Figure 4.16b, and the same flow field within and out of the teeth spacing can be expected. The Swirl number within teeth spacing rises up to 1.2 for both the tests. Neither the velocity contours showed in Figures 4.13a and 4.13b nor the velocity distributions are able to clearly highlight any kind of flow field within the teeth spacing.

Test at $V_p = 25m/s$ has been compared also with a CFD simulation

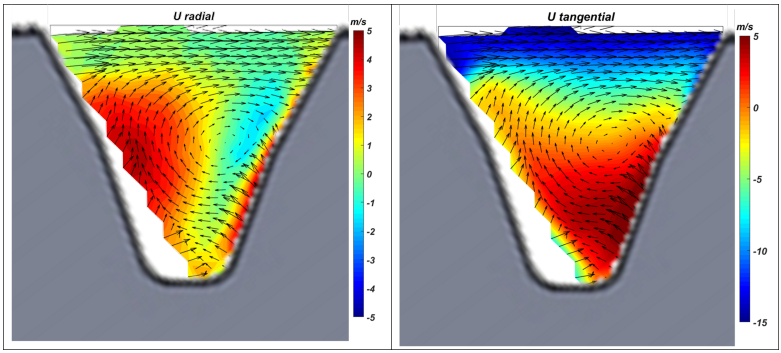

(a) PIV radial velocity and vector maps in gear relative frame for $V_p = 25m/s$

(b) PIV tangential velocity and vector maps in gear relative frame for $V_p = 25m/s$

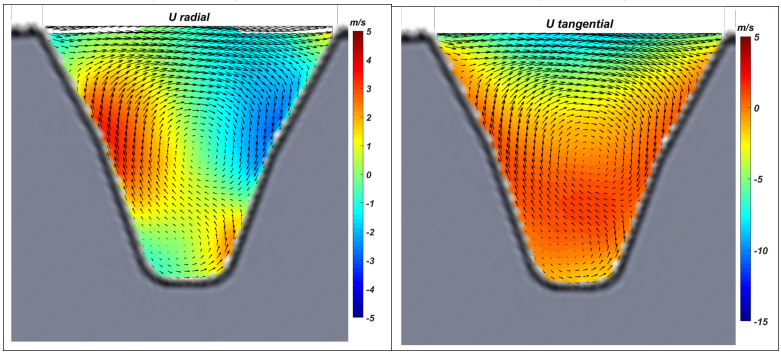

(c) CFD radial velocity and vector maps in gear relative frame for $V_p = 25m/s$

(d) CFD tangential velocity and vector maps in gear relative frame for $V_p = 25m/s$

Figure 4.17: Comparison between PIV and CFD in XY plane

performed at the same conditions, using the model already validated in terms of power losses.

In order to observe the presence of any recirculation phenomenon, PIV and CFD results have been expressed in cylindrical coordinates and the radial and tangential velocities were expressed in the gear reference frame. Results for the radial and tangential velocities in the relative frame are

reported in Figures 4.17a and 4.17b together with the vector maps, the tangential velocity is positive in the gear speed direction, the radial velocity if it is outgoing from the teeth spacing.
First of all it is worth to notice the very good agreement found between experiment and simulation both in terms of flow field and velocities magnitude.
It is then possible to observe the presence of two counter-rotating recirculation as expected: one is at a higher radius and has a clockwise direction, the other rotates in the opposite direction and is placed on the bottom of the teeth spacing. This means that in the meeting point of the two circles air is moving at a higher velocity than the tooth itself, as showed by the velocity radial distributions.

4.3.2 YZ Plane

In this section PIV measurements were performed observing the flow field from a different point of view: as suggested by Dawson [6] and Hill [20], a jet-like structure can be expected on the YZ plane. Four pitch velocities were investigated in this case: $V_p = 25, 50, 75, 100 m/s$.
The time between laser pulses was properly chosen as a compromise between the need of avoiding the seeding particles disappearance from the images due the high cross sectional velocity, orthogonal to the laser sheet, and the capability of seeing their movement on the two acquired frames. 685 pairs of images have been acquired for every test condition. The calculated flow fields has been then time averaged obtaining the results summarized in Figure 4.18, where they are expressed in terms of 2D velocity maps and streamlines. In this case no synchronization was necessary given the absence of any optical obstacle.
In order to more easily describe the maps, a reference system was chosen centered in the middle of the gear width and at the external radius. Distances are expressed as the ratio with the gear width L_f. The expected jet-like structure generated by the gear rotation was actually found but, as supposed in the preceding chapter, the presence of the back plate (left

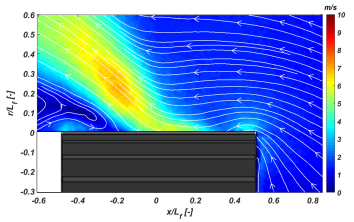

(a) PIV velocity and vector maps in plane YZ for $V_p = 25m/s$

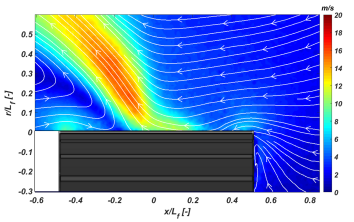

(b) PIV velocity and vector maps in plane YZ for $V_p = 50m/s$

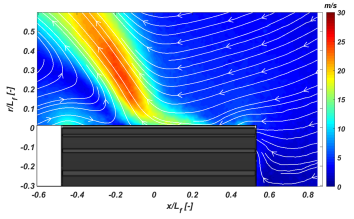

(c) PIV velocity and vector maps in plane YZ for $V_p = 75m/s$

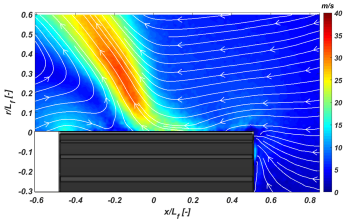

(d) PIV velocity and vector maps in plane YZ for $V_p = 100m/s$

Figure 4.18: PIV velocity and vector maps in plane YZ

in the figures) has an effect on the flow field generated. It seems indeed responsible for the jet inclination. The jet is generated by the center of the gear and immediately moves towards the back plate, the same jet inclination was found for all the tests. A core at higher velocity can be noted as well within the jet. Another important observation can be done by looking at the streamlines close to the gear lateral faces: air is sucked within the teeth spacing from the lateral openings, this confirms the statements proposed by Fondelli [9] in his work based on numerical simulations.

The jet inclination is responsible for a counter-clock wise rotating flow structure close to the back plate.

Maps show a similar flow field for the four tests, nevertheless a more

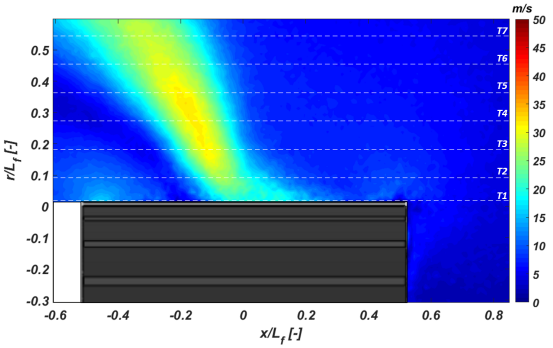

Figure 4.19: Seven traverse position for PIV velocity profiles extraction

accurate comparison can be made by plotting the radial V_r and axial V_x velocity profiles extracted from different radial positions. Seven radii have been chosen: $\frac{r}{L_f} = 0.02, 0.09, 0.18, 0.27, 0.36, 0.45, 0.55$. The positions are showed in Figure 4.19. The velocity components are considered positive when they agree with the geometrical axis.
Graphs summarized in Figures 4.20 and 4.21, show the velocity profiles extracted for the three positions T1, T4, T7. As could be expected the higher is the pitch velocity the higher is the spread between maximum and minimum air speed in both the components investigated.
Observing the axial velocities, Figure 4.21, it is possible to note that at T1, where the jet recalls air from its left, there are positive values that become negative passing through the jet. Moving from T1 to T7 the velocity is only directed toward the left side and very close to zero on the right. The radial velocities are the footprint of the jet, for this reason in T1 there is a peak almost centered on the zero coordinate, but far away from the gear it moves towards the backplate.

The flow fields generated by four tests seem to be very similar. In order to make a better comparison between them, results have been scaled

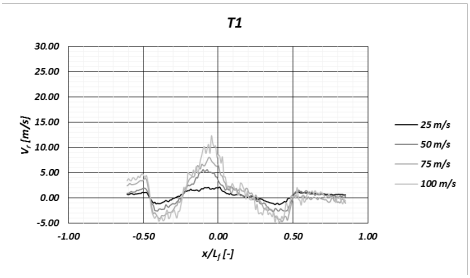

(a) PIV axial velocity profile on T1

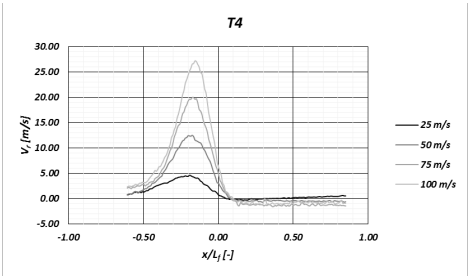

(b) PIV axial velocity profile on T4

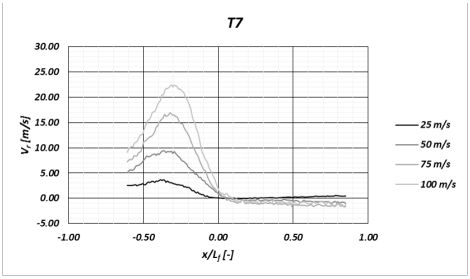

(c) PIV axial velocity profile on T7

Figure 4.20: PIV radial velocity profiles at T1, T4, T7: comparison between all tests

on the pitch velocity V_p. This operation highlights the differences between the tests. As showed in Figures 4.22 and 4.23 all the curves tend to collapse, few differences trigger in the test at $V_p = 25m/s$ at T4, while going at T7 also the test at $V_p = 50m/s$ starts to differ from the others.

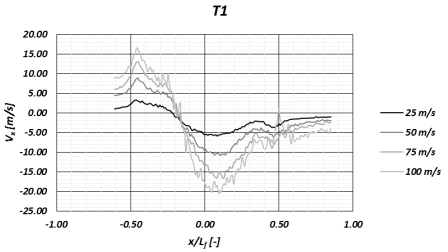

(a) PIV axial velocity profile on T1

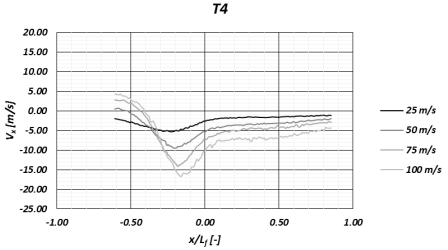

(b) PIV axial velocity profile on T4

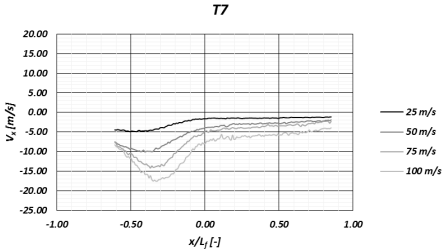

(c) PIV axial velocity profile on T7

Figure 4.21: PIV axial velocity profiles at T1, T4, T7: comparison between all tests

After these comparisons we can state that the flow field generated by the gear is basically the same in the zones close to the gear itself, on the contrary going farther, where the jet starts to decay few differences rise between the tests. The reason may be found in the fact that high rotating

velocities produce greater whirling structures that need more time to be dissipated and extend for a larger space. Further considerations about vorticity and unsteadiness generated by the gear will provided in the following sections.

Comparison of CFD results for test at $V_p = 25m/s$ is reported together with the measured flow field in Figure 4.24a: simulation is able to well predict the jet distorsion towards the back plate.
Observing the pressure field in Figure 4.24b may help to understand the reason of this distorsion: the shaft generates a pressure gradient that recalls air from the backplate side, this amount of air is provided by the gear jet that is for this reason bended in that direction. Two counter rotating vortices are hence generated on that side.
Additional PIV measurements were performed acquiring greater number of pixels per image in order to obtain a wider view of the flow field. They highlighted the increase of the differences between the four tests moving away from the gear, see Figure 4.25. Moreover a great recirculation is visible on the left side which is as higher as the velocity increases.

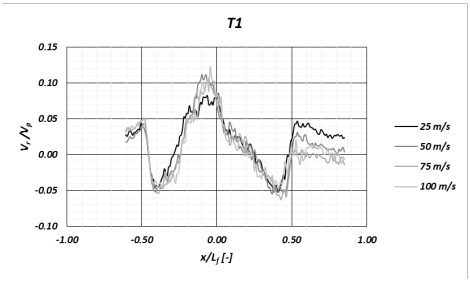

(a) PIV radial velocity profile profiles scaled on pitch velocity on T1

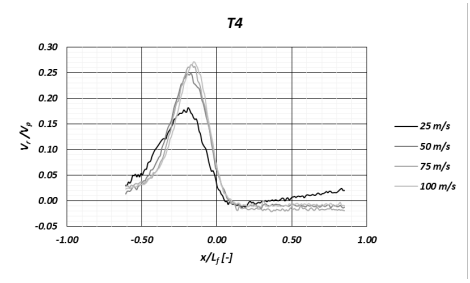

(b) PIV radial velocity profile profiles scaled on pitch velocity on T4

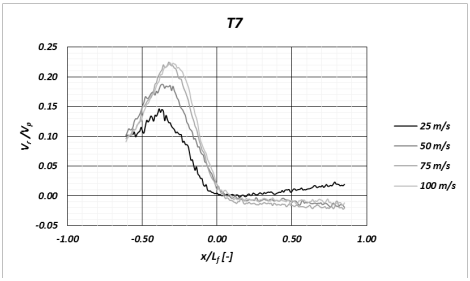

(c) PIV radial velocity profile profiles scaled on pitch velocity on T7

Figure 4.22: PIV radial velocity profiles scaled on pitch velocity at T1, T4, T7: comparison between all tests

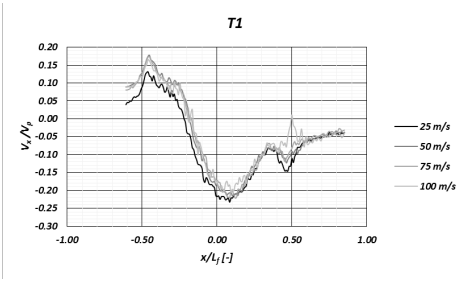

(a) PIV axial velocity profile profiles scaled on pitch velocity on T1

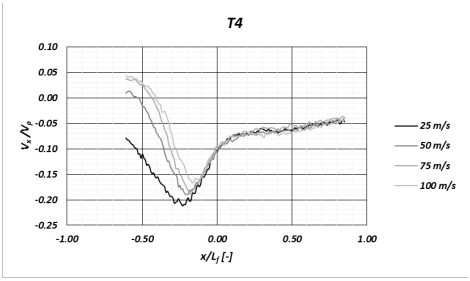

(b) PIV axial velocity profile profiles scaled on pitch velocity on T4

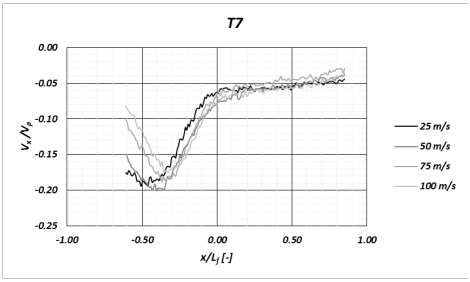

(c) PIV axial velocity profile profiles scaled on pitch velocity on T7

Figure 4.23: PIV axial velocity profiles scaled on pitch velocity at T1, T4, T7: comparison between all tests

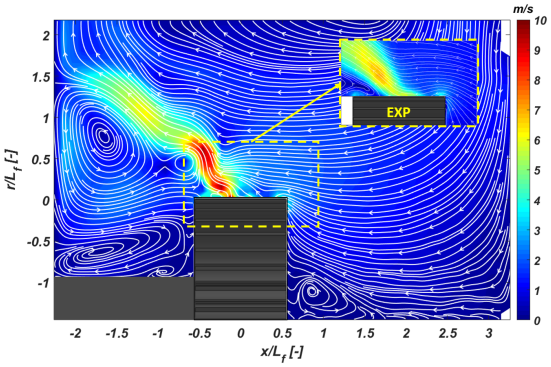

(a) CFD flow field for YZ plane compared with experiment at $V_p = 25m/s$

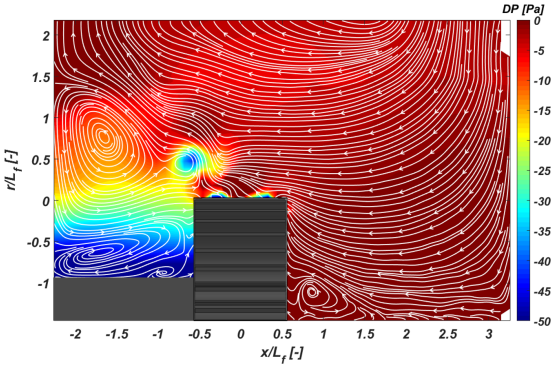

(b) CFD pressure field

Figure 4.24: CFD results for YZ plane

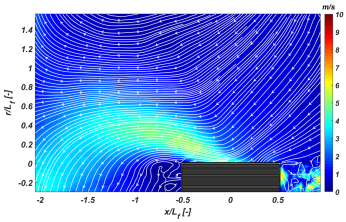

(a) PIV velocity and vector maps in plane YZ for $V_p = 25m/s$

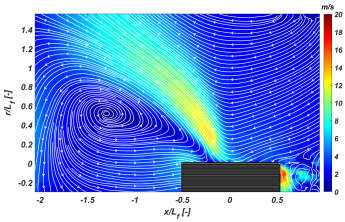

(b) PIV velocity and vector maps in plane YZ for $V_p = 50m/s$

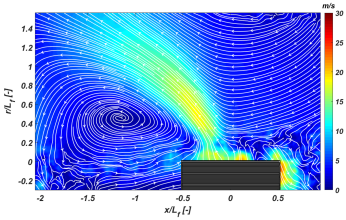

(c) PIV velocity and vector maps in plane YZ for $V_p = 75m/s$

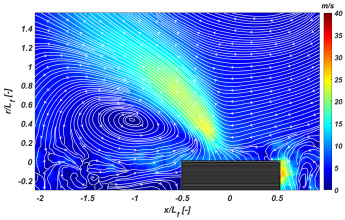

(d) PIV velocity and vector maps in plane YZ for $V_p = 100m/s$

Figure 4.25: PIV velocity and vector maps in plane YZ

4.3.3 Unsteady Phenomena

PIV results showed in the previous section were obtained by averaging a series of instantaneous flow fields calculated from image pairs acquired at high frequency using the high speed camera showed in chapter 3. In this section they will be observed from an unsteady point of view. Additional PIV measurements were performed visualizing a plane close to the gear but moved on the left side in order to observe the unsteady behaviour of the jet.
First, the flow fields evolution with time will be presented, then a spectral analysis will help to understand the principal flow structures representing the jet generated by the gear. Results were also post-processed using the Proper Orthogonal Decomposition (POD) in order to highlight coherent structures .
Tests at $V_p = 25$ and $100 m/s$ were chosen for this analysis considering the differences found between the flow fields in the two conditions; 2245 image pairs were acquired at a frequency of 2233 Hz. In order to reach a so high frequency a reduced number of pixel was acquired, resulting in a smaller area observed.

4.3.3.1 Time-variant flow fields

In order to have an idea of the evolution of the air jet generated by the gear, three instantaneous flow fields measured with a time-step of 1 ms for tests at $V_p = 25$ and $50 m/s$ are showed in Figure 4.27. The first observation is that the flow field is very unsteady and far from the mean value showed in the preceding sections. Also the magnitude of the velocities encounterd is of course higher with the respect to the maps already seen.
Many vortices are generated and evolve within the gap between gear and back plate: two counter rotating structures are visible mostly for the test at $V_p = 25 m/s$ because this jet has a reduced extension and is characterized by lower velocities, bringing to the quicker decay observed

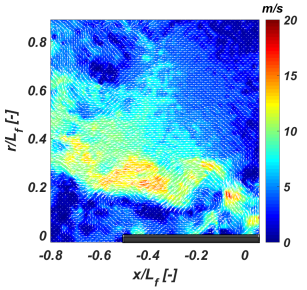

(a) $V_p = 25m/s$ - *Time* $= 0$

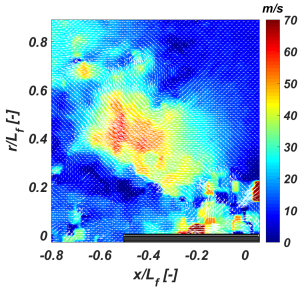

(b) $V_p = 50m/s$ - *Time* $= 0$

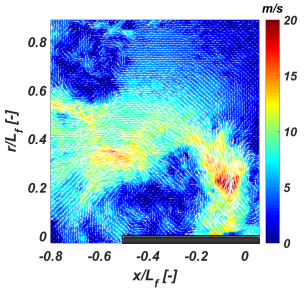

(c) $V_p = 25m/s$ - *Time* $= 1$ *ms*

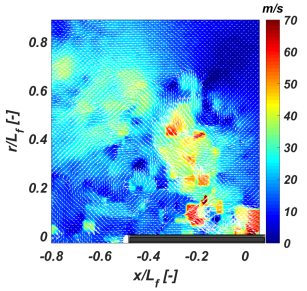

(d) $V_p = 50m/s$ - *Time* $= 1$ *ms*

Figure 4.26: PIV velocity and vector maps in plane YZ

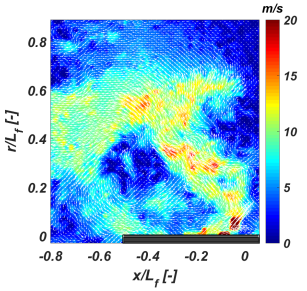

(a) $V_p = 25m/s$ - *Time* $= 2$ *ms*

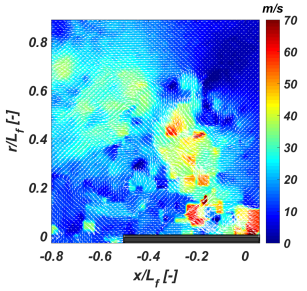

(b) $V_p = 50m/s$ - *Time* $= 2$ *ms*

Figure 4.27: PIV velocity and vector maps in plane YZ

by the averaged velocity maps. Considering the high acquisition frequency and the number of maps observable for every test it is worth representing the flow structure in statistical terms.

4.3.3.2 Spectral analysis

The spectral analysis of the data was performed by applying the Fast Fourier Tansform (FFT) function to the velocity time series on a certain number of local positions. In order to reduce the amount of data to be processed without losing important information on the jet evolution, a vertical and a horizontal lines were chosen, centered on the jet. As Figure 4.28 shows, the mean flow field was observed and the velocities on the dashed lines extracted and analysed. The FFT performed on the above

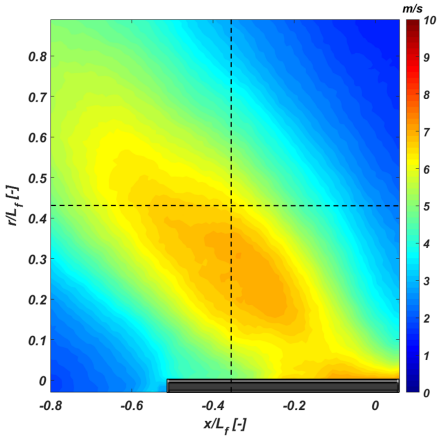

Figure 4.28: Lines on which velocity time evolution was extracted

mentioned velocities were observed in terms of frequency spectra, results are reported in Figure 4.29. The two graphs, expressed in logarithmic scale, show the presence of several similar peaks in many positions which are responsible of oscillating flow structures. The highest peak found in the vertical line is placed at 52 Hz and, at same frequency, a peak is also

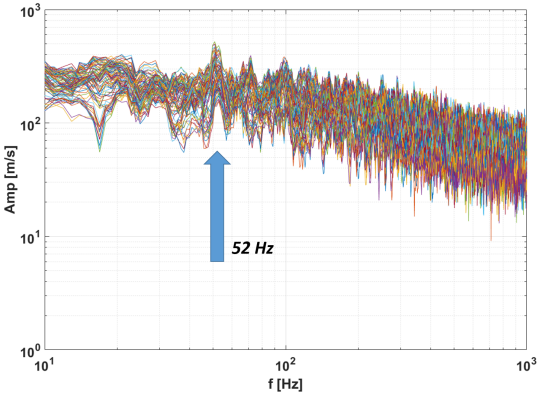

(a) Velocity spectra on vertical line

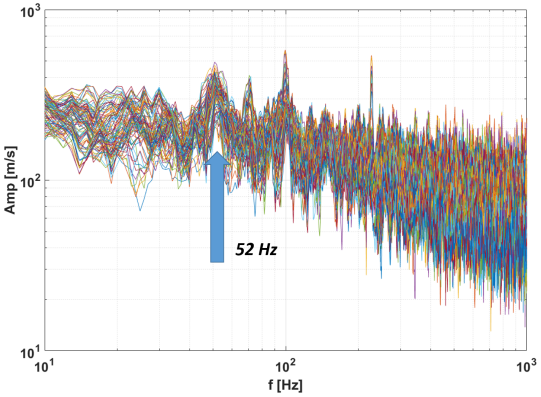

(b) Velocity spectra on horizontal line

Figure 4.29: PIV velocity spectra in test at $V_p = 25m/s$

present in the horizontal spectra. This was interpreted as an oscillating mode representative of a strong flow structure.
Hence the amplitude of this mode was mapped together with streamlines, Figure 4.30 shows the result. The streamlines show the presence of a recirculation similar to the one observed in Figure 4.26a, while the positive

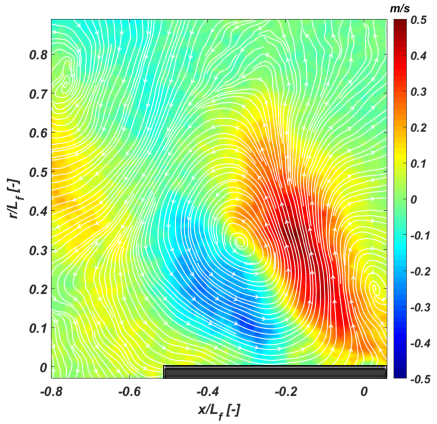

Figure 4.30: Velocity oscillating mode at 52 Hz for $V_p = 52Hz$

and negative peaks show the position where the vortex is oscillating, indeed its center is expected in the zone at zero velocity.

In order to find confirmation on this assertion, an instantaneous flow field map with a similar structure was searched and compared with the others measured after one and two periods relative to the chosen frequency $T = 1/f$. The three instantaneous flow fields are reported in Figure 4.31. They show the same recirculation starting to grow from the gear, this structure will evolve then in the same way shown in Figure 4.27.

A similar post-processing was applied to tests at $V_p = 100m/s$ a, peak at 12 Hz was found and the relative oscillating mode is reported in Figure 4.32. In this case the oscillating structure is still a vortex but placed at a higher distance from the gear. This agrees both with the lower characteristic frequency found and with the averaged results previously shown.

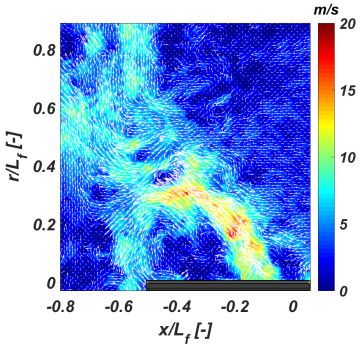

(a) Flow field at time $= t_0$

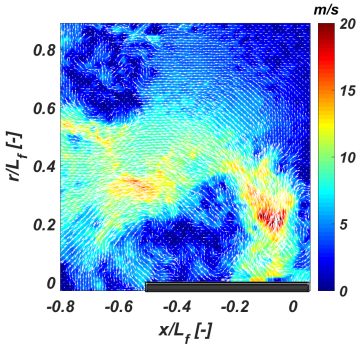

(b) Flow field at time $= t_0 + T$

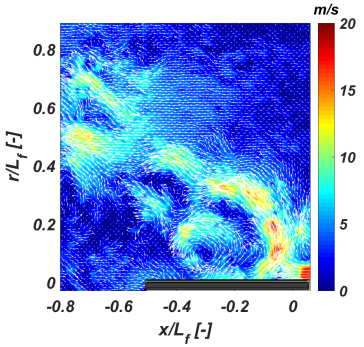

(c) Flow field at time $= t_0 + 2T$

Figure 4.31: Flow field comparison after a period of time $T = 1/f$

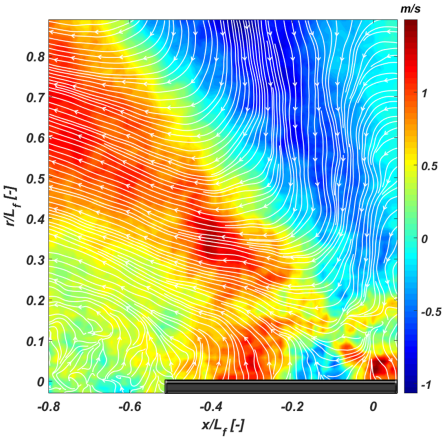

Figure 4.32: Velocity oscillating mode at 12 Hz for $V_p = 12Hz$

4.3.3.3 Proper Orthogonal Decomposition (POD) analysis

The Proper Orthogonal Decomposition (POD) is a mathematical technique, often used in statistical problems, which allows obtaining low dimensional approximate descriptions for multi-dimensional systems.
The POD procedure can be considered divided in two parts: the first is to take "snapshot" of a series of data obtaining a series of modes describing the principal flow structures characterizing the flow field, the second is to "project" the data through a selection of them. In the present study this technique has been applied as a method of description and verification of the flow structures showed by the time series of data and the spectral analysis. The large eddies present in the flow field and their evolution with time were indeed already described thanks to the high frequency acquisitions allowed by PIV instrumentation.
Closely related to the Principal Component Analysis (PCA), the Proper Othogonal Decomposition (POD) has been used, since Lumley [53] in 1967, in fluid-dynamics measurements and simulation in order to detect coherent structures present within the flow.
The implementation used in this work applies the method proposed by Sirovic in 1987 [54], named "Snapshot POD": every PIV measurement is indeed considered a snapshot of the flow. Considering a series of N measurements taken at identical positions, an average value can be calculated and constitute the mode 0. The mean is subtracted from every snapshot and the analysis is then focused only on the fluctuating velocity components.

The velocity values for every point and every time are rearranged in a matrix U from which an autocovariance matrix can be calculated as:

$$C = U^T U \tag{4.10}$$

The dimension of C is [N X N], where N is the number of instants, for this matrix the eigen-value problem can be solved:

$$C\Psi_i = \lambda_i \Psi_i \tag{4.11}$$

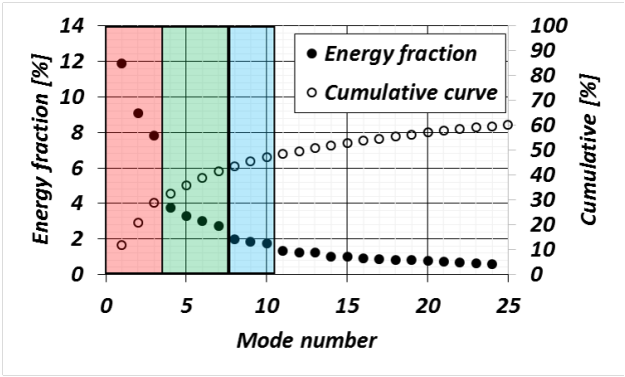

Figure 4.33: Energy fraction and cumulative curve for the first 25 modes for $V_p = 100m/s$

Obtaining a series of N eigen-values λ_i and eigen-vectors Ψ_i, they are ordered from the first to the i^{th} in descending order. Projecting the original data on the eigen-vectors we obtain the POD modes, the relative eigen-value of every POD mode represents the energy contribution of the mode to the total kinetic energy of velocity fluctuations, this means that the first modes are associated to the greatest flow structures. Further explanations on the post-processing technique can be found in the Dantec DynamicStudio Manual [55], while for a physical understanding of resulting eigen-values, eigen-vectors and modes a practical example can be found in the work of Berrino et al [56].
Coming back to gear, in order to make a complete comparison of the different techniques, results for the test at $V_p = 25m/s$ were post-processed extracting the eigen-values and vectors and projecting the modes. Figure 4.33 shows the energy fraction (black dots) together with the cumulative curve (empty dots) associated to the first 25 modes. The first three have a significant value, close to 10%, they represents the 30 % of the total energy fraction, their projections are reported in Figure 4.34, where the three modes show different recirculation. In particular the first one is very similar to the oscillating mode at 52 Hz (Figure 4.30), confirming the

importance of that oscillating mode in the balance of turbulent energy of the jet.
Then there is a drop, meaning that the successive modes are related to flow structures with lower turbulent energy as Figure 4.35 shows.
Further drops happen at mode 8 and than at the 10^{th}, after which the 50 % of the energy fraction is reached, see Figure 4.36. Successive modes are related to ever lower flow structures.

POD technique was applied also to the test at $V_p = 100m/s$. The energy fraction and cumulative curve are reported in Figure 4.37. The first three obtained modes are shown in Figure 4.38, where it is possible to notice a similitude with results obtained at $V_p = 25m/s$.
In both tests indeed the first mode reveals a single recirculation, that is placed farther for higher velocity, while there are two in second one. The third mode identifies a central recirculation surrounded by other two, in the test at $V_p = 100m/s$ however there is a wider spread of them, and the two lateral flow structure are visible only partially.
The mode 1 shows a similitude with the oscillating mode identified at 12 Hz (Figure 4.32) by means of FFT post-processing.

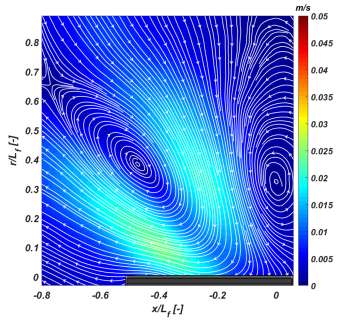

(a) POD mode 1

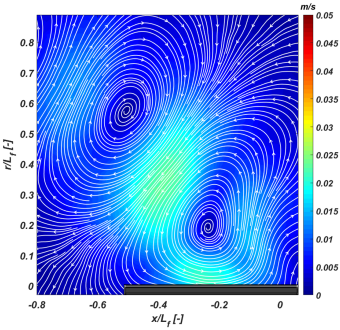

(b) POD mode 2

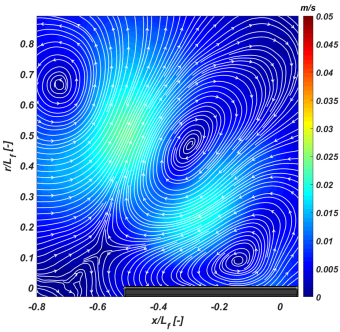

(c) POD mode 3

Figure 4.34: POD modes 1 to 3 for test at $V_p = 25m/s$

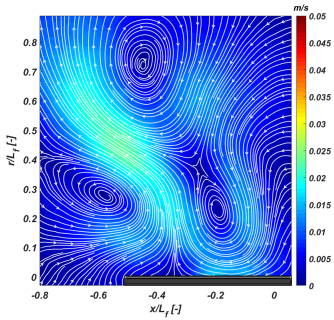

(a) POD mode 4

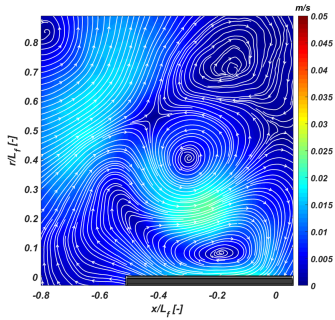

(b) POD mode 5

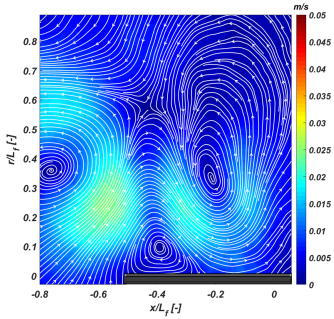

(c) POD mode 6

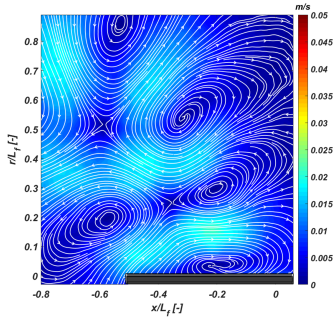

(d) POD mode 7

Figure 4.35: POD modes 4 to 7 for test at $V_p = 25m/s$

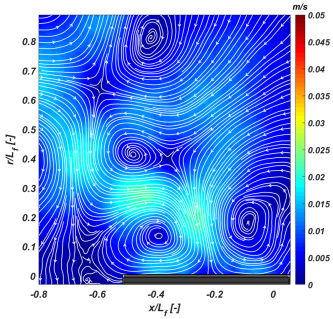

(a) POD mode 8

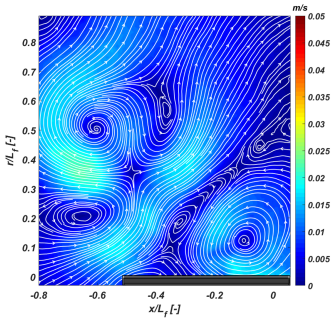

(b) POD mode 9

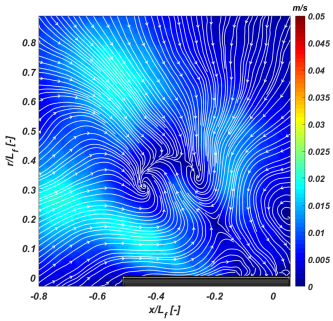

(c) POD mode 10

Figure 4.36: POD modes 8 to 10 for test at $V_p = 25m/s$

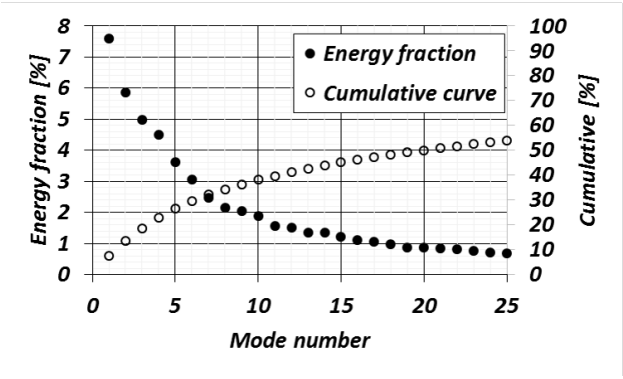

Figure 4.37: Energy fraction and cumulative for the first 25 modes for $V_p = 100m/s$

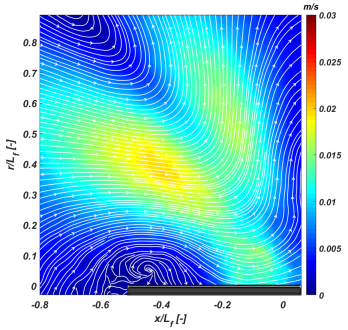

(a) POD mode 1

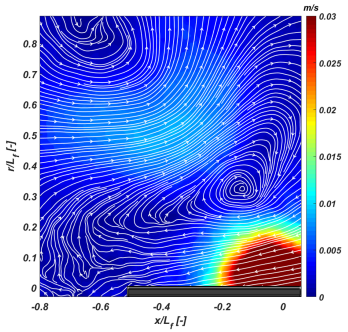

(b) POD mode 2

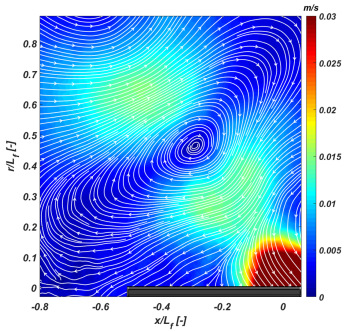

(c) POD mode 3

Figure 4.38: POD modes 1 to 3 for test at $V_p = 100m/s$

Chapter 5

Oil jet

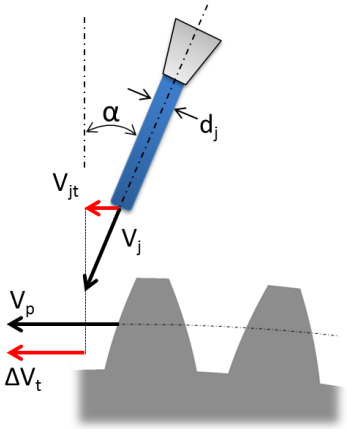

Figure 5.1: Oil jet angular direction definition

In this chapter the oil injection mechanism will be treated in terms of torque measurements and high speed visualizations. The oil control unit, already showed in Chapter 3, was exploited to provide the right pressure and temperature of oil MIL-23699 used for the experiments.

A single oil jet was tested at different working conditions. Oil temperature was fixed at $80°C$ and the mass flow rate was varied in order to set the jet Reynolds number Re_j up to 5000.
Before starting the test, some time was dedicated to analyse the jet atomization mechanisms by means of image acquisitions at different working conditions.
Two typical working conditions for gearbox used in aeronautical applications were replicated: the take-off, at ambient pressure and maximum pitch velocity of 100 m/s, and the cruise condition, at reduced pressure ($\rho \approx 0.3$) and velocity, 80 m/s. Further tests have been conducted in a preliminary phase in order to decouple the effects of pressure and velocity.
The jet was generated by a spraybar whose distance and angular direction with respect to the gear were varied following the test matrix reported in table 5.1. The definition of the injection angle is well described by Figure 5.1.

Conf.	T1	T2	T3	T4	T5	T6	T7	T8	T9	T10
$\frac{L_j}{D_p}[-]$	0.013	0.013	0.013	0.013	0.013	0.5	0.5	0.5	0.5	0.5
$\alpha[^\circ]$	0	20	40	60	-20	0	20	40	60	-20

Table 5.1: Oil injection test matrix

For every of the described positions a single oil jet was tested at different working conditions.

5.1 Theoretical 0D model

The tests also helped to provide an experimental verification of a simple theoretical 0D model, proposed by Fondelli [37, 38], able to well predict the torque augmentation in presence of oil jet lubrication.
The model is quite simple, similarly to the model proposed by Diab [7] for windage calculation, it is based on the calculation of the oil momentum variation during the interaction with the tooth.
Considering the pitch velocity as the speed reachable by the oil after the

impact, we can calculate the force necessary to the fluid acceleration as:

$$F = m_j \Delta U_j \longrightarrow \tau = m_j \Delta V_j R_p \tag{5.1}$$

Applying the force to the pitch line radius, we obtain the torque.
This simple equation is able to model the effects of different oil mass flow rates and temperatures, rotating speeds, oil angular direction. All these parameters can be explicitly expressed:

$$\tau = \frac{\pi d_j^2}{4} \rho_j V_j R_p \big(\omega R_p - V_j \sin(\alpha)\big) \tag{5.2}$$

Where d_j, ρ_j and V_j are the jet diameter, density and velocity respectively, α is the injection angle expressed following the scheme in Figure 5.1.
The most important hypothesis for this model is that all the oil mass flow rate is accelerated in same way: this is not always true considering that the tooth surface is inclined and the impact can occur at different radii having different peripheral velocities. Moreover there is a portion of oil impacting on the top land of tooth, where it can be accelerated by viscous forces, not really by an impact. Finally the oil break-up occurring before the impact can alter its velocity or reduce the effective mass flow rate taking part to the phenomenon. However at this moment no much information are available to provide a mass flow correction taking into account the aforesaid problems, nevertheless results shown in the following sections will provide some evidence of the need of a finer model.
It can be useful to express the torque as the moment coefficient C_m, in order to reduce the effects of gear rotating velocity and ambient pressure:

$$C_m = \frac{\tau}{0.5 \rho_{air} \omega^2 R_p^5} = \frac{\frac{\pi d_j^2}{4} \rho_j V_j R_p \big(\omega R_p - V_j \sin(\alpha)\big)}{0.5 \rho_{air} \omega^2 R_p^5} \tag{5.3}$$

After few manipulations, equation 5.3 becomes:

$$C_m = \frac{\pi d_j^2}{2 R_p^2} \frac{\rho_j V_j}{\rho_{air} V_p} \Big(1 - \frac{V_j}{V_p} \sin(\alpha)\Big) \tag{5.4}$$

Equation 5.4 shows the three principal groups affecting the moment coefficient:

- $\frac{\pi d_j^2}{2R_p^2}$: it is a geometrical parameter, fixed for a fixed geometry;
- $\frac{\rho_j V_j}{\rho_{air} V_p}$: in this group the oil and the environment characteristics are linked;
- $\left(1 - \frac{V_j}{V_p}\sin(\alpha)\right)$: this third group takes into account the oil injection angle.

5.2 Oil jet break-up regimes

Before showing the results of the interaction between oil jet and gear, it is worth dedicate few words on the jet atomization characteristics. It is well known indeed that both cooling and lubricating capability are maximized if the jet is able to generate an impingement on the teeth and, on the other hand, it manages to reach the deepest surfaces of the gear. This means in fact that the jet should be coherent and break-up should be avoided.
In a liquid column moving in a gaseous mean, many internal and external forces act on its surface generating oscillations and perturbations. When a critical condition is reached the result is the surface destruction and the generation of droplets. This event can be foreseen, there are three parameters able to describe the flow break-up regimes:

- Reynolds number,
$$Re_j = \frac{\rho_j V_j D_j}{\mu} \tag{5.5}$$
- Weber number, it represents the ratio between the aerodynamic forces and the surface tension, it can be defined in two ways depending on the application:
  –
$$We = \frac{V_j^2 \rho_j D_j}{\sigma} \tag{5.6}$$

–

$$We_{cf} = \frac{V_{air}^2 \rho_{air} D_j}{\sigma} \tag{5.7}$$

In the first case both velocity and density are characteristic of the oil jet, the other parameter is used to describe a jet in a cross-flow.

- Ohnesorge number

$$Oh = \frac{\sqrt{We}}{Re_j} = \frac{\mu}{\rho \sigma D_j} \tag{5.8}$$

It relates the viscous forces to inertial and surface tension forces.

A pioneer work on the expected types of break-up was done by Ohnesorge in 1937, and further improved by many researchers during the last century. Reitz in 1978 [57] proposed the definition of four break-up regimes defined by as many zone on a Oh vs Re_j chart. The chart is reported in Figure 5.2 together with the experimental points to be tested.

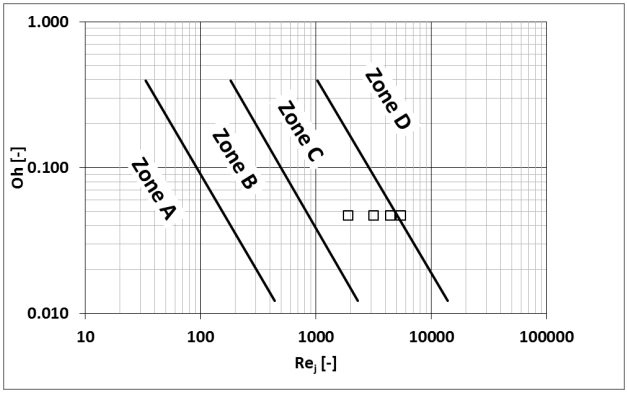

Figure 5.2: The four break-up zones

An idea of what the zones means in terms of liquid break-up is given in Figure 5.3, taken from the work of Schenider [12]:

- **Zone A - Rayleigh break-up**: it happens at very low velocities, only very small axial-symmetric perturbations are present, bringing at the end to the jet break-up in big droplets, larger than the jet diameter.
- **Zone B - First wind-induced breakup**: the increase of the velocity brings to a higher influence of the aerodynamic forces on the jet surface; from the liquid column droplets start to secede, droplet dimensions are expected to be of the same order of magnitude of the jet diameter.
- **Zone C - Second wind-induced breakup**: this zone is dominated by the same phenomenon as the preceding one but a further increase of the velocity accelerate the jet break-up; moreover, smaller droplets are generated.
- **Zone D - Atomization**: in this case the velocity is so high that the break-up starts immediately and the liquid column does not exists any more.

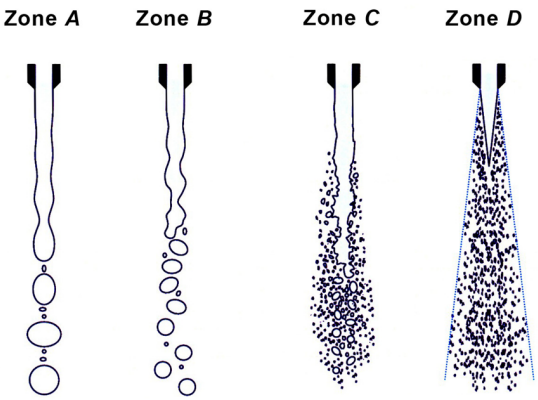

Figure 5.3: Typical image of the four primary breakup regimes [12]

In gearbox applications acceptable values of Re_j is usually higher than 1500; for this reason the four test points presented in Figure 5.2 were chosen for the present investigation: three of the four test points are expected to be in the Zone C and one in between the Zones C and D. Nevertheless, as proposed by Scnheider [12], also the ambient where the jet is injected should have a role in the break-up. In particular a reduced pressure should move to the right the divisions. In order to understand the effect of pressure expected on the tests, the same points of Figure 5.2, have been plotted in another graph proposed by Schneider [12], where the four zones are reported as a function of jet Reynolds and air density, see Figure 5.4. It is possible to observe that, following this definition,

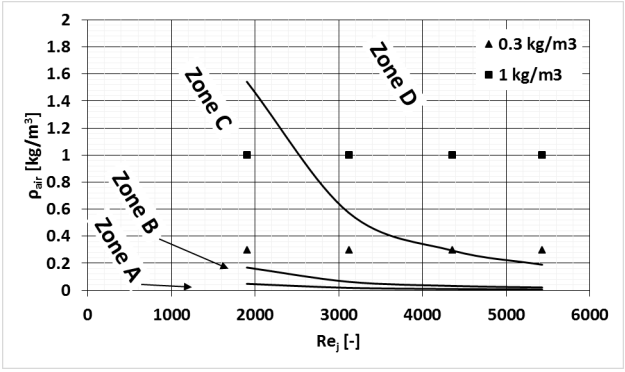

Figure 5.4: The regimes of liquid breakup as a function of Reynolds number and ambient gas density [13]

for both the pressure conditions points at $Re_j = 1900$ fall in the zone C, while the ones at $Re_j = 4300$ and $Re_j = 5400$ in the zone D. Differences are expected due to pressure variation only for $Re_j = 3100$.

In the present study it has to be considered that the jet is not delivered in an undisturbed environment, as showed by PIV results indeed. An important air flow field is present around the gear which can anticipate the liquid break-up.

Sallam et al. [13] provided experimental evidence on the liquid break-up

of liquid column immersed in a cross-flow demonstrating that for laminar jets the dominating parameter is the We_{cf}, at which different kind of break-up modes are associated, see Figure 5.5.

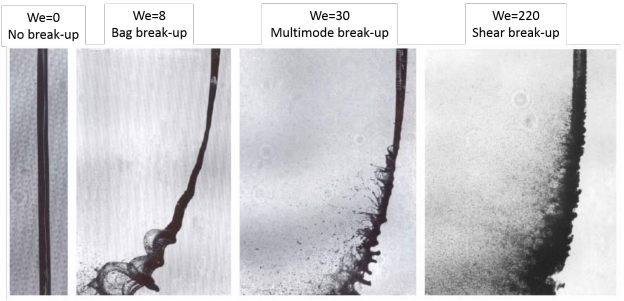

Figure 5.5: The regimes of liquid breakup at different We_{cf} for a laminar jet

5.3 High speed visualizations

Results of the experimental investigation on oil jet lubrication can be divided in two main parts: one concerning the high speed visualizations focused at understanding which kind of break-up is established at the various working conditions, the other intends to verify the power losses due to different Re_j, jet to gear distance and inclination.
The typical values of Re_j used in these applications are higher than 1900 and are expected to generate turbulent jets. However few acquisitions were made also with a reduced mass flow rate in order to observe the effect of the air cross-flow generated by the gear and to apply a We_{cf} also in a rotating flow field.
In order to have an idea of the jet regime, the discharge coefficient was calculated for a series of Reynolds numbers, obtaining the curve reported in Figure 5.6:

$$C_d = \frac{m_{real}}{m_{is}} \tag{5.9}$$

The curve is constituted by three parts defined by the presence of a peak

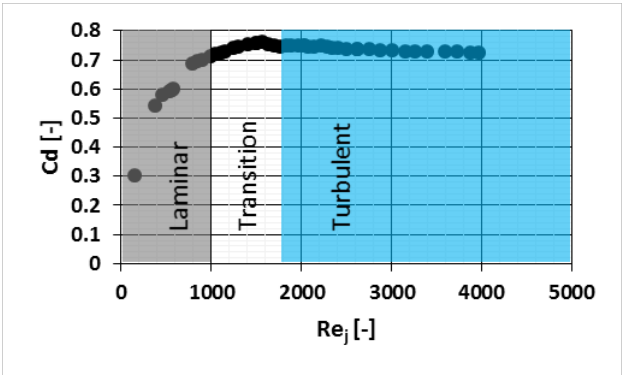

Figure 5.6: Discharge coefficient vs Reynolds number for the tested spray-bar

that indicates a transition from laminar to turbulent regime: $Re_j < 1000$ are associated to laminar jets, $Re_j > 2000$ to turbulent.

5.3.1 Laminar jet

The oil mass flow rate was reduced to a very low value, also the temperature was set at $30°C$ increasing the oil viscosity, a $Re_j \approx 200$ was obtained assuring the jet to be laminar.
At this point, following the study of Sallam et al. [13], the leading parameter is expected to be We_{cf}, in this case there is not a well defined flow field, hence the pitch velocity was chosen for defining the cross-flow speed. Three rotating velocities were varied in order to obtain $We_{cf} = 2, 37, 366$.

Results are summarized in Figure 5.7, three acquisition frames were chosen in order to show the passage of a tooth under the jet. A good agreement between expected and observed break-up modes is visible.
At low We_{cf} the jet arrives undisturbed on the gear. Moreover, given the low rotating velocity, the oil is able to reach the bottom of the teeth

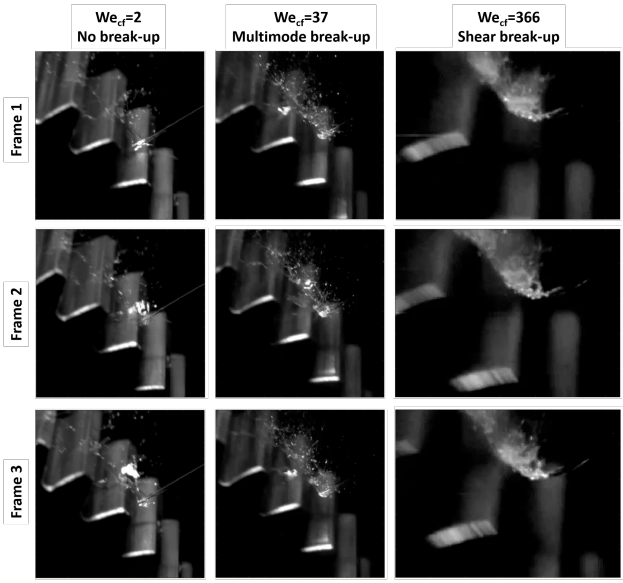

Figure 5.7: Effect of We_{cf} defined using gear pitch pitch velocity on a laminar oil jet

spacing. The impact with the surface generates a film spreading in all directions; a portion of oil however is flung off going towards the preceding tooth.

For $We_{cf} = 37$ the jet starts to be bended and big drops and ligaments are generated from it. In this case the point of impact is at a higher radius, closer to the tip of the tooth, however the oil is split in two parts: one generates the film on the surface and the other is thrown away.

Further increase of rotating velocity causes a stronger air flow investing the oil jet, a big population of small drops is seceded from it and no oil enters the teeth spacing.

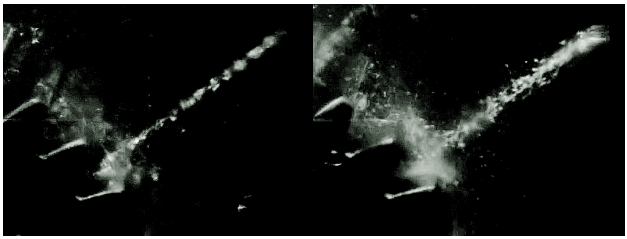

(a) Visualization of oil jet at $Re_j = 1900$

(b) Visualization of oil jet at $Re_j = 3100$

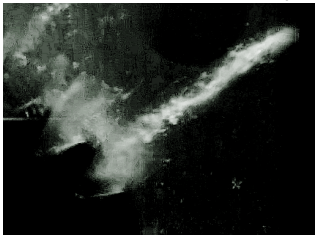

(c) Visualization of oil jet at $Re_j = 4300$

Figure 5.8: Oil jet break-up: effect of Re_j at ambient conditions

5.3.2 Turbulent jet

A preliminary jet observation was done with the gear stopped for the first three Reynolds values at ambient conditions, in order to verify if the jet column shape follows the prevision made by using dimensionless groups. Results are reported in Figure 5.8 where the effect of Re_j is clearly visible: the liquid column is coherent only in the first image 5.8a, Figures 5.8b and 5.8c on the contrary show a jet completely surrounded by droplets. Moreover the jet diameter remains almost constant for the lowest Re_j while increases for the other two, a typical behaviour of turbulent jets, as suggested by Sallam et al. [13].

Oil jet visualizations performed with the high speed camera will be here presented for jet $\frac{L_j}{D_p} = 0.5$, inclinations of 0 and 40 degrees and in both Take-off and Cruise conditions. Four Re_j will be observed in order to highlight the different break-up regimes. For every test three images

showing the tooth passage under the jet are reported.
The first comparison can be done between Figure 5.9 and 5.10: in both the figures, increasing the Reynolds number an increase of the jet spreading and the generation of droplets can be observed. As expected, the air pressure plays a secondary role in these tests, with the exception of $Re_j = 3100$ where the jet break-up is already present in Take-off condition unlike in the Cruise one. The gear velocity on the contrary has a central role in generating a strong cross flow in the vicinity of the teeth, which is responsible for an oil fog generation.
When the oil jet reaches the gear indeed, a portion of it forms a liquid film on the surface while another part is flung off and recirculated by the air.
The oil column shape however, seems not to be affected by the air cross-flow generated by the rotation and reaches the gear in radial direction without being deformed. This is in agreement with PIV results showed in section 4.3, where Figure 4.16 pointed out the quick tangential velocity decay going away from the gear.
Further considerations may be done observing the jet having an inclination of $\alpha = 40$ degrees. In Figures 5.11 and 5.12 again it is possible to observe the effect of pressure at $Re_j = 3100$ and the denser fog generated by a higher rotating velocity in Take-off conditions, however also a negative effect of the inclination on the oil break-up is visible. In this case indeed, due to the inclination, the oil is subjected for longer time and space to the high velocity flow field surrounding the gear. As a consequence the liquid column is bended towards the air velocity direction.
Another aspect concerning these latter tests is that the real jet to gear distance is as higher as the the angle increases (or decreases) because the spray-bar position is fixed for all the angular variations. This causes the jet to arrive in the gear proximity after longer time and so in a worst break-up condition.
In aero-engine applications the oil jets are necessary, besides the lubrication scope, in order to cool the gear teeth, they are designed to generate an impingement assuring a high heat transfer coefficient zone. If the jet is

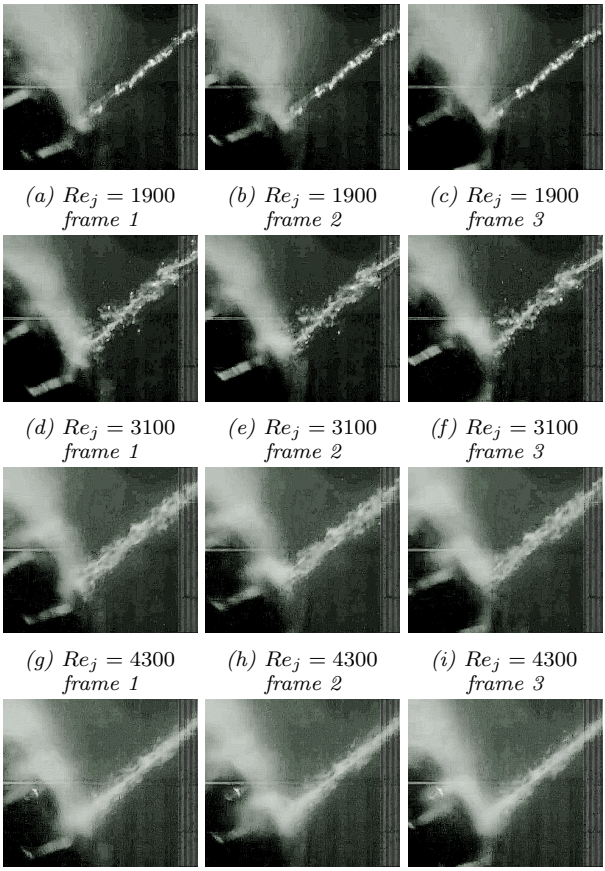

(a) $Re_j = 1900$ *frame 1* (b) $Re_j = 1900$ *frame 2* (c) $Re_j = 1900$ *frame 3*

(d) $Re_j = 3100$ *frame 1* (e) $Re_j = 3100$ *frame 2* (f) $Re_j = 3100$ *frame 3*

(g) $Re_j = 4300$ *frame 1* (h) $Re_j = 4300$ *frame 2* (i) $Re_j = 4300$ *frame 3*

(j) $Re_j = 5400$ *frame 1* (k) $Re_j = 5400$ *frame 2* (l) $Re_j = 5400$ *frame 3*

Figure 5.9: High speed visualizations in Take-off condition and $\alpha = 0$

subjected to the air cross-flow, or the injection hole itself does not assure a compact liquid column to be delivered from the spray-bar, its cooling effect can be strongly reduced. Part of the oil mass flow can be lost before impacting or the impact itself can be not strong enough to generate a high heat transfer impingement.

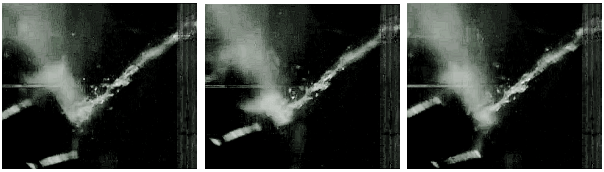

(a) $Re_j = 1900$ *frame 1*

(b) $Re_j = 1900$ *frame 2*

(c) $Re_j = 1900$ *frame 3*

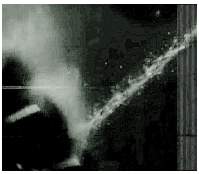

(d) $Re_j = 3100$ *frame 1*

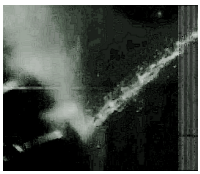

(e) $Re_j = 3100$ *frame 2*

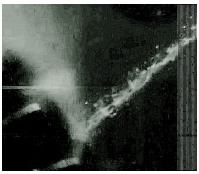

(f) $Re_j = 3100$ *frame 3*

(g) $Re_j = 4300$ *frame 1*

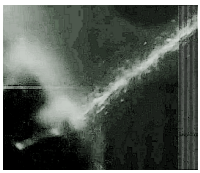

(h) $Re_j = 4300$ *frame 2*

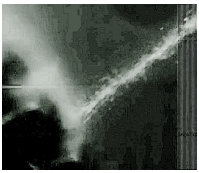

(i) $Re_j = 4300$ *frame 3*

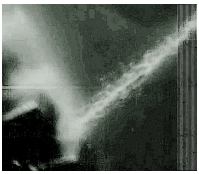

(j) $Re_j = 5400$ *frame 1*

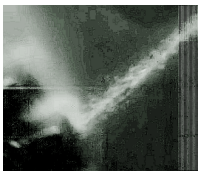

(k) $Re_j = 5400$ *frame 2*

(l) $Re_j = 5400$ *frame 3*

Figure 5.10: High speed visualizations in Cruise condition and $\alpha = 0$

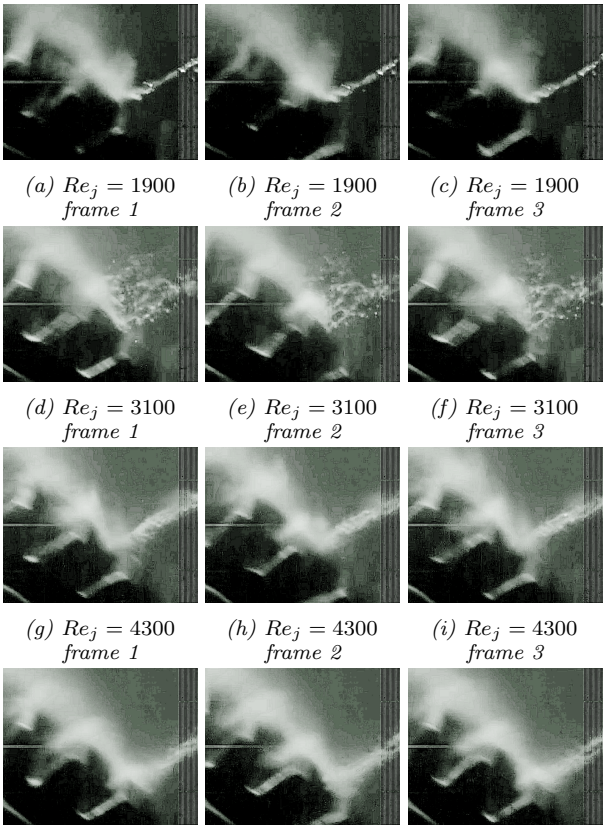

(a) $Re_j = 1900$ *frame 1* | *(b)* $Re_j = 1900$ *frame 2* | *(c)* $Re_j = 1900$ *frame 3*

(d) $Re_j = 3100$ *frame 1* | *(e)* $Re_j = 3100$ *frame 2* | *(f)* $Re_j = 3100$ *frame 3*

(g) $Re_j = 4300$ *frame 1* | *(h)* $Re_j = 4300$ *frame 2* | *(i)* $Re_j = 4300$ *frame 3*

(j) $Re_j = 5400$ *frame 1* | *(k)* $Re_j = 5400$ *frame 2* | *(l)* $Re_j = 5400$ *frame 3*

Figure 5.11: High speed visualizations in Take-off condition and $\alpha = 40$

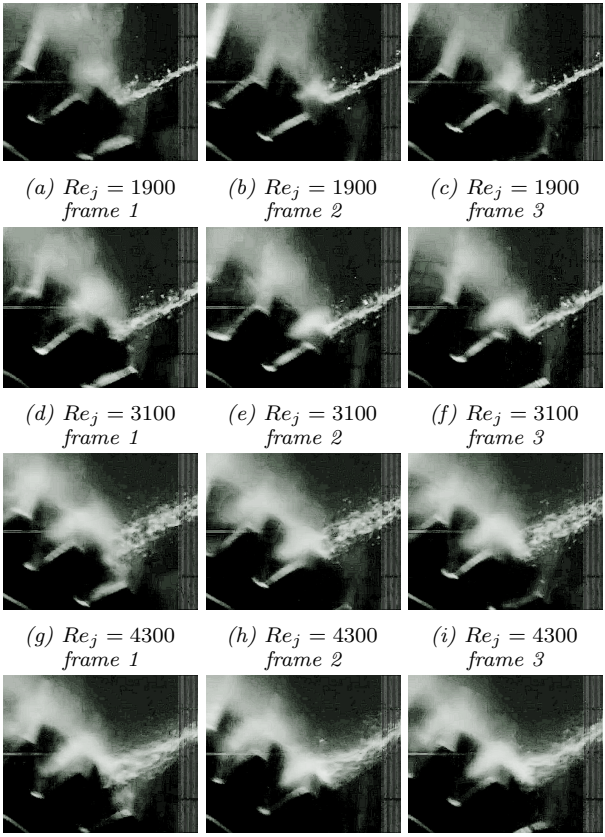

(a) $Re_j = 1900$ *frame 1* | *(b)* $Re_j = 1900$ *frame 2* | *(c)* $Re_j = 1900$ *frame 3*

(d) $Re_j = 3100$ *frame 1* | *(e)* $Re_j = 3100$ *frame 2* | *(f)* $Re_j = 3100$ *frame 3*

(g) $Re_j = 4300$ *frame 1* | *(h)* $Re_j = 4300$ *frame 2* | *(i)* $Re_j = 4300$ *frame 3*

(j) $Re_j = 5400$ *frame 1* | *(k)* $Re_j = 5400$ *frame 2* | *(l)* $Re_j = 5400$ *frame 3*

Figure 5.12: High speed visualizations in Cruise condition and $\alpha = 40$

5.4 Power losses

Tests were conducted by measuring the overall torque and then subtracting the effects of the bearings friction and gear windage by using the correlations reported in Chapters 3 and 4.
The effect of pitch velocity was firstly investigated at ambient condition, as could be expected it heavily affects the power losses, as showed in Figure 5.13. From a first observation of these results it can be noticed

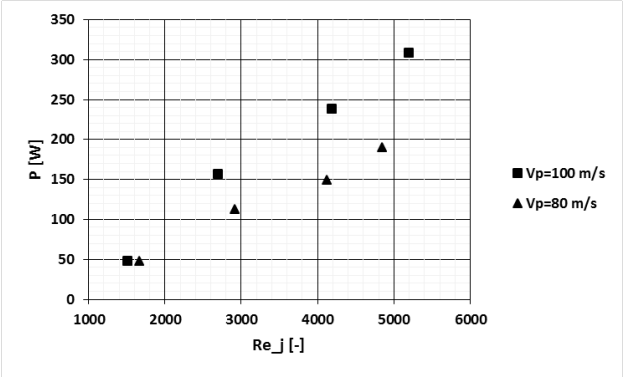

Figure 5.13: Power losses due to oil injection at ambient pressure: effect of pitch velocity

the linear trend of all the curves with Re_j, which has of course a physical explanation for which we refer to the theoretical model explained in section 5.1.
The test points summarized in Table 5.1 can be divided in two main groups considering the spray-bar distance from the gear. A first series of tests were performed placing the spray-bar in the closest position in order to minimize the effects of the liquid break-up on oil velocity and trajectory, which is expected following the discussion and tests reported in the previous section. In such a way the theoretical model proposed can be verified without introducing other aspects to be modelled.

The results relative to Take-off and Cruise conditions are reported in

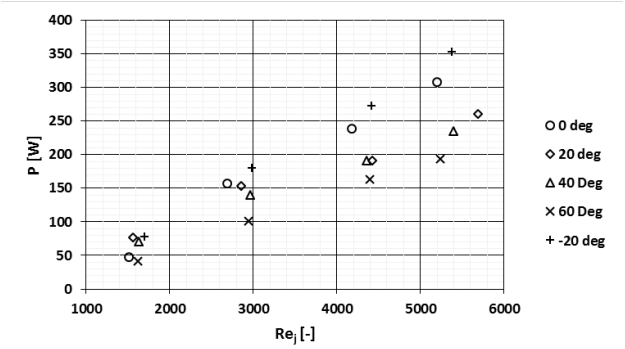

(a) Power losses for oil jet injection in Take-off conditions at $\frac{L_j}{D_p} = 0.013$

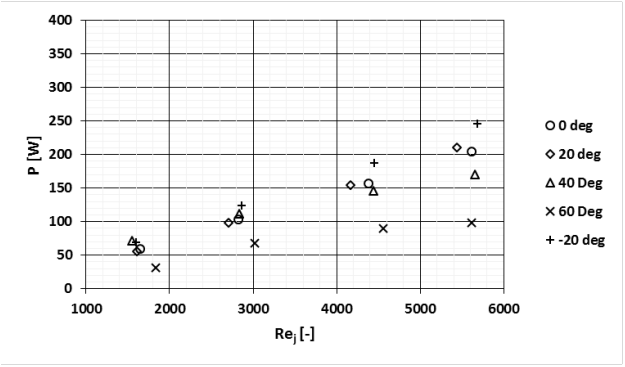

(b) Power losses for oil jet injection in Cruise conditions at $\frac{L_j}{D_p} = 0.013$

Figure 5.14: Power losses for oil jet injection at $\frac{L_j}{D_p} = 0.013$

Figure 5.14 where the power losses are plotted against the jet Reynolds number. A linear trend is visible for all the tests, given the direct proportionality expected between the torque and the oil mass flow rate.
The differences between Cruise and Take-off conditions are basically due to the rotating velocity of the gear. For this reason all the curves present in Figure 5.14a are higher than the ones in Figure 5.14b. The injection

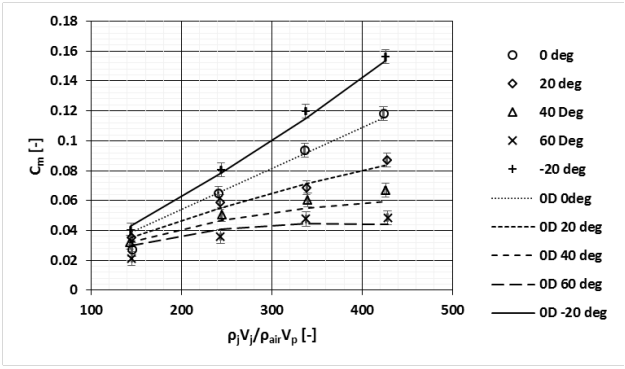

(a) C_m vs $\frac{\rho_j V_j}{\rho_{air} V_p}$ for oil jet injection in Take-off conditions at $\frac{L_j}{D_p} = 0.013$

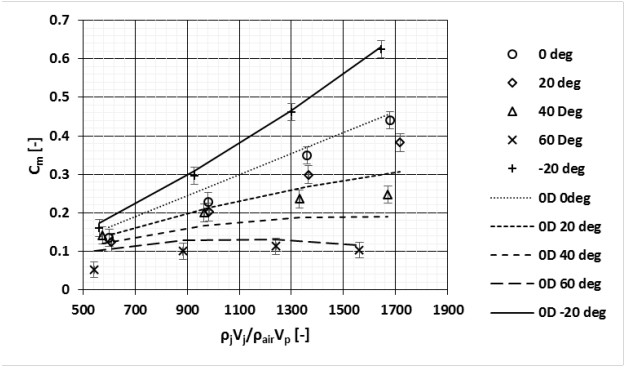

(b) C_m vs $\frac{\rho_j V_j}{\rho_{air} V_p}$ for oil jet injection in Cruise conditions at $\frac{L_j}{D_p} = 0.013$

Figure 5.15: C_m vs $\frac{\rho_j V_j}{\rho_{air} V_p}$ for oil jet injection at $\frac{L_j}{D_p} = 0.013$

angle affects the oil tangential velocity, causing a torque reduction if $\alpha > 0$ an augmentation otherwise.

The data showed in Figure 5.14 can be expressed in terms of C_m vs $\frac{\rho_j V_j}{\rho_{air} V_p}$ and compared with the equation 5.4. In Figure 5.15 the predicted C_m values are compared with experiments, plotted together with uncertainty

bounds. A fairly good agreement can be noted between the predicted and measured losses, both for Take-off and Cruise conditions. Few differences arise at low jet velocities that may be attributed to a higher windage effect on the oil column.

The general good predictions of the model also demonstrate that the effect of pressure is negligible in this configuration. Nevertheless in order to better confirm this statement, further tests were performed. Figure 5.16a shows the effect of pressure on test at $V_p = 80m/s$ and $\alpha = 0°$, while Figure 5.16b shows the test at $V_p = 100m/s$ and $\alpha = 60°$ which is the worst configuration considering the higher air velocity around the gear and the longer distance for the oil to be travelled from the spray-bar to the gear teeth, due to the high inclination angle.

No significant effects were found for both the tests. This can be explained by the fact that the principal source of loss is due to the work extracted by the gear for the oil acceleration after the impact with the tooth, if the same amount of oil arrives on the gear at similar velocity the power loss should be the same. The air pressure can affect the oil column causing a different break-up but, as already mentioned, if the injection is close to the gear, little to null differences are expected.

After having proved the good quality of the 0D model on the simplest configuration, we can go to observe what happens if the jet is delivered from a higher distance, such as $\frac{L_j}{D_p} = 0.013$.

Results are here directly reported in terms of C_m vs $\frac{\rho_j V_j}{\rho_{air} V_p}$ together with the values predicted by equation 5.4.

As shown by Figure 5.17, in this case the model overestimates the C_m value for all the configurations tested. As already mentioned an effect of the break-up is expected: at the time of the impact the jet can have a reduced velocity, moreover it is possible that a portion of the mass flow rate is dispersed before touching the gear.

The Take-off condition seems to be more affected than the Cruise. This may be due to the higher pressure which can have a not negligible effect. This was proved by repeating the comparison showed in Figure 5.16b and reported in Figure 5.18. With an increased distance a higher air pressure

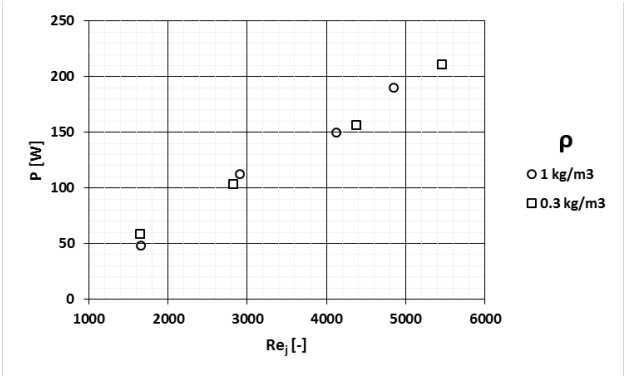

(a) Power losses due to oil injection delivered from $\frac{L_j}{D_p} = 0.013$ *at* $V_p = 80m/s$ *and* $\alpha = 0°$ *effect of ambient pressure*

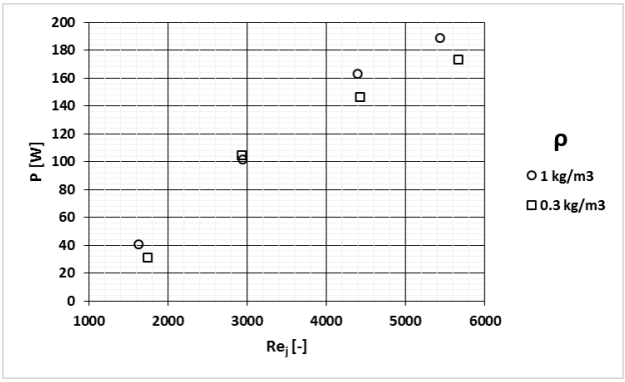

(b) Power losses due to oil injection delivered from $\frac{L_j}{D_p} = 0.013$ *at* $V_p = 100m/s$ *and* $\alpha = 60°$ *effect of ambient pressure*

Figure 5.16: Effect of pressure on oil injection power losses

is responsible for a stronger break-up and the jet is already destroyed when arrives to the gear.

The torque losses reduction can be considered a good effect for gearbox applications, however the oil break-up can be a problem in terms of efficiency of lubrication and cooling, given the velocity reduction and the

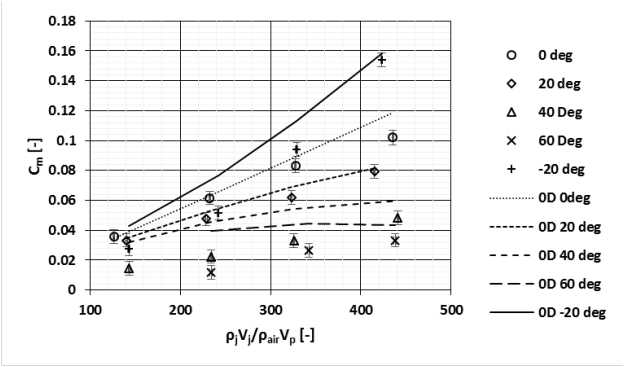

(a) C_m vs $\frac{\rho_j V_j}{\rho_{air} V_p}$ for oil jet injection in Take-off conditions at $\frac{L_j}{D_p} = 0.5$

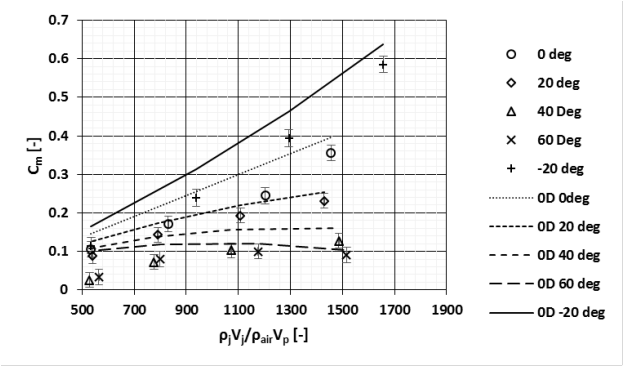

(b) C_m vs $\frac{\rho_j V_j}{\rho_{air} V_p}$ for oil jet injection in Cruise conditions at $\frac{L_j}{D_p} = 0.5$

Figure 5.17: C_m vs $\frac{\rho_j V_j}{\rho_{air} V_p}$ for oil jet injection at $\frac{L_j}{D_p} = 0.013$

portion of oil not able to reach the gear.

Concerning the first aspect, the jet has to be fast enough to enter deep in the teeth spacing. For the other one, a coherent jet is able to impinge on the surface producing a zone at elevated heat transfer coefficient, a series of droplets may not give the same result.

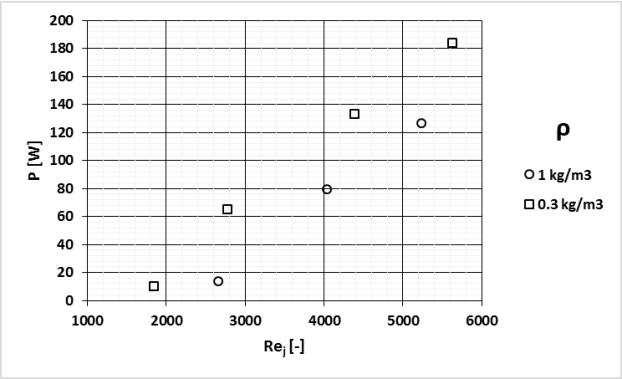

Figure 5.18: Power losses due to oil injection delivered from $\frac{L_j}{D_p} = 0.5$ *at* $V_p = 100m/s$ *and* $\alpha = 60^\circ$ *effect of ambient pressure*

High speed visualizations may help understanding what really happens during and after the impact instant and to better analyse the results previously reported.

Chapter 6

Conclusions and future work

A rotating test rig, designed to study single or meshing gears, was exploited in the reported experimental campaign with the goal of understanding the fluid-dynamic mechanisms responsible for power losses in a gearbox system for aero-engine applications.
The spur gear is enclosed in a sealed test chamber, in such a way pressure can be reduced as low as 30 kPa in order to provide realistic conditions for aircraft engine applications. The experiments were conducted varying the gear rotating velocity obtaining a maximum pitch velocity of $V_p = 100m/s$.
Windage losses results available in literature only concern tests at ambient pressure, they were compared with present measurements showing a fairly good agreement. Tests at very low pressure were performed showing a power loss strong reduction. All the collected data showed to be well reduced by a dimensionless parameter, that is the moment coefficient C_m.
PIV technique was exploited to provide reliable results on the flow field generated at ambient conditions by the gear: two different measured planes were investigated. One of the most important findings of this investigation was the visualization of the flow recirculation happening within the teeth spacing, so far observed only by CFD simulations. An important effect of the backplate on bounding the jet-like structure generated by

the gear was observed.
Experimental results have been exploited also to validate a CFD model that was used to carry out a series of numerical simulations supporting the experimental evidence.
Further investigations were performed on power losses due to oil jet lubrication. Both the rotating speed and pressure, as well as the oil jet mass flow rate, were varied in order to reach working conditions typical for take-off and cruise.
High speed visualizations were performed in order to observe the gear to jet interaction both in terms of jet impact on the teeth and fluid-dynamic interaction with the environment where the jet is delivered. Findings of this first step showed a jet break-up happening at $Re_j > 3100$ at ambient pressure, while lowering the air density this limit was found to rise at $Re_j = 4300$. No interaction with the cross flow generated by the gear rotation was found given the high values of Re_j. Increasing its inclination however, the oil jet spends more time in the rotating boundary layer and this gives a deteriorating effect on the jet break-up.
Power losses measurements were performed in Cruise and Take-off conditions, findings of this investigation showed that power losses are basically affected by jet velocity and gear rotating speed. The inclination angle can be responsible for losses reduction if a tangential velocity in the same direction of rotation of the gear is provided.
The distance from which the oil jet is delivered affects the break-up of the liquid column. In this case also the ambient pressure plays a role: if it is lower a more coherent jet structure reaches the gear, having a better lubricating effect but higher power losses.
Results have been also exploited for the validation of 0D model able to well predict the power losses due to jet impact with the gear. The model is not able to take into account the power losses reduction due to jet break-up.
The experimental work done was useful to deepen the knowledge of fluid-dynamic losses in gearbox systems separately. However, even if realistic boundary conditions have been imposed, such as rotating velocity, air

pressures and oil temperature and mass flow rates, further increase in similitude with a real gearbox system is necessary. The next step forward the complete epicyclic transmission will be the study of the meshing losses: experimental investigations are foreseen on the test rig aimed at evaluating the effects of rotating velocity and ambient pressure in absence of lubrication. Afterwards, oil lubrication will be imposed, in and out of mesh.

The results will be useful also to provide a reliable test case for CFD simulations that will take place in parallel with the experiments.

The last step foreseen for this activity will be the testing of a complete epicyclic transmission equipped with a sun gear and three planetary enmeshing with the sun and a static annular gear. A rotating lubricating system will provide the oil necessary to allow the transmission to work properly. Tests will be performed in terms of resistant torque evaluation and PIV within the enmeshing regions. Effects of rotating velocity and ambient pressure will be investigated.

Bibliography

[1] *Visual inspections of commercial jet engines. URL http://www.olympus-ims.com/en/applications/rvi-passenger-jet-engine.* .

[2] Kurzke, J. Fundamental differences between conventional and geared turbofans. In *ASME Turbo Expo 2009: Power for Land, Sea, and Air*, pages 145–153. American Society of Mechanical Engineers, 2009.

[3] *Pure power engine family specifications. URL http://www.pw.utc.com.* .

[4] *Rolls-Royce UltraFan high-bypass geared turbofan engine. URL http://www.rolls-royce.com/products-and-services/civil-aerospace/products/future-products/ultrafan.aspx.* .

[5] Anderson, N E and Loewenthal, S H. "Effect of geometry and operating conditions on spur gear system power loss." *Journal of mechanical design*, 103(1):151–159, 1981.

[6] Dawson, PH. "Windage loss in larger high-speed gears." *Proceedings of the Institution of Mechanical Engineers, Part A: Journal of Power and Energy*, 198(1):51–59, 1984.

[7] Diab, Y, Ville, F, Changenet, C, and Velex, P. Windage losses in high speed gears: Preliminary experimental and theoretical results. In *ASME 2003 International Design Engineering Technical Conferences and Computers and Information in Engineering Conference*, pages 941–947. American Society of Mechanical Engineers, 2003.

[8] Al-Shibl, K, Simmons, K, and Eastwick, CN. "Modelling windage power loss from an enclosed spur gear." *Proceedings of the Institution of Mechanical Engineers, Part A: Journal of Power and Energy*, 221 (3):331–341, 2007.

[9] Fondelli, T. *Numerical Investigation of Fluid-Dynamic Losses in Power Gearboxes For Aero-Engine Applications.* PhD thesis, University of Florence, 2015.

[10] Akin, LS, Townsend, DP, and Mross, JJ. "Study of lubricant jet flow phenomena in spur gears." 1974.

[11] El-Bayoumy, E, Akin, L S, Townsend, D P, and Choy, FC. The role of thermal and lubricant boundary layers in the transient thermal analysis of spur gears. Technical report, DTIC Document, 1989.

[12] Schneider, B M. *Experimentelle Untersuchungen zur Spraystruktur in transienten, verdampfenden und nicht verdampfenden Brennstoffstrahlen unter Hochdruck.* PhD thesis, Diss., Technische Wissenschaften ETH Zürich, Nr. 15004, 2003, 2003.

[13] Sallam, K A, Ng, C-L, Sankarakrishnan, R, Aalburg, C, and Lee, K. "Breakup of turbulent and non-turbulent liquid jets in gaseous crossflows." *AIAA Paper*, 1517:2006, 2006.

[14] Dewanji, D, Rao, G A, and van Buijtenen, J. Feasibility study of some novel concepts for high bypass ratio turbofan engines. In *ASME Turbo Expo 2009: Power for Land, Sea, and Air*, pages 51–61. American Society of Mechanical Engineers, 2009.

[15] Farokhi, S. *Aircraft propulsion.* John Wiley & Sons, 2014.

[16] Kyprianidis, K. *Future aero engine designs: an evolving vision.* 2011.

[17] Andriani, R, Gamma, F, and Ghezzi, U. "Thermodynamic analysis of a turboprop engine with intercooling and heat recovery." *Transactions of the Japan Society for Aeronautical and Space Sciences*, 54(183): 44–50, 2011.

[18] Seetharaman, S and Kahraman, A. "Load-independent spin power losses of a spur gear pair: model formulation." *Journal of Tribology*, 131(2):022201, 2009.

[19] Stavytskyy, V, Nosko, P, Fil, P, Karpov, A, and Velychko, N. "Load-independent power losses of gear systems: A review." *TEKA Kom. Mot. i Energ. Roln. B*, 10:205–213, 2010.

[20] Hill, M J and Kunz, R F. "A computational investigation of gear windage." 2012.

[21] Lord, A A. *Experimental investigation of geometric and oil flow effects on gear windage and meshing losses.* PhD thesis, University of Wales Swansea, 1998.

[22] Handschuh, R F and Kilmain, C J. Preliminary comparison of experimental and analytical efficiency results of high-speed helical gear trains. In *ASME 2003 International Design Engineering Technical Conferences and Computers and Information in Engineering Conference*, pages 949–955. American Society of Mechanical Engineers, 2003.

[23] Von Kármán, Th. "Technical memorandum on laminar and turbulent friction." *National Advisory Committee for Aeronautics Report*, (1092), 1921.

[24] Goldstein, S. On the resistance to the rotation of a disc immersed in a fluid. In *Mathematical Proceedings of the Cambridge Philosophical Society*, volume 31, pages 232–241. Cambridge Univ Press, 1935.

[25] Anderson, N E and Loewenthal, S H. Spur-gear-system efficiency at part and full load. Technical report, DTIC Document, 1980.

[26] Eastwick, C N and Johnson, G. "Gear windage: a review." *Journal of Mechanical Design*, 130(3):034001, 2008.

[27] Marchesse, Y, Changenet, C, Ville, F, and Velex, P. "Investigations on cfd simulations for predicting windage power losses in spur gears." *Journal of Mechanical Design*, 133(2):024501, 2011.

[28] Hill, M J, Kunz, R F, Medvitz, R B, Handschuh, R F, Long, L N, Noack, R W, and Morris, P J. "Cfd analysis of gear windage losses: validation and parametric aerodynamic studies." *Journal of Fluids Engineering*, 133(3):031103, 2011.

[29] Akin, LS. "An interdisciplinary lubrication theory for gears (with particular emphasis on the scuffing mode of failure)." *Journal of Engineering for Industry*, 95(4):1178–1195, 1973.

[30] Townsend, D P. "Lubrication and cooling for high speed gears." 1985.

[31] Akin, L S and Townsend, D P. "Lubricant jet flow phenomena in spur and helical gears with modified addendums; for radially directed individual jets." 1989.

[32] Saavedra, J J. *Effect of jet prandtl number on impingement cooling of rotating bodies.* PhD thesis, Citeseer, 1981.

[33] DeWinter, A and Blok, H. "Fling-off cooling of gear teeth." *Journal of Engineering for Industry*, 96(1):60–70, 1974.

[34] Johnson, G, Chandra, B, Foord, C, and Simmons, K. "Windage power losses from spiral bevel gears with varying oil flows and shroud configurations." *Journal of Turbomachinery*, 131(4):041019, 2009.

[35] Li, L, Versteeg, H K, Hargrave, G K, Potter, T, and Halse, C. "Numerical investigation on fluid flow of gear lubrication." 2009.

[36] Arisawa, H, Nishimura, M, Imai, H, and Goi, T. Cfd simulation for reduction of oil churning loss and windage loss on aeroengine transmission gears. In *ASME Turbo Expo 2009: Power for Land, Sea, and Air*, pages 63–72. American Society of Mechanical Engineers, 2009.

[37] Fondelli, T, Andreini, A, Da Soghe, R, Facchini, B, and Cipolla, L. Volume of fluid (vof) analysis of oil-jet lubrication for high-speed spur gears using an adaptive meshing approach. In *ASME Turbo Expo 2015: Turbine Technical Conference and Exposition*, pages V07AT31A006–V07AT31A006. American Society of Mechanical Engineers, 2015.

[38] "Numerical simulation of oil jet lubrication for high speed gears."

[39] Rosen, M W. "Noises of two spur-gear transmissions." *Noise Control*, 7(6):11–19, 1961.

[40] Wittbrodt, M J and Pechersky, MJ. A hydrodynamic analysis of fluid flow between meshing spur gear teeth. Technical report, DTIC Document, 1987.

[41] HOUJOH, H, OHSHIMA, S, MIYATA, S, TAKIMOTO, T, and MAENAMI, K. Dynamic behavior of atmosphere in a tooth space of a spur gear during mesh process from the viewpoint of efficient lubrication. In *Proceedings of DETC'00-8th International Power Transmission and Gearing Conference, Baltimore (2000.9)*, number PTG-14372, 2000.

[42] Houjoh, H, Ohshima, S, Matsumura, S, Yumia, Y, and Itoh, K. Pressure measurement of ambient air in the root space of helical gears for the purpose of understanding fluid flow to improve lubrication efficiency. In *ASME 2003 International Design Engineering Technical Conferences and Computers and Information in Engineering Conference*, pages 957–964. American Society of Mechanical Engineers, 2003.

[43] Diab, Y, Ville, F, Houjoh, H, Sainsot, P, and Velex, P. "Experimental and numerical investigations on the air-pumping phenomenon in high-speed spur and helical gears." *Proceedings of the Institution of Mechanical Engineers, Part C: Journal of Mechanical Engineering Science*, 219(8):785–800, 2005.

[44] Gorla, C, Concli, F, Stahl, K, Höhn, B-R, Michaelis, K, Schultheiß, H, and Stemplinger, J-P. "Hydraulic losses of a gearbox: Cfd analysis and experiments." *Tribology International*, 66:337–344, 2013.

[45] Burberi, E, Fondelli, T, Andreini, A, Facchini, B, and Cipolla, L. Cfd simulations of a meshing gear pair. In *ASME Turbo Expo 2016: Turbomachinery Technical Conference and Exposition*, pages V05AT15A024–V05AT15A024. American Society of Mechanical Engineers, 2016.

[46] Raffel, M, Willert, C E, Wereley, S T, and Kompenhans, J. Physical and technical background. In *Particle Image Velocimetry*, pages 15–77. Springer, 2007.

[47] ASME. "Measurement uncertainty in instrument and apparatus." *vol. ANSI/ASME PTC 19.1-1985 of Performance Test Code, ASME*, (19), 1985.

[48] Kline, S. J. and McClintock, F. A. "Describing uncertainties in single sample experiments." *Mechanical Engineering*, 75(1), 1953.

[49] Gancedo, M, Gutmark, E, and Guillou, E. "Piv measurements of the flow at the inlet of a turbocharger centrifugal compressor with recirculation casing treatment near the inducer." *Experiments in Fluids*, 57(2):1–19, 2016.

[50] Westerweel, J. "Fundamentals of digital particle image velocimetry." *Measurement science and technology*, 8(12):1379, 1997.

[51] *ANSYS® FLUENT, Theory Guide, Release 16.0.*

[52] Owen, JM and Roger, RH. "Flow and heat transfer in rotating-disc systems. volume i-rotor-stator systems." *NASA STI/Recon Technical Report A*, 90, 1989.

[53] Lumley, J L. "The structure of inhomogeneous turbulent flows." *Atmospheric turbulence and radio wave propagation*, pages 166–178, 1967.

[54] Sirovich, L. "Turbulence and the dynamics of coherent structures part i-iii: coherent structures." *Quarterly of applied mathematics*, 45 (3):561–590, 1987.

[55] Dynamics, Dantec. "Dantec dynamicstudio user's guide."

[56] Berrino, M, Lengani, D, Satta, F, Ubaldi, M, Zunino, P, Colantuoni, S, and Di Martino, P. Investigation of the dynamics of an ultra low nox injection system by pod data post-processing. In *ASME Turbo Expo 2015: Turbine Technical Conference and Exposition*, pages V04AT04A049–V04AT04A049. American Society of Mechanical Engineers, 2015.

[57] Reitz, R D. "Atomization and other breakup regimes of a liquid jet." 1978.